

**THERMOFLUIDIC IMPACTS OF GEOMETRICAL CONFINEMENT ON POOL
BOILING: ENABLING EXTREMELY COMPACT TWO-PHASE THERMAL
MANAGEMENT TECHNOLOGIES THROUGH MECHANISTIC-BASED
UNDERSTANDINGS AND PREDICTIONS**

by

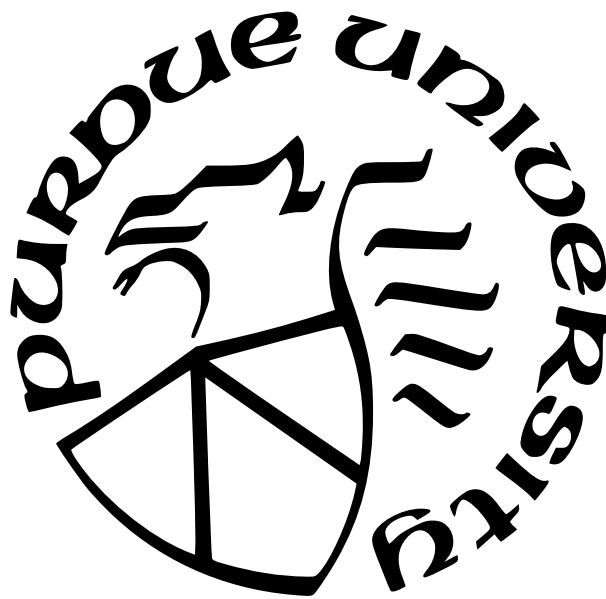
Albraa A. Alsaati

A Dissertation

Submitted to the Faculty of Purdue University

In Partial Fulfillment of the Requirements for the degree of

Doctor of Philosophy



School of Mechanical Engineering

West Lafayette, Indiana

May 2022

**THE PURDUE UNIVERSITY GRADUATE SCHOOL
STATEMENT OF COMMITTEE APPROVAL**

Dr. Amy M. Marconnet, Co-Chair

School of Mechanical Engineering

Dr. David M. Warsinger, Co-Chair

School of Mechanical Engineering

Dr. Justin A. Weibel

School of Mechanical Engineering

Dr. Alina A. Alexeenko

School of Aeronautics and Astronautics

Approved by:

Dr. Eckhard Groll

To those who push the frontiers of knowledge

ACKNOWLEDGMENTS

I would like to express my sincere gratitude to my advisor Dr. Amy Marconnet for her ever-present and invaluable support, guidance, and personal coaching throughout my graduate studies. Equally, I would like to thank Dr. David Warsinger for believing in me and encouraging me to reach my full potential. My gratitude extends to Dr. Justin Weibel for his continuous mentorship. His immense knowledge and plentiful experience in two-phase thermal management shaped the outcomes of this work. I am grateful for Dr. Timothy Fisher of University of California Los Angeles (UCLA) and Dr. Nicholas Glavin of the Air Force Research Laboratory (AFRL) for their contributions in building the experimental facility for this work. Dr. Alina Alexeenko I am grateful for your feedback and advice as part of the thesis examining committee.

To the industry liaisons, Dr. Rajiv Mongia and Dr. Feras Eid of Intel, Dr. Kamal Sikka of Apple and Dr. Anil Yuksel of IBM and Dr. Se-Ho You of Samsung, I am appreciative for providing your unique practical perspectives and feedback. I would like to also offer my special thanks to all my lab mates at Marconnet Thermal and Energy Conversion (MTEC) Lab, Warsinger Water Lab, and Cooling Technology Research Center (CTRC) for their support, encouragement, and friendship. Lastly, I am deeply grateful to my family and adored wife, Rawan, for the unconditional love and support.

Financial support for this work was provided by Semiconductor Research Corporation (SRC), as a part of the Global Research Collaboration (GRC) Program on Packaging (PKG; Science Director, Dr. John Oakley) in the Center for Heterogeneous Integration Research on Packaging (CHIRP) and the Saudi Arabia Cultural Mission (SACM) fellowship, sponsored by the Saudi Arabian Ministry of Education.

TABLE OF CONTENTS

LIST OF TABLES	8
LIST OF FIGURES	9
LIST OF SYMBOLS	16
ABBREVIATIONS	18
ABSTRACT	19
1 INTRODUCTION	20
1.1 Research Objective	22
1.2 Research Contributions	23
1.3 Organization	24
2 REVIEW OF BOILING PROCESSES FUNDAMENTALS	26
2.1 Boiling Heat Transfer	26
2.2 Boiling Models and Correlations	30
2.2.1 Nucleate Boiling Correlations	30
2.2.2 Nucleation Onset	33
2.3 Boiling Enhancement Techniques	37
2.4 Limitations of Nucleate Boiling	40
2.5 Geometrical Size Effect on Boiling	45
2.6 Summary and Relation to this Work	49
3 BOILING IN MICROSCALE GAPS	51
3.1 Introduction	52
3.2 Experimental Setup	53
3.3 Results and Discussion	56
3.3.1 Unconfined Pool Boiling Benchmark Testing	56
3.3.2 Confined Boiling Characterization	57

3.3.3	Confined Boiling Heat Transfer Enhancement	60
3.3.4	Impact of Confinement Gap and Window Size	61
3.4	Summary	63
4	STEM BUBBLES BOILING	65
4.1	Introduction	65
4.2	Experimental Methods	69
4.3	Results and Discussion	73
4.3.1	Confined Boiling Flow Visualization	73
4.3.2	Effect of Confinement Gap Spacing on Boiling Heat Transfer	75
4.3.3	Vapor Stem Bubbles	80
4.4	Summary	85
4.A	Nucleation Onset Model	88
5	CRITICAL HEAT FLUX (CHF) IN CONFINED GAPS	90
5.1	Introduction	91
5.2	State-of-the-Art Models for CHF in Confined Geometries	92
5.3	CHF Model Development	99
5.4	Results and Discussion	104
5.5	Summary	109
5.A	Confinement Threshold Limit	110
6	CONCLUSIONS AND FUTURE OUTLOOK	111
6.1	Conclusions	111
6.2	Future Outlook	112
6.2.1	Stem Bubble Boiling of Dielectric Coolants	113
6.2.2	Control the Formation of Stem Bubbles	113
6.2.3	Use Confinement Wall Wettability for Confined CHF Enhancement	115
	REFERENCES	117

A HETEROGENEOUS INTEGRATION OF ELECTRONICS AND ASSOCIATED
THERMAL CHALLENGES 134

LIST OF TABLES

2.1	Empirical correlations for boiling heat transfer proposed by Stephan and Abdelsalam [20].	34
2.2	A summary of modified dimensionless unconfined CHF ratios, $K = \frac{CHF}{\rho_v^{0.5} h_{lv} [\sigma g (\rho_l - \rho_v)]^{1/4}}$, based on Zuber's model [71] including the key physics upon which the models are based.	44
2.3	Modified dimensionless CHF ratios, $K = \frac{CHF}{\rho_v^{0.5} h_{lv} [\sigma g (\rho_l - \rho_v)]^{1/4}}$, based on Zuber's model [71] to account to finite geometrical effect.	47
2.4	Empirical correlations for confined boiling heat transfer.	48
2.5	Modified dimensionless CHF ratios, , $K = \frac{CHF}{\rho_v^{0.5} h_{lv} [\sigma g (\rho_l - \rho_v)]^{1/4}}$, based on Zuber's model [71] to account to geometrical confinement effect.	49
5.1	A summary of the dimensionless CHF ratios modified to account for additional factors, $K = \frac{q''_{CHF,Z}}{\rho_v^{0.5} h_{lv} [\sigma g (\rho_l - \rho_v)]^{1/4}}$	94
5.2	Collected database of experimental CHF in confined geometries.	105

LIST OF FIGURES

1.1	Examples of Boiling Applications: recent technological advances across different industrial sectors have led to increases in the required heat dissipation rates. Two-phase thermal management schemes use the latent heat of vaporization to facilitate the removal of high heat density in various applications such as transportation, defense, aerospace, energy, information technologies, and water applications. Images are adapted from "Recent Advances in High-flux, Two-phase Thermal Management" by Mudawar [3] with permission. Copyright 2013 ©by ASME.	21
1.2	Influence of confinement of the thermofluidic characteristics. The complexity of the boiling phenomena often necessitates statistical treatment of experimental measurements to develop relevant understanding and correlations. Many models developed for unconfined boiling focus on a one-dimensional analysis normal to the boiling surface. However, confinement wall forces the vapor bubble to grow parallel to the boiling surface. Therefore, the applicability of models developed for unconfined boiling needs to be carefully examined to account for the effect of confinement.	22
2.1	Representation of a typical pool boiling curve.	28
2.2	Illustration on the flow boiling regimes along a vertical tube. Similar to pool boiling, the heat transfer coefficient varies across different boiling regimes. Notably, the highest heat transfer coefficient is observed at the annular regime with no active nucleation sites on the boiling surface.	29
2.3	Schematic of the vapor entrapping mechanism in the groove as the liquid advances on the boiling surface.	35
2.4	Schematic of (a) bubble growth at a nucleation site on the boiling surface. The liquid temperature is highest right at the solid interface (red) and gradually reach the saturation temperature away from the solid interface (blue).(b) the criteria for the onset of nucleate boiling. In order for the bubble to grow, the temperature at the highest point of the bubble must be sufficient to overcome the surface tension. The dashed black line represents the temperature required for the bubble to grow for a given temperature. The red solid lines represents the liquid temperature away for the solid interface. Increasing the heat flux increases both the wall temperature and the temperature gradient. Nucleation onset occurs first the solid line intersect with the dashed line. More cavity size range are activated for heat fluxes higher that onset conditions.	36
2.5	The range of active cavity sizes using the model from Hsu [26] as a function of wall superheat for saturated water at atmospheric pressure and thermal boundary layer of 0.2 mm. Temperature above saturated temperature is required to onset nucleation. As the wall temperature increases, a larger range of vapor embryos sizes get activated.	37

2.6	Illustrations of vapor columns on a heated surface at CHF assuming the system is limited by the hydrodynamic instability of the far field liquid-vapor interfaces)	42
3.1	Schematic illustration of the confined boiling experimental facility. Cartridge heaters (not shown) provide heat to the copper rod from below. The heat flux and the boiling surface temperature are measured from thermocouples embedded in the copper rod. Thermal insulation surrounding the rod minimizes the radial temperature gradient and heat losses. An adjustable glass window confines boiling to within a controlled gap above the boiling surface. A camera captures the two-phase interfaces in the confinement gap as viewed through a rigid borescope. The pool of water is maintained at the saturation temperature using two auxiliary cartridge heaters with temperature control based on the thermocouples within the pool.	54
3.2	Experimental facility repeatability tests for the unconfined pool boiling curve. The highest heat flux value in each run represents the critical heat flux (CHF) compared to the theoretical prediction (green line). The inset images show the transition from (a) nucleate boiling to (b) film boiling following an increment to a heat flux higher than CHF.	57
3.3	Boiling curve for different nondimensional confinement gaps sizes ($Bo = S/L$) are shown as solid lines. Natural convection (gray shaded region) is observed at low heat fluxes where no nucleation sites are activated. During intermittent boiling (shaded in green), vapor is generated slowly enough that the entire boiling surface is able to rewet following periodic vapor departure from the gap. Finally, as the vapor generation frequency increases, the boiling transition to partial dryout regime (shaded in red) where regions of the boiling surface remain continually covered with vapor. The unconfined boiling curve is shown in blue as a dashed line for reference (regimes do not apply).	59
3.4	Surface temperature oscillations in the intermittent boiling regime ($Bo = 0.09$, $q''=1.5 \text{ W cm}^{-2}$). In the portions of the data where the surface temperature rises with time, the confined liquid is heated without phase change (inset (a)) until the minimum required superheat for nucleation is reached. Inset (b) illustrates the nucleation of vapor bubbles that escape from confinement region and are replaced by a sudden inrush of saturated liquid from surrounding pool that quenches the boiling surface.	60
3.5	Confined boiling heat transfer enhancement mechanisms. (a) Confinement induces radial growth of vapor bubbles enlarging the microlayer coverage compared to unconfined boiling. (b-e) A time series of images that illustrate nucleation-enhanced rewetting where the volume expansion during phase change at nucleation site (red dot) displaces liquid from wet areas to dry areas.	61
3.6	Influence of confinement gap size on the CHF for differing fractions of the area within the confined region heated by the boiling surface.	62

3.7	Influence of confinement gap size on the boiling surface superheat for differing heat fluxes. Cases are shown where (a) the boiling surface and confinement window are the same diameter and (b) where the boiling surface area is 1/2 of the confinement window area. A local minimum is observed near $Bo = 0.2$	63
4.1	Cross-sectional schematic of the confined boiling experimental apparatus. An electrical heater supplies heat into a copper rod of known thermal conductivity. Three temperature measurements along the rod with embedded thermocouples quantify the heat flux and are extrapolated to estimate the boiling surface temperature. A glass window confines boiling to within the gap of controlled the vertical distance between the boiling surface and the confinement wall, S . A high-speed camera captures the two-phase interface dynamics through a rigid borescope during boiling. Two auxiliary heaters maintain the liquid pool at the saturation temperature. A pressure transducer measures the chamber internal pressure. The exterior of the boiling chamber and the copper rod are well insulated to minimize heat losses.	70
4.2	Top view of the boiling surface at several points in time for a nucleation-suppressed confined circular boiling surface ($Bo = 0.30$ with $q'' = 10 \text{ W/cm}^2$). As the vapor expands (red arrows in t_2) and then escapes (red arrow in t_3) confinement, liquid replaces the vapor volume within the confined region (blue arrows in t_4 and t_5). Within the extremely confined boiling region, rewetting occurs at different rates at different positions along the two-phase interface. Viscous resistance slows the rewetting of regions furthers from the confinement edge as shown at time steps t_4 and t_5 . As a result, most of the vapor bubble escapes the confined region, but partially leaves behind a stem vapor bubble in the confined space at in time step t_6 . This new vapor bubble stems from the vapor left from the preceding vapor bubble and the cycle repeats.	74
4.3	Top view of the boiling surface at several points in time for a nucleation-active confined circular boiling surface ($Bo = 0.63$, $q'' = 14 \text{ W/cm}^2$). Consecutive isolated bubbles forms from an active nucleation site as shown inside the yellow circle at time step t_1 . Then, adjacent bubbles formed at different nucleation sites eventually coalesce into single bubbles having lower surface curvature as demonstrated inside the green circles at time steps t_2 and t_3 . The change in bubble curvature, and the associated internal pressure forces across the two-phase interface, allow for an abrupt increase in the growth rate of the coalesced vapor bubble (red arrows in time step t_4). The vapor bubble escapes confinement completely when it reaches the confinement edge (red arrows in time steps t_5 and t_6).	75

- 4.4 Boiling curves for different non-dimensional confinement gap size ($Bo = S/L_c$). The boiling process spans three distinct characteristics highlighted by different shaded regions. In the *partial dryout* (shaded in red), regions of the boiling surface remain continually covered with vapor due to restriction of liquid replenishing imposed by the confinement wall. As a result, boiling occurs at a higher surface superheat compared to a similar heat flux in the unconfined boiling curve. The blue shaded region is the *nucleation-active* confined boiling region. Nucleation-active confined boiling is limited by the minimum superheat for incipience as expressed in Equation 4.2 (green dashed line). Enhancements to the heat transfer coefficient are mainly attributed to the larger evaporative microlayer in confined boiling, where active nucleation sites are required to generate new vapor bubble, as demonstrated for nucleation-active confined boiling curves ($Bo = 0.9$ and 0.63). On the other hand, for nucleation-suppressed confined boiling ($Bo = 0.1, 0.2,$ and 0.3), vapor generates from the vapor stem bubbles left behind from a previous bubble growth and escape cycle in the *nucleation-suppressed* region (shaded in green). The relatively large radius of stem bubbles compared to vapor embryos allows vapor generation at superheat lower than the minimum superheat required for vapor embryos growth from the boiling surface. 77
- 4.5 Heat transfer coefficient for different non-dimensional gap sizes ($Bo = S/L_c$) as a function of heat flux. For the unconfined boiling case, the heat transfer coefficient increases with heat flux due to the increase in the active nucleation site density reaching a maximum unconfined heat transfer coefficient at CHF. However, in nucleation-suppressed confined boiling ($Bo = 0.1, 0.2$ and 0.3), the maximum heat transfer coefficient is achieved at the low range of heat flux values due to the stem bubble boiling enhancement mechanism. Similar enhancements are not observed in nucleation-active confined boiling ($Bo = 0.63$ and 0.9), where the main heat transfer coefficient enhancement mechanism is the extension in the area of the evaporative microlayer which is limited to the minimum incipience superheat criterion (dashed green line). 78
- 4.6 Schematic of (a) bubble growth at a nucleation site and (b) bubble growth within a confined boiling system. As the confined vapor bubble grows parallel to boiling surface (red arrow), the induced flow (blue arrow) agitates the protruded region of the vapor embryos and reduces its radius to the local surface roughness on the boiling surface. As a result, nucleation sites within the confined boiling space are hydrodynamically deactivated and the minimum superheat for nucleation onset is required to maintain boiling within the confined space. Note the color gradient in the left panel illustrates the temperature gradient from the surface temperature (red) to the saturation temperature (blue). 79

4.7	Flow visualizations and complementary schematics of the cycle of bubble growth and escape in nucleation-suppressed confined boiling. The time series demonstrates a life cycle of vapor bubble growing between the boiling surface and the confinement wall. In the first image t_1 , confinement limits the bubble to growing only parallel to the boiling surface. After the bubble reaches the edge of the confined zone, it can escape into the liquid pool. Liquid replaces the escaped vapor bubble at variable wetting rates across the two-phase interface, t_2 . The red arrows illustrate the vapor outflow of the confinement and the blue arrows illustrate the liquid inflow. Viscous resistance slows the rewetting for regions furthest from confinement edge which results in vapor splitting and partial vapor escape as illustrated in t_3 . Thus, stem vapor bubbles form from the residual trapped vapor within the confined space, t_4 . Because no active nucleation sites are required for stem bubble boiling, phase change occurs at reduced superheat compared to nucleate based boiling. This cycle then repeats.	81
4.8	(a) Confinement enhancement ratio in the heat transfer coefficient compared to unconfined boiling ($h_{con}(q'')/h_{\infty}(q'')$) as a function of heat flux illustrating the impact of the gap size on the transition between nucleation-active to nucleation-suppressed confined boiling. (b) Temporal evolution of the non-dimensional vapor bubble diameter (d/L_c) predicted from Equations 4.3-4.8 for the range of heat fluxes required for the onset of nucleate boiling observed experimentally ($T_i - T_{sat} \sim 4-5$ °C). The transition between inertia controlled and thermal controlled growth regimes occurs when the growth rate decays by 90% of initial value. Enhancements in heat transfer due to the vapor stem bubbles are significant when the confinement gap is smaller than the transition between the two bubble growth regimes.	86
5.1	Two-phase interface dynamics comparison during unconfined and confined pool boiling. (a) Illustration of the theoretical framework for the hydrodynamic instability theory for predicting CHF in saturated pool boiling on an infinite unconfined flat plate. The CHF is postulated to occur when the two-phase interfaces of the unconfined vapor columns are unstable based on the Helmholtz criterion. (b) Illustration of the effect of a confinement wall above a horizontal boiling surface on the two-phase interface dynamics. Instead of forming vapor columns normal to the surface, vapor bubbles are forced to grow parallel to the boiling surface. In both panels, arrows indicate the liquid (blue) and vapor (red) flow paths.	96

5.2	<p>Micro-hydrodynamics at the contact line as the governing mechanism for CHF in confined geometries (a) Side-view schematic of the cross-section of the confined boiling system where a bubble is growing within a gap spacing, S, from the boiling surface of a diameter, D. Forces governing the two-phase interface dynamics are illustrated with blue arrows. These include the hydrostatic forces, F_G, surface tension forces, F_S, and the vapor momentum forces, F_m. (b) Cross-sectional top view of the base of the confined vapor bubble just prior to CHF. Undulations in the perimeter of the bubble extend partially outside the confined boiling region allowing partial rewetting of the boiling surface near the confinement space perimeter (<i>i.e.</i>, the liquid inlet regions). The ratio of the vapor outlet regions (shown in red) to the full perimeter of the boiling surface (combined red and blue line), defined as ψ, is the single fitting parameter in our newly developed correlation.</p>	101
5.3	<p>Assessment of the proposed model for CHF in confined geometries. Both the experimental and predicted CHF are normalized by the prediction for the unconfined CHF from Zuber [71]. The solid black reference line indicates a perfect match, and the gray shaded region indicates $\pm 30\%$ from this reference line. This comparison is limited to a region where the proposed model is valid, namely, up to Zuber’s limit for unconfined conditions (a value of 1 on the normalized axes). Thereafter, a green line indicates Zuber’s limit and the shaded region illustrates $\pm 30\%$ around this limit.</p>	107
5.4	<p>Accuracy of the confined CHF models. The error is calculated by comparing the model to the experimental data points (N) in the dataset that are below the gap spacing threshold. The mean (μ) and standard deviation (STD) of the prediction error for each model are tabulated within the plot. The notch in the box marks the mean error, whereas the box edges mark the 25th and the 75th percentiles. The dashed whiskers illustrate the full range of the calculated error in the data set. The results of the proposed model that is based on the micro-hydrodynamics balance in this work is shown in black in the first row, demonstrating low mean error and a narrow spread of the error compared to the models shown in subsequent rows that are based on alternative frameworks. . .</p>	108
5.5	<p>Sensitivity of the Confinement Threshold. The error is calculated by comparing the model for the confined CHF model (Eqn. 5.14) to the experimental data points in the dataset that are below the proposed confinement threshold limit (Eqn. 5.15). The vertical black dashed line corresponds to the confinement threshold of one where the confined CHF matches the unconfined CHF. The confinement threshold depends on the dimensionless unconfined CHF ratio, K. The error is calculated for two values of K found in the literature (blue and orange lines). In both cases, the minimum error is found near a ratio of one indicating that the cutoff in the applicability of the model is when the predicted CHF with confinement match the unconfined prediction.</p>	110

6.1	Illustration of the confinement wall wettability effect on the heat transfer coefficient. Hydrophilic confinement wall promote complete rewetting of the boiling surface which reduces the enhancement associated with stem bubbles.	114
6.2	Illustration of the confinement wall wettability pattern concept for improving probability of stem bubble formation. Hydrophobic sites splits the vapor bubble as it escapes the confinement reducing the probability of complete rewetting. . .	115
6.3	Illustration of the confinement wall wettability pattern concept for manipulating the vapor area ratio at the confinement perimeter. The thin vapor layer on the super hydrophobic surface coalesce with the expanding trapped vapor bubble. As a results, mass transport of teh radially outflow of vapor is reduced on selected sections only.	116

LIST OF SYMBOLS

β	Surface Contact Angle (deg)
ψ	Vapor Area Ratio at the Confinement Opening Area, $\frac{A_v}{A_{\text{gap}}}$ (-)
ϵ	Perimeter of the Confined Heater (m)
Γ	Non-dimensional Radius of Bubbles, $\frac{R}{L_c}$ (-)
ν_{lv}	Specific Volume Difference (m^3/kg)
ρ_l	Liquid Density (kg/m^3)
ρ_v	Vapor Density (kg/m^3)
σ	Surface Tension (N/m)
θ	Boiling Surface Orientation ($^\circ$)
α_l	Liquid Thermal Diffusivity, $\frac{k_l}{\rho_l C_{pl}}$ (m^2/s)
A	Area (m^2)
Bo	Bond Number, $\frac{S}{L_c}$ (-)
C_b	Fitting Parameter Specific to Boiling System, (-)
C_{pl}	Liquid Heat Capacity, (J/K)
D	Boiling Surface Diameter (m)
D_d	Bubble Departure Diameter (m)
f	Friction Factor (-)
F_m	Momentum Force (N)
F_G	Hydrostatic Force (N)
F_s	Surface Tension Force (N)
g	Gravitational Acceleration (m/s^2)
h	Heat Transfer Coefficient (W/m^2K)
h_{lv}	Heat of Vaporization (J/kg)
H_i	Effective Depth of the Two-phase Interface (m)
Ja	Jackob Number, $\frac{\rho_l c_{pl}(T_{\text{inf}} - T_{\text{sat}})}{\rho_v h_{lv}}$ (-)
Nu	Nusselt Number, $\frac{hL_b}{k_l}$ (-)
n_a	Nucleation Site Density, (-)
f	Friction Factor, (-)

Re	Reynolds Number, $\frac{\rho_v U_b L_b}{\mu_l}$ (-)
K	Dimensionless Critical Heat Flux (-)
k_l	Liquid Thermal Conductivity (W/mK)
L_c	Capillary Length, $\sqrt{\frac{\sigma}{g(\rho_f - \rho_v)}}$ (-)
L_b	Boiling Characteristic Length, (m)
U_b	Boiling Characteristic Velocity, (m/s)
u_c	The Critical Helmholtz Velocity, (m/s)
Pr	Prandtl Number, $\frac{c_{pl}\mu}{k}$ (-)
q''	Heat Flux (W/m^2)
q''_{CHF}	Critical Heat Flux (W/m^2)
$q''_{CHF,Co}$	Confined Critical Heat Flux (W/m^2)
q''_i	Incipience Heat Flux (W/m^2)
R	Vapor Bubble Radius (m)
S	Confinement Gap Spacing (m)
t	Time (S)
t_d	Vapor Bubble Departure Time (S)
T_i	Incipience Surface Temperature (K)
T_{sat}	Saturation Temperature (K)
T_∞	Pool Temperature (K)
T_b	Boiling Surface Temperature (K)
ΔT_s	Wall Superheat, $T_b - T_{sat}$ (K)

ABBREVIATIONS

CHF Critical Heat Flux

HTC Heat Transfer Coefficient

IoT Internet of Things

TSV Through-silicon Via

I/Os Inputs and Outputs

IC Integrated Circuit

ABSTRACT

With new technologies taking advantages of the rapid miniaturization of devices to microscale across emerging industries, there is an unprecedented increase in the heat fluxes generated. The relatively low phase-change thermal resistance associated with boiling is beneficial for dissipating high heat flux densities in compact spaces. However, for boiling heat transfer, a high degree of geometrical confinement significantly alters two-phase interface dynamics which affects the flow pattern, wetting dynamics, and moreover, the heat transfer rate of the boiling processes. Hence, it is crucial to have a deeper understanding of the mechanistic effects of confinement on two-phase heat dissipation and carefully examine the applicability of boiling correlations developed for unconfined pool boiling to predict and optimize design of extremely compact two-phase thermal management solutions. This dissertation develops and demonstrate a fundamental understanding of the impact of confinement on pool boiling. To elucidate the mechanisms that impact confined boiling, this study experimentally evaluates boiling characteristics through the quantification of boiling curves and high-speed visualization across a range of gap spacing smaller than the capillary length of the working fluid.

This work reveals the existence of two distinct boiling regime uniquely observed in boiling in confined configurations (namely, intermittent boiling and partial dryout). In contrast to pool boiling where the maximum heat transfer coefficient occurs below the critical heat flux limit, the intermittent boiling regime demonstrates the highest heat transfer coefficient in confined boiling. Then, this study provides a mechanistic explanation for the enhanced heat transfer rate due to geometrical confinement. Mainly, small residual pockets of vapor, termed ‘stem bubbles’ herein, remain on the boiling surface through a pinch-off process. These stems bubbles act as seeds for vapor growth in the next phase of the boiling process without the need for active nucleation sites. Furthermore, this dissertation develops a more accurate, mechanistic-based model for the phenomena that occur at CHF in confined configurations. The newly developed mechanistic understanding and model provides guidance on new directions for designing extremely compact two-phase thermal solutions.

1. INTRODUCTION

Pool boiling is the process of phase change from liquid to vapor through the generation of bubbles on a heater surface which then depart by natural convection. For ‘pool’ boiling, as opposed to flow boiling, a stationary bath of liquid is generally above the heated surface, where generated vapor bubbles depart the heated surface by buoyancy. The large latent heat of vaporization facilitates the removal of high heat density while maintaining boiling surface at a relatively low temperature rise above the saturation temperature, often safely below critical temperature limits for a system. Typically, operating above the design temperature limits results in a material degradation or a malfunctioning of the systems. Therefore, boiling is used in a numerous of technological applications as shown in Figure 1.1. Currently, the power industry still takes an advantage of the high heat transfer rates associated with boiling for increasing the thermodynamic efficiency of extracting energy from solar, fossil, and nuclear fuels. Boiling is also essential in other technological applications such as refrigeration and air conditioning, food processing, and modern chemical and distillation processes.

Moreover, recent trends in modern devices miniaturization have spurred a new interest in confined boiling. Examples of those modern devices include computer electronics, data centers, hybrid vehicle power electronics, aircraft, space craft avionics, x-ray medical devices, and small modular nuclear reactor (SMR) [1], [2]. In addition, new manufacturing technologies have enabled the semiconductor industry to vertically integrate active and passive components within one package, *i.e.* ‘heterogeneous integration’. The emerging 3D heterogeneous integration technology reveal associated thermal challenges due to the higher thermal resistances within the stack and the higher total power density. Appendix A discusses the benefit of heterogeneous integration and the associated thermal challenges. The relatively low phase-change thermal resistance associated with boiling can be exploited for dissipating high heat flux densities in compact spaces.

These applications motivated researchers to understand the phenomenon of boiling starting with the foundational work of Nukiyama in 1934 [4]. Since the work of Nukiyama, considerable progress in the understanding of the boiling phenomenon has been made including boiling incipience, boiling hysteresis, heat transfer coefficient (HTC) associated with differ-

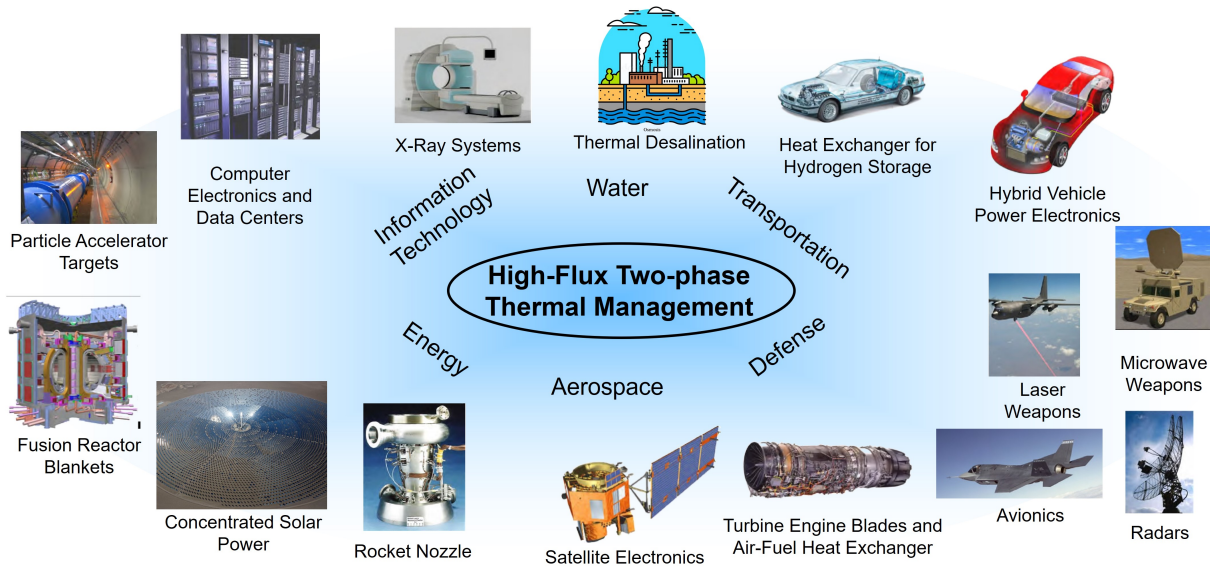


Figure 1.1. Examples of Boiling Applications: recent technological advances across different industrial sectors have led to increases in the required heat dissipation rates. Two-phase thermal management schemes use the latent heat of vaporization to facilitate the removal of high heat density in various applications such as transportation, defense, aerospace, energy, information technologies, and water applications. Images are adapted from "Recent Advances in High-flux, Two-phase Thermal Management" by Mudawar [3] with permission. Copyright 2013 ©by ASME.

ence boiling regimes, and the critical heat flux [5]. These research efforts continued, but by the 1980's, established models and theories were sufficient to describe most macroscopic boiling processes enabling safe operation of large heat transfer systems [6].

Boiling is a chaotic and a complex two-phase flow phenomenon. This complexity stems from the presence and the dynamic evolving of multiple interfaces covering a wide range of length scales extending from the macroscale down to the molecular level [6]. As a result, despite the decades of research and the growing importance of pool boiling, the fundamental physical mechanisms associated with boiling processes are still not fully understood [7].

Geometrical confinement further complicates the boiling process where it significantly alters the thermofluidic characteristics of pool boiling [8]. Primarily, vapor bubbles generated on the confined boiling surface are forced to grow parallel to the boiling surface extending the area of influence of nucleation sites, whereas many of the models developed and the

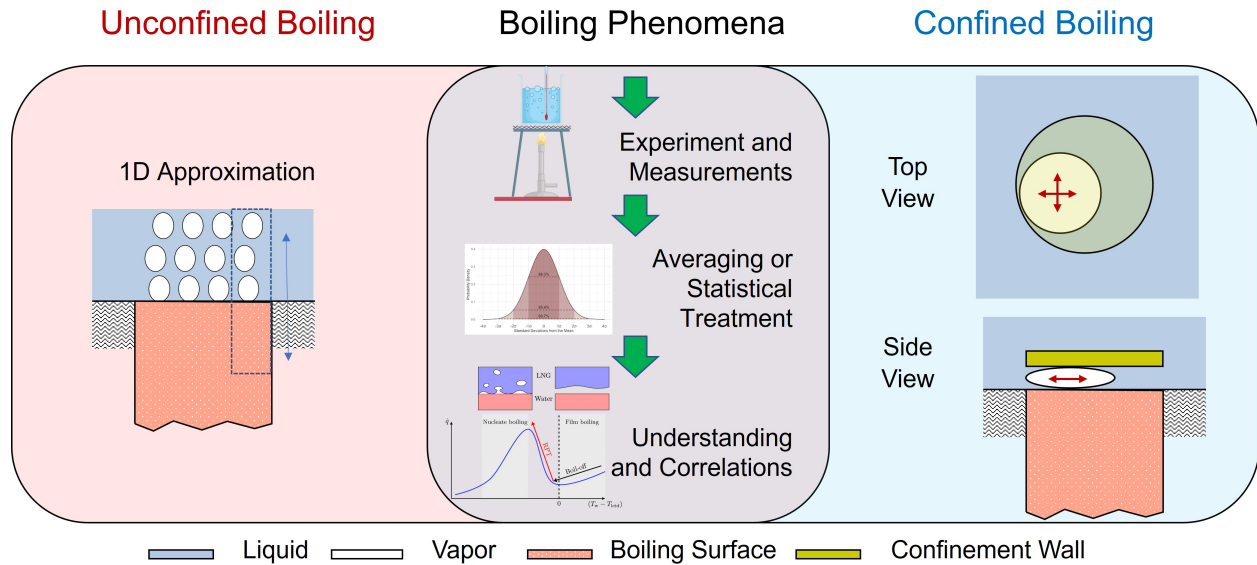


Figure 1.2. Influence of confinement of the thermofluidic characteristics. The complexity of the boiling phenomena often necessitates statistical treatment of experimental measurements to develop relevant understanding and correlations. Many models developed for unconfined boiling focus on a one-dimensional analysis normal to the boiling surface. However, confinement wall forces the vapor bubble to grow parallel to the boiling surface. Therefore, the applicability of models developed for unconfined boiling needs to be carefully examined to account for the effect of confinement.

understanding for pool boiling focus on a one-dimensional analysis normal to the boiling surface as illustrated in Figure 1.2. Therefore, the applicability of the existing pool boiling mechanistic understanding and corresponding models should be carefully examined and reevaluated prior applying them to confined boiling.

1.1 Research Objective

The objective of this work is to develop and demonstrate a fundamental understanding of the impacts of confinement on pool boiling in order to predict and optimize the design of two-phase thermal transport processes. To elucidate the mechanisms that impact confined boiling, this dissertation experimentally evaluates confined boiling across a range of gap spacings through quantification of the boiling curves and high-speed visualization of the bubble dynamics. Then, leveraging this deep mechanistic

understanding of the confinement effect to develop a predictive model of the thermal behavior of confined boiling which will enable a wider practical systems implementation of the technique.

1.2 Research Contributions

This dissertation generated new knowledge crucial to understanding the impact of confinement on boiling regimes, heat transfer coefficients, and critical heat fluxes, as summarized below and demonstrated throughout the remainder of this dissertation:

Confined Boiling Regimes: The thermofluidic characteristics of two-phase heat transfer are significantly affected by the spatial confinement. This work reveals the existence of two distinct boiling regimes uniquely observed in boiling in confined configurations (namely, intermittent boiling and partial dryout). Intermittent boiling exhibits a cyclic behavior where the heat dissipation method from the boiling surface alternate between single-phase and two-phase heat dissipation. In a nucleation-active confined boiling, rewetting liquid from unconfined pool lowers the surface superheat and boiling ceases momentarily until the surface heats up to the nucleation temperature. On the other hand, in the partial dryout confined boiling regime, portions of the surface remain continually dried out throughout the boiling process because the capillary forces are insufficient to overcome the viscous resistance necessary to completely rewet the boiling surface.

Heat Transfer Coefficient for Confined Boiling: Previous experimental studies reported that geometrical confinement results in enhancement of the heat transfer coefficient. However, previous work suggested that increased evaporation from the microlayer underneath the distorted vapor bubble was the primary mechanism of enhancement. This work unveils *nucleation-enhanced rewetting* as a complimentary enhancement mechanism for the nucleation-active boiling in confined configuration. As the vapor bubble grows, the confinement wall forces liquid to flow parallel to the boiling surface, facilitating the rewetting of the dry region of the boiling surface. On the other hand, for extremely confined configurations this work reports the observation of *nucleation-suppressed* boiling, where small residual pockets of vapor, termed ‘stem bubbles’ herein, remain on the boiling surface through a pinch-off

process. These stem bubbles act as seeds for vapor growth in the next phase of the boiling process and dominate the heat transfer enhancement in extremely confined boiling. Overall, these processes provide an improved mechanistic understanding of the improvements in heat transfer coefficients associated with confined boiling.

Critical Heat Flux for Confined Boiling: Geometrical confinement has detrimental effect of the Critical Heat Flux (CHF) (*i.e.*, the heat flux above which the boiling surface loses direct contact to the liquid because of the formation of a stable vapor layer resulting in drastic increase in overall thermal resistance). Moreover, the generalizability of much of the previously developed confined CHF models is limited since they were mostly based on the unconfined pool boiling triggering mechanism. This work develops a more complete, mechanistic based model for the phenomena that occur at CHF. The developed model postulates that the CHF coincides with the irreversible growth of dry spots on the boiling surface. Compared to existing models, the newly developed model improves the accuracy of predicting the impact of the confinement geometry on the CHF up to a limit where boiling dynamics are not affected by the confinement wall. This model increases confidence in the actual CHF limit and allows for reduction in engineering “safety factors”.

1.3 Organization

This dissertation is organized into the following chapters:

Chapter 1 introduces and motivates the research.

Chapter 2 reviews the fundamentals of boiling processes and the recent advances in confined boiling.

Chapter 3 describes the experimental investigation of the effect of confined boiling on the boiling regimes and the consequences on the heat transfer performance in terms of the heat transfer coefficient and the critical dryout limits of boiling.

Chapter 4 further explores the mechanisms of confined boiling and, based on high speed video and thermal results, proposes “stem boiling” as the dominant heat transfer enhancement mechanism for extremely confined boiling.

Chapter 5 develops a mechanistic model to predict saturated pool boiling Critical Heat Flux (CHF) in confined geometries.

Chapter 6 summarizes the major contributions of this dissertation and describes the future research directions.

2. REVIEW OF BOILING PROCESSES FUNDAMENTALS

This chapter reviews the fundamental of boiling processes and the recent advances in accounting for the geometrical influence on the thermofluidic characteristics of boiling. While there are some efforts to empirically account the geometrical implications in the boiling process, based on this review, there is a lack of established models that accounts for the implications on a fundamental level.

2.1 Boiling Heat Transfer

Similar to evaporation, boiling is the phase change process from liquid to vapor. However, there is key difference between evaporation and boiling. Evaporative phase change occur at the *liquid-vapor interface* when the vapor pressure of at the interface is less than the saturated pressure for a given temperature. Evaporation has proven to be an effective approach for many electronics cooling applications. For examples, heat pipes [9] and vapor chambers [10] are evaporative-based thermal designs and commercially used in electronics cooling applications. However, heat has to be transported from the solid surface to the evaporative interface through a liquid layer where wick materials are typically used to replenish the evaporated liquid. The physical separation between desired cooling surface, solid surface, and where the two-phase heat dissipation occurs leads to a trade off between solid surface temperature and the maximum heat flux limit beyond which the liquid layer dries out [10].

In contrast, boiling phase change occurs at the *solid-liquid interface* when the solid surface temperature is maintained above the saturation temperature of the working fluid. Boiling is characterized by rapid vapor bubble generation at the solid-liquid interface. The growing bubbles detach from the boiling surface and rise to the free surface when their buoyancy forces overcome bubble adhesion forces. The coincidence of the boiling surface and the two-phase heat dissipation mechanism has the potential to enable extremely miniaturized thermal solutions allowing for a more compact thermal management system.

Boiling is a non-equilibrium process where the vapor bubbles are not in thermodynamic equilibrium with surrounding liquid. In other words, the surrounding liquid temperature and pressure is typically different than the temperature and vapor pressure inside the vapor

bubble. Surface tension at the two-phase interface balances the pressure difference, while the temperature difference drives heat transfer across the two-phase interface. Heat is transferred from the bubble when the surrounding liquid is at lower temperature than the bubble causing vapor condensation and eventually bubble collapse. In contrast, heat is transfer to the bubble when the surrounding liquid is at higher temperature than the bubble causing bubble growth and the bubble to rise to the top due to increasing buoyancy forces. This distinction classifies boiling into two regimes: *subcooled boiling* and *saturated boiling*. Boiling is also classified into *pool boiling* and *flow boiling*. In pool boiling, the bulk of the fluid is stationary. The boiling surface relies on buoyancy driven flow for liquid rewetting. On the other hand, flow boiling relies on an active pump to circulate working fluid within the thermal system. Boiling typically occur at the inside wall of a sealed channel. Both boiling schemes require a separate condenser that eventually dissipates the heat into the ambient environment.

One the conventional thermal performance metrics used is the heat transfer coefficient (HTC or h). The heat transfer coefficient can be broadly defined as the coefficient of proportionality between the temperature difference, ΔT , and the applied heat flux, q . Commonly for boiling, the heat transfer coefficient is defined based on the temperature difference between the boiling surface temperature (T_b) and saturation temperature (T_{sat}): $\Delta T = T_b - T_{sat}$. This temperature difference is called the “excess temperature” or the “surface superheat”. Unlike conduction where the temperature difference is linearly proportional to the heat flux, the heat transfer coefficient during boiling depends on the surface superheat. Consequently, boiling curves that relate the boiling heat flux as a function of the surface superheat are used for characterizing the boiling thermal behavior. Figure 2.1 illustrates a representative heat flux control pool boiling curve including four sequential boiling regimes. At low heat fluxes, no bubbles are generated. Free (or natural) convection is sufficient to dissipate the heat from the boiling surface. Once the onset or nucleation is reached, bubbles start forming at certain sites, also known as nucleation sites, on the boiling surface. In the lower heat flux range of the nucleate boiling regimes, isolated bubbles are formed. As the bubble detach and depart the surface, liquid replenishes the vacated space rewetting the boiling surface where the bubble detached. As the heat flux increases within the nucleate boiling regime, bubbles form rapidly forming numerous continuous columns of vapor within the liquid. At

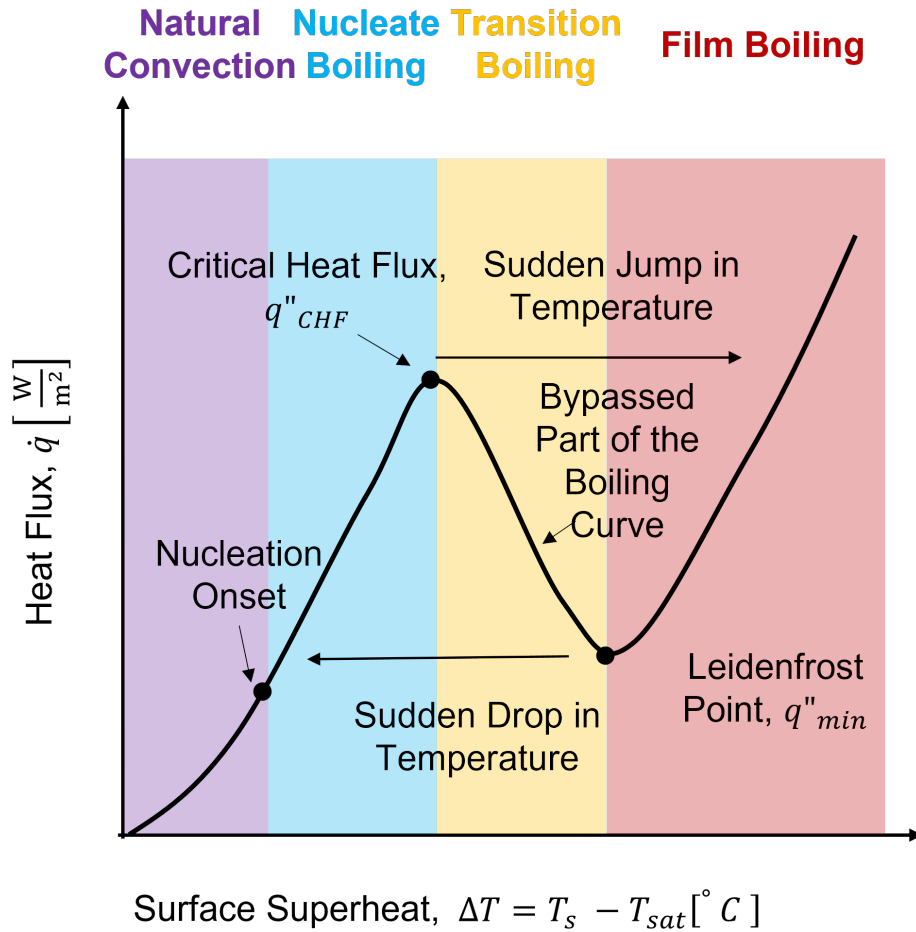


Figure 2.1. Representation of a typical pool boiling curve.

large surface superheats, vapor is generated at high rates making it difficult for the liquid to rewet the boiling surface. Consequently, unstable pockets of vapor partially cover the boiling surface. The heat flux at this point is termed the critical heat flux (CHF) where the boiling transitions from the nucleate boiling regime to film boiling. A continuous stable vapor layer is formed on the entire boiling surface at the film boiling regime. The vapor film acts as an insulating layer where heat is only transferred through conduction and radiation. Boiling processes exhibit a hysteresis effect. Once in the film boiling regime, heat flux needs to be reduced below the Leidenfrost point, which is much lower than CHF, to transition the boiling back to nucleate boiling regime.

The boiling regimes for flow boiling differ from pool boiling. Flow boiling regimes are classified based on the relative amount of liquid to vapor and vary along the length of the boiling channel. Figure 2.2 illustrates flow boiling regimes in a uniformly heated tube. Phase change is initiated in the subcooled flow boiling regime. A large radial temperature gradient characterizes this regime where bubbles are generated in the vicinity of the tube wall, while subcooled liquid flows near the center of the tube. Eventually, liquid at the core of the tube reaches saturation conditions and bubble can exist at any radial location at the bubbly flow boiling regime. Further downstream the bubble density increases and adjacent bubbles coalesce forming slugs in the slug flow regime. The annular flow regime follows with the liquid forming a thin layer near the wall. It is worth noting that the highest heat transfer

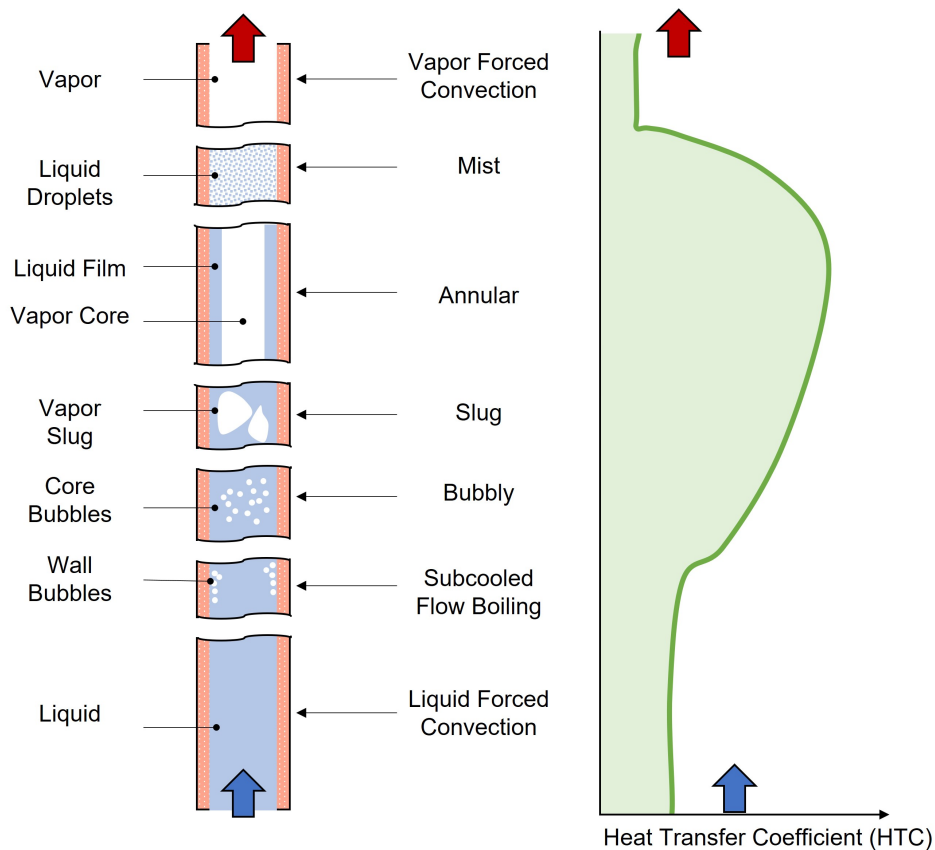


Figure 2.2. Illustration on the flow boiling regimes along a vertical tube. Similar to pool boiling, the heat transfer coefficient varies across different boiling regimes. Notably, the highest heat transfer coefficient is observed at the annular regime with no active nucleation sites on the boiling surface.

coefficient in flow boiling is observed in annular regime with no active nucleation sites on the heated surface. Rather, relatively large vapor core spans almost the entire cross-sectional area of the channel. Eventually, the liquid layer around the vapor core get depleted leaving the inner wall of the tube dry in the mist regime where the remaining liquid exist in a form of droplets within the vapor core. After the droplets completely evaporate, heat is dissipated through the forced convection of the moving vapor.

2.2 Boiling Models and Correlations

The characteristics of each boiling regime differ considerably. Hence, developing a unified model that represents thermal behavior during boiling across multiple regimes has been a challenge that yet to be solved. Among the boiling regimes, nucleate boiling is particularly well studied due to its relevance in a wide variety of applications. A complete review of all the effort in modeling all boiling regimes is beyond the scope of this thesis. Instead, the following sections review a few approaches for modeling heat transport in the nucleate boiling regimes and the operational limits of nucleate boiling.

2.2.1 Nucleate Boiling Correlations

The micro-agitation of fluid in the vicinity of nucleated bubbles is among the common approaches to model the high heat transfer rate associated with nucleate boiling. Rohsenow [11] used the micro-convection approach to develop a correlation adapted from single-phase forced-convection correlation with a modified length and velocity scales. This approach implies that boiling heat transfer correlation for the Nusselt number, Nu_b follows the form:

$$Nu_b = \frac{hL_b}{k_l} = ARe_b^n Pr_l^m, \quad (2.1)$$

where $h = \frac{q''}{T_b - T_{sat}}$ is the convection coefficient, $Re_b = \frac{\rho_v U_b L_b}{\mu_l}$ is the Reynolds number, Pr is the Prandtl number, ρ_v is the vapor density. μ_l is the liquid viscosity, and k_l is the liquid thermal conductivity. Here, L_b is a suitable length scale and the Reynolds number is scaled by the suitable velocity and the heat transfer coefficient is defined in relation to the surface

superheat. Rohsenow [11] used the bubble departure diameter, d_d , and the vapor superficial velocity, $U_b = \frac{q''}{\rho_v h_{lv}}$, as the scaling parameters to develop the following boiling heat transfer correlation:

$$\frac{q''}{\mu_l h_{lv}} \left[\frac{2\sigma}{g(\rho_l - \rho_v)} \right]^{1/2} = \left(\frac{1}{C_{sf}} \right)^{1/r} Pr_l^{-s/r} \left[\frac{C_{pl}[T_b - T_{sat}(P_l)]}{h_{lv}} \right]^{1/r}, \quad (2.2)$$

where $C_{sf} = \frac{\sqrt{2}C_b\omega}{A}$, $d_d = L_b = C_b\omega \left[\frac{2\sigma}{g(\rho_l - \rho_v)} \right]^{1/2}$, σ is the surface tension, ω is the contact angle, ρ_l is the liquid density, g is the gravitational acceleration, h_{lv} is the latent heat of vaporization, c_{pl} is the liquid heat capacity, and C_b , A , r , and s are fitting parameters specific to the boiling system. Over the years, recommended fitting parameters have been listed for common boiling systems [12].

Forster and Zuber [13] also developed a boiling correlation based on the micro-convection approach. Their model used a bubble growth relation (developed in their earlier investigations [14]) such that the bubble radius, R , is given by the following relation for thermally-controlled growth:

$$R = Ja(\pi\alpha_l t)^{1/2}, \quad (2.3)$$

where

$$Ja = \frac{[T_\infty - T_{sat}(P_\infty)]C_{pl}\rho_l}{\rho_v h_{lv}}. \quad (2.4)$$

The growth rate for the bubble radius is

$$\dot{R} = Ja \left(\frac{\pi\alpha_l}{4t} \right)^{1/2}. \quad (2.5)$$

Using the bubble diameter ($2R$) and growth rate (\dot{R}) as the length and velocity scales, respectively, the boiling correlation becomes

$$Nu_b = \frac{q''(2R)}{(T_b - T_\infty)k_l}, \quad (2.6)$$

where

$$Re_b = \frac{2R\rho_l\dot{R}}{\mu_l} = \pi Ja^2 Pr_l^{-1}. \quad (2.7)$$

Note that Foster and Zuber's correlation differs from Rohsenow's correlation in number of aspects. The heat transfer is defined in relation to the liquid bulk temperature instead of the saturation temperature, the Reynolds number is independent of the bubble radius, and the scale length is time dependent.

Other investigators [15] validated that the convection to liquid is the main contributor to heat dissipation of boiling surface. This validation justifies the use of micro-convection approach for boiling correlations. However, micro-convection is a steady state approach and boiling is a very dynamical physical phenomenon. Forster and Greif [14] proposed a transient based model postulating that nucleated bubbles act as micro-pump that draws cold bulk liquid into the boiling surface as the bubble departs the surface. Therefore, they proposed the following model based on the bubble maximum radius, R_{max} , bubble frequency, f , and the nucleation site density, n_a :

$$q'' = \rho_l c_{pl} \left(\frac{2\pi}{3} \right) R_{max}^3 \left(\frac{1}{2} \right) (T_b - T_\infty) f n_a. \quad (2.8)$$

Later, Mikic and Rohsenow [16] combined both the steady micro-convection approach with the transient vapor-liquid exchange approach by superimposing convection dissipation in between active nucleation sites. Their proposed correlation can be written in this form:

$$\frac{\bar{q}''}{\mu_l h_{lv}} \left[\frac{2\sigma}{g(\rho_l - \rho_v)} \right]^{1/2} = B[\Phi(T_b - T_{sat})]^{m+1}, \quad (2.9)$$

where

$$\Phi = \left[\frac{k_l^{1/2} \rho_l^{17/8} c_{pl}^{19/8} h_{lv}^{m-23/8} \rho_v^{m-15/8}}{\mu_l (\rho_l - \rho_v)^{9/8} \sigma^{m-11/8} T_{sat}^{m-15/8}} \right]^{1/(m+1)}, \quad (2.10)$$

and B and m are system-dependent fitting parameters. Similarly, Zuber [17] also proposed to combine the micro-convection approached and the transient vapor-liquid exchange approach. However, Zuber's model uses the correlation developed for turbulent natural convection while substituting the appropriate velocity, length, and time scales. The resulting correlation has the form:

$$\frac{q'' L}{k_l} = C_0 \left(\frac{gL^3}{\nu_l \alpha_l} \left[\beta(T_b - T_{sat}) + \frac{\pi}{6} n_a d_d^2 \frac{d_d f (\rho_l - \rho_v)}{\rho_l u_T} \right] \right)^{1/3}. \quad (2.11)$$

While micro-convection dominates the heat dissipation at the low heat flux range in the isolated bubble regime, experimental data indicates that it does not accurately capture the total heat dissipation at the higher range of heat flux where the spacing between active nucleation sites is reduced. A large fraction of the heat is dissipated through the evaporation of the microlayer underneath the bubble. Van Stralen [18] validated experimentally that a superposition of micro-convection and the latent heat of vaporization is an appropriate approach to model boiling across a large of range of heat fluxes. Judd and Hwang [19] also proposed a model that accounts for microlayer evaporation in addition to the micro-convection and nucleate boiling mechanisms to predict the heat flux yielding the relationship

$$q'' = 4.35 \times 10^8 n_a f V_{me} + 184(T_w - T_\infty)^{4/3} [1 - K\pi R_b^2 n_a] + 1543K R_b^2 \sqrt{f} n_a (T_b - T_\infty), \quad (2.12)$$

where V_{me} is the volume of the microlayer evaporated, R_b is the radius of influence by bubble, and K is the ratio between influence area around nucleation sites and the projected bubble area at departure.

Most of the models described above idealized shapes and location of isolated bubbles and, then, build a heat and mass transport model based on those idealizations. As a result, boiling correlations requires prior knowledge about bubble frequencies, nucleation density, bubble shape, and bubble size. Despite the intensive investigation efforts over many years, these parameters are not well understood in boiling processes. As a result, best boiling correlations still have 30-40 % deviation form experimental data. The uncertainties in analytical based approaches paved the way for an empirical based approached that are validated in the tested ranged only. Stephan and Abdelsalam [20] proposed the empirical boiling heat transfer correlations for various working fluids summarized in Table 2.1.

2.2.2 Nucleation Onset

Bubble nucleation is classified into homogeneous nucleation (that is, bubble nucleation completely in superheated liquid) and heterogeneous nucleation (*i.e.*, nucleation at the interface of fluid and solid). In the case of heterogeneous nucleation, when heat added to the

Table 2.1. Empirical correlations for boiling heat transfer proposed by Stephan and Abdelsalam [20].

For water in the pressure range $10^{-4} < P/P_C < 0.886$ with $\theta = 45^\circ$:

$$\frac{q'' D_b}{k_l(T_w - T_{sat})} = 2.46 \times 10^6 \left(\frac{q'' D_b}{k_l T_{sat}} \right)^{0.673} \left(\frac{h_{fg} D_b^2}{\alpha_l^2} \right)^{-1.58} \left(\frac{c_p T_{sat} D_b^2}{\alpha_l^2} \right)^{1.26} \left(\frac{\rho_l - \rho_v}{\rho_l} \right)^{5.22}$$

For hydrocarbons in the pressure range $5.7 \times 10^{-3} < P/P_C \leq 0.9$ with $\theta = 35^\circ$:

$$\frac{q'' D_b}{k_l(T_w - T_{sat})} = 0.0546 \left(\left(\frac{q'' D_b}{k_l T_{sat}} \right) \left(\frac{\rho_v}{\rho_l} \right)^{0.5} \right)^{0.67} \left(\frac{h_{fg} D_b^2}{\alpha_l^2} \right)^{0.248} \left(\frac{\rho_l - \rho_v}{\rho_l} \right)^{4.33}$$

For cryogenic liquids in the pressure range $4.0 \times 10^{-3} < P/P_C \leq 0.97$ with $\theta = 1^\circ$:

$$\frac{q'' D_b}{k_l(T_w - T_{sat})} = 4.82 \left(\frac{q'' D_b}{k_l T_{sat}} \right)^{0.624} \left(\frac{(\rho_c k)_c}{(\rho_c k)_l} \right)^{0.1117} \left(\frac{\rho_v}{\rho_l} \right)^{0.257} \left(\frac{c_p T_{sat} D_b^2}{\alpha_l^2} \right)^{0.374} \left(\frac{h_{fg} D_b^2}{\alpha_l^2} \right)^{-0.329}$$

For refrigerants in the pressure range $3.0 \times 10^{-4} < P/P_C < 0.78$ with $\theta = 35^\circ$:

$$\frac{q'' D_b}{k_l(T_w - T_{sat})} = 207 \left(\frac{q'' D_b}{k_l T_{sat}} \right)^{0.745} \left(\frac{\rho_v}{\rho_l} \right)^{0.581} \left(\frac{\nu_l}{\alpha_l} \right)^{0.533}$$

system through the solid heated surface, the liquid immediately adjacent to the solid interface exhibit the highest temperature and may exceed the equilibrium saturation condition. Hence, bubble nucleation is most likely to occur at the solid interface. Theoretical analysis concluded that surface superheat approaches the homogeneous nucleation is required to initiate boiling at perfectly wetted liquid-solid interface [21]. For instance, based on the liquid phase stability analysis, water at atmospheric pressure is predicted to require wall temperature around 300 °C to initiate boiling for a perfectly wetted liquid-solid interface with not the presence of trapped gasses on the surface [22]. However, this degree of superheat is rarely observed experimentally. Instead, water start boils in a metal pan at wall superheat no more than 15 °C. The low surface superheat required for boiling is attributed to the presence of trapped gas within solid surface crevices. Most real solid surfaces contain defects and irregularities leading to incomplete liquid wetting. The energy requirements to expand pre-existing vapor-liquid interfaces are much lower than for initiating the vapor phase in the fluid. Trapped gasses facilitating boiling at reduces surface superheat has been experimental validated [23]–[25]. Figure 2.3 illustrates vapor entrapment as a liquid wets the surfaces leading to formation a nucleation site.

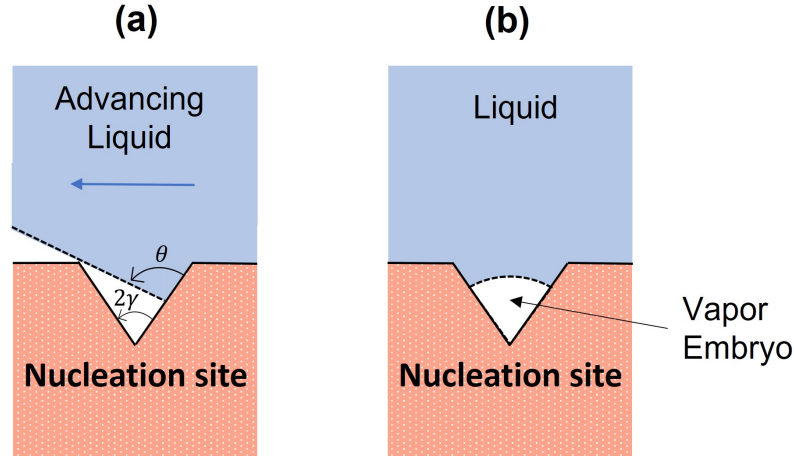


Figure 2.3. Schematic of the vapor entrapping mechanism in the groove as the liquid advances on the boiling surface.

The advancing contact angle, θ_a , of the triple line (vapor-liquid-solid) plays a crucial role in trapping vapor in a surface groove angle of 2γ . As the liquid front moves, the liquid-vapor interface will contact the opposite wall of the groove without completely wetting the groove if $\theta_a > 2\gamma$ as shown in Figure 2.3(a). Similarly, receding liquid line will leave liquid in the groove if the receding contact angle is $\theta_r < 180 - 2\gamma$. Contact angle hysteresis, $\theta_a - \theta_r$, improve the probability of trapping gap in surface cavities. However, the effectiveness of trapped gasses in initiating boiling depends on the rate of gas-liquid diffusion rate. For example, pure degassed liquids dissolve trapped gasses faster than aerated liquid which deactivates cavities. On the other hand, once nucleation sites become active and generate vapor, over time all non-condensable gasses get removed leaving only vapor behind. If the surrounding liquid cools down, the vapor may completely condense deactivating the nucleation site and leading to boiling hysteresis.

The entrapped vapor plays a crucial role in determining the active nucleation site density on the boiling surface and the onset conditions for nucleation. For an entrapped vapor embryo to grow, its internal vapor pressure must overcome the external liquid pressure in addition to the surface tension pressure. Once the nucleation site is activated bubbles are generated in cyclic steady growth pattern usually termed the *ebullition cycle* as illustrated in Figure 2.4. The liquid surrounding the growing bubble is subjected to conductive temperature drop

away from the boiling surface. Hsu [26] proposed a semi-theoretical model accounting for the non-uniform of the surrounding liquid in determining the range of surface cavities that will be active for given boiling conditions. The model Hsu developed considers a trade off in active nucleation site size between bubble radius of curvature and the temperature drop away for the boiling surface.

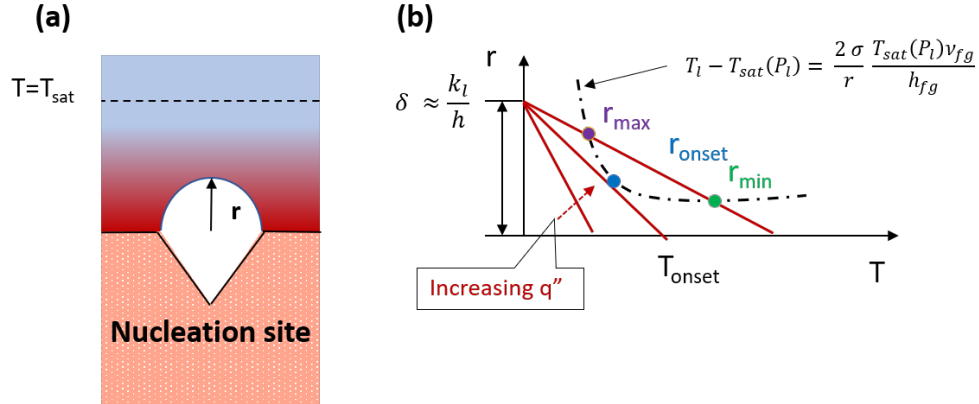


Figure 2.4. Schematic of (a) bubble growth at a nucleation site on the boiling surface. The liquid temperature is highest right at the solid interface (red) and gradually reach the saturation temperature away from the solid interface (blue). (b) the criteria for the onset of nucleate boiling. In order for the bubble to grow, the temperature at the highest point of the bubble must be sufficient to overcome the surface tension. The dashed black line represents the temperature required for the bubble to grow for a given temperature. The red solid lines represents the liquid temperature away for the solid interface. Increasing the heat flux increases both the wall temperature and the temperature gradient. Nucleation onset occurs first the solid line intersect with the dashed line. More cavity size range are activated for heat fluxes higher that onset conditions.

The Young-Laplace equation combined with Clausius-Clapeyron relation results in the following relation between boiling conditions and radius of bubble embryos, r_e :

$$T_l - T_{sat}(P_l) = \frac{2\sigma T_{sat}(P_l)}{\rho_v h_{fg} r_e}. \quad (2.13)$$

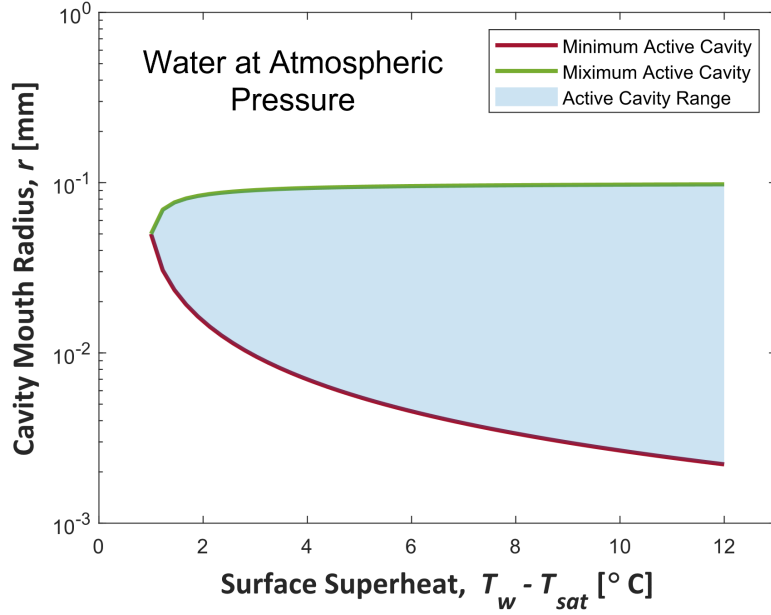


Figure 2.5. The range of active cavity sizes using the model from Hsu [26] as a function of wall superheat for saturated water at atmospheric pressure and thermal boundary layer of 0.2 mm. Temperature above saturated temperature is required to onset nucleation. As the wall temperature increases, a larger range of vapor embryos sizes get activated.

Hsu [26] proposed that the radius of the bubble embryos, r_e , related to the mouth radius of the cavity on which the bubble forms, r_c , as $2r_c = 1.6r_e$. Mathematically, the range of active cavity sizes, r_{min} and r_{max} is expressed as

$$\left\{ \begin{array}{l} r_{c,min} \\ r_{c,max} \end{array} \right\} = \frac{\delta_t}{4} \left[1 - \frac{(T_{sat} - T_\infty)}{(T_b - T_\infty)} \left\{ \begin{array}{l} + \\ - \end{array} \right\} \sqrt{\left(1 - \frac{(T_{sat} - T_\infty)}{(T_w - T_\infty)} \right)^2 - \frac{12.8\sigma T_{sat}(Pl)}{\rho_v h_{lv} \delta_t (T_b - T_\infty)}} \right], \quad (2.14)$$

where δ_t is the thickness of the thermal boundary layer. Figure 2.5 shows the predicted range of active cavities using the model for incipience of Hsu [26].

2.3 Boiling Enhancement Techniques

Several techniques to enhance the boiling heat transfer coefficient and the critical heat flux of boiling have been proposed. Based on the mechanisms of nucleate boiling and the

critical heat flux (CHF), the boiling heat transfer coefficient and CHF can be enhanced through the following strategies:

- Increasing the abundance of the surfaces cavities that can act as nucleation sites through trapped gas or vapor.
- Controlling the nucleation cavity size range to facilitate onset of nucleate boiling at low superheat while activating more cavities at high heat flux.
- Drawing more liquid toward the contact line region under the bubble through increasing surface wettability.
- Extending the solid-liquid interface area to enhance the overall heat transfer rate.

Modification of surface roughness as a technique for boiling enhancement has been explored since the early 1930's [27]. Increasing surface roughness increases the number of active nucleation site which improves the nucleate boiling performance [28]–[30]. Both incipience and nucleate boiling heat transfer is affected by roughness [28], [29], [31]. In fact, advanced micro-machining technologies have enabled optimizing surface roughness morphology to further improve boiling performance. For instance, the CHF of water on etched surfaces has been reported to be up to 51% larger than sanded surfaces to the same roughness [32].

In addition, introducing a microstructured porous wick layer on the boiling surface adds extra liquid flow paths through capillary driven flow in the interstitial spaces to the liquid-vapor interface. Various models have been developed to predict the enhancement of CHF due to the microstructured surfaces [33]–[35]. In general, the thickness of the microstructured wick layer leads to a trade-off between increasing the boiling heat transfer coefficient and increasing the CHF. While thick wick layers improve liquid flow to the liquid-vapor interface, they also add a thermal contact resistance in the heat flow path.

Advanced manufacturing techniques have also enabled engineering boiling surfaces with tunnels and reentrant cavities. As discussed in sections above, bubbles grow when the internal pressure, which is directly correlated to vapor temperature, overcomes the effect of surface tension and surrounding liquid pressure. Nakayama *et al.* [36] demonstrated that convex vapor interface reduces the superheat required for the bubble to grow compared to

concave vapor interfaces. The convex vapor interfaces were achieved by fabricating micro-tunnels on the boiling surface then cover them with thin plate having rows of micro pores. Under ‘suction-evaporation mode’, tunnels were filled by vapor and nucleate boiling occurred at the cover plate pores. The bubble release from active sites caused liquid suction on inactive sites resulting in convex vapor interface.

Microporous coatings on the boiling surface have been demonstrated to enhance pool boiling performance. The enhancement relies on a combination of capillary-assisted liquid supply, increased surface area, dense nucleation sites, and preferential vapor release route. For FC-72 heat transfer fluid, surfaces coated with copper microparticles have been demonstrated to reduce the required superheat for incipience by 80% while increasing the boiling heat transfer coefficient by 330% in nucleate boiling and increasing the CHF by 100% [37]. Similarly, micro-fin patterns on the boiling surface induce capillary liquid flow in addition to increasing the boiling surface area. Micro-fins were able to increase heat transfer coefficient on boiling water by 300% and CHF by 300% compared to bare surfaces [38]. In general, the boiling enhancements due to micro-structures have similar trends to that observed to roughened surface. Boiling requires less superheat shifting the boiling curve to the left. Additionally, wickability associated with micro-structures increase CHF.

Nanostructured boiling surfaces also have demonstrated improve boiling performance [39]–[44]. Numerous studies demonstrated the improvement in water boiling CHF due to the nanostructured boiling surfaces [45]–[52]. The nanostructures significantly decrease the surface contact angle, however, the change in surface wettability solely does not accurately explain the thermal enhancement. CHF models developed for highly wetting surfaces generally do not predict nanostructured boiling surfaces CHF. Thus, Rahman *et al.* [53] proposed the use of wicking number, Wi :

$$Wi = \frac{\dot{V}'_0 \rho_l}{\rho_v^{1/2} [\sigma(\rho_l - \rho_v)g]^{1/4}}, \quad (2.15)$$

where V_0' is the initial wicked volume flow rate. The wicking number correlate the critical heat flux of a wicking number to the critical heat flux of non-wicking surface, $q_{CHF,nw}''$, for the same condition as follows:

$$\frac{q_{CHF}''}{\rho_v^{1/2} h_{lv} [\sigma(\rho_l - \rho_v)g]^{1/4}} = \frac{q_{CHF,nw}''}{\rho_v^{1/2} h_{lv} [\sigma(\rho_l - \rho_v)g]^{1/4}} [1 + Wi]. \quad (2.16)$$

While micro-/nano-structured surface demonstrated enhancement in boiling processes, implementing them in applications requires additional considerations. The enhancements tend to degrade due to fouling, thermal stresses, and absorbed material [54], [55]. Modification of surface wettability is another common approach to enhance boiling performance. However, modification of surface wettability poses a trade-off between increased heat transfer coefficient and increased CHF. While hydrophobic surfaces lower the boiling superheat required for incipience and increase the heat transfer coefficient, they also lower the CHF [56]–[60]. Investigations into the effect of contact angle on nucleate boiling found that hydrophobic surfaces hinders that detachment of the bubbles of the boiling surface facilitating bubble growth and coalescence and eventually forming a vapor film on the surface. On the other hand, hydrophilic surfaces increase the bubble departure diameter while reducing the bubble generation frequency [61], [62]. The trade-off in the impact of surface wettability motivated investigations into the boiling performance of heterogeneous surfaces composed of hydrophilic surfaces with hydrophobic patterns. Experiments have demonstrated that heterogeneous surfaces improve both the nucleation boiling heat transfer coefficient and the CHF [52], [63].

2.4 Limitations of Nucleate Boiling

In a typical boiling curve (Figure 2.1), nucleate boiling transitions into film boiling when the applied heat flux reaches the critical heat flux (CHF). Before reaching the CHF, energy has to transport through the following energy transfer mechanisms:

M1: Energy transfer across the solid-liquid interface.

M2: Energy transfer from the liquid-solid interface to the liquid-vapor interface.

M3: Energy transfer across the liquid-vapor interface.

M4: Far field vapor transport away from the boiling surface preventing dryout.

M5: Far field liquid transport toward the boiling surface replenishing vaporized liquid.

M6: Near surface liquid transport and wetting of the surface in the contact line region.

Interruption in any of those mechanisms limits the boiling process. The boiling system configuration determines which of those transfer mechanisms is the factor that limits the maximum heat transfer rate for nucleate boiling. Models to predict CHF generally postulate that one of the transfer mechanisms is the weak link in the boiling process chain. Analysis indicates that the thermal energy carriers, phonons, scattering across the solid-liquid interface is unlikely to be the limiting transport mechanism [64], [65]. Similarly, the maximum vapor flux across the liquid-vapor interface using kinetic theory typically yields large maximum transfer rate limits compared to the other transfer mechanisms [65]. Thus, investigators historically focused on either the far field counter flow of vapor and liquid or near field liquid delivery to the contact line as the limiting factor in the nucleation boiling process.

Rohsenow and Griffith [66] and Chang and Snyder [67] postulated that the near field liquid supply to the contact line limits nucleate boiling. As the applied heat flux increases, more nucleation sites are activated. Eventually, a critical nucleation site density is reached where liquid flow to the contact surface is blocked. However, models based on this approach require accurate quantification of the bubble generation frequency and bubble departure diameter. Despite previous efforts, those quantities are still not well understood and challenging to be accurately quantified. In addition, visual evidence does not support the premise that round bubbles are packed against the surface tightly near the CHF.

Another widely accepted analytical approach to predict CHF is through the analysis of the hydrodynamic instabilities of far field counter flow liquid-vapor interfaces. Kutateladze [68] employed a dimensional analysis approach to postulated the functional dependence of the CHF on various parameters. This leads to the dimensionless Kutateladze number, Ku , which is defined as:

$$Ku = \frac{q_{CHF}}{\rho_v h_{lv}} \left[\frac{\rho_v^2}{\sigma(\rho_l - \rho_v)g} \right]^{1/4}. \quad (2.17)$$

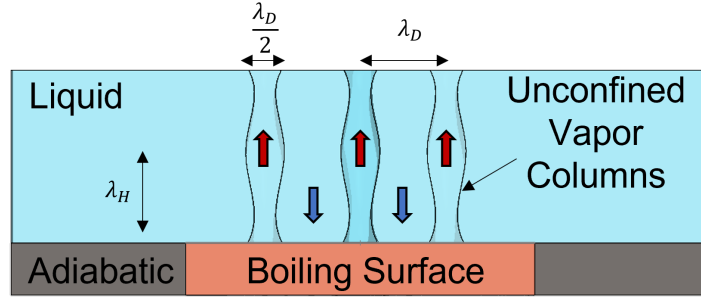


Figure 2.6. Illustrations of vapor columns on a heated surface at CHF (assuming the system is limited by the hydrodynamic instability of the far field liquid-vapor interfaces)

Chang [69] was the first to suggest a link between CHF for pool boiling and the interfacial instability analysis developed by Taylor [70]. Influenced by Chang, Zuber [71] further developed the interface instability approach to explain the mechanisms of CHF for pool boiling. Zuber's model was further refined by Lienhard and Dhir [72] by assuming the vapor columns leaving the boiling surfaces follow the Helmholtz instability at the CHF and are spaced with nodes at the dominant unstable Taylor wavelength, $\lambda_D = 2\pi(3\sigma/[(\rho_l - \rho_v)g])^{1/2}$. Vapor column diameters were also assumed to be half of the vapor column spacing as depicted in Figure 2.6.

Assuming that vapor density is much lower than liquid density, the critical Helmholtz velocity, u_c is

$$u_c = \left[\frac{2\pi\sigma}{\rho_v\lambda} \right]^{1/2}. \quad (2.18)$$

The mean vapor velocity in the column can be calculated using conservation of mass and energy to be

$$u_c = \frac{q''_{CHF}}{\rho_v h_{lv}} \left(\frac{A_{surf}}{A_{col}} \right) = \left(\frac{16}{\pi} \right) \frac{q_{CHF}}{\rho_v h_{lv}}. \quad (2.19)$$

Using the Taylor wavelength most susceptible to instabilities and equating the relations for u_c yields

$$q''_{CHF} = \frac{\pi}{16(3)^{1/4}} \rho_v h_{lv} \left[\frac{\sigma(\rho_l - \rho_v)g}{\rho_v^2} \right]^{1/4} \quad (2.20)$$

The generalizability of the model of Zuber [71] has been criticized [69], [72], [73] since it did not account for geometry, surface conditions, and wettability while experimental data suggested that those factors have a strong influence on CHF. Subsequent investigations adapted Zuber's model when developing CHF correlations for finite boiling surface. Table 2.3 summarizes those CHF correlations to account for additional factors such as wettability, pressure, viscosity, and orientation.

Table 2.2. A summary of modified dimensionless unconfined CHF ratios, $K = \frac{CHF}{\rho_v^{0.5} h_{lv} [\sigma g (\rho_l - \rho_v)]^{1/4}}$, based on Zuber's model [71] including the key physics upon which the models are based.

Author(s)	Dimensionless CHF Ratio	Wettability	Pressure	Viscosity	Orientation
Kirichenko and Chernyakov [74]	$K = 0.171 \frac{(1+0.324e-3\beta^2)^{1/4}}{(0.018\beta)^{1/2}}$	✓			
Ramilison <i>et al.</i> [75]	$K = 0.0044(\pi - \beta)^3 R_a^{0.125}$	✓			
Kim <i>et al.</i> [76]	$K = 0.811 \left(\frac{1+\cos\beta}{16} \right) \left[\frac{2}{\pi} + \frac{\pi}{4}(1 + \cos\beta) + \frac{351.2 \cos\beta}{1+\cos\beta} \left(\frac{R_a}{S_m} \right) \right]^{1/2}$	✓			
Wang <i>et al.</i> [77]	$K = [0.18 - 0.14(P/P_c)^{5.68}]$		✓		
Borishanskii [78]	$K = 0.13 + 4 \left[\frac{\rho_l \sigma^{3/2}}{\mu_l^2 [g(\rho_l - \rho_g)]^{1/2}} \right]^{-2/5}$			✓	
Liao <i>et al.</i> [79]	$K = 0.131 \left[-0.73 + \frac{1.73}{1+10^{-0.021(185.4\theta)}} \right] \left[1 + \frac{55-\beta}{100} (0.56 - 0.0013\theta) \right]$				✓
El-Genk and Bostanci [80]	$K = [(0.229 - 4.27e-4\theta)^{-6} + (0.577 - 2.98e-3\theta)^{-6}]^{-1/6}$				✓
Arik and Bar-Cohen [81]	$K = 0.131(1 - 0.001117\theta + 7.79401e-6\theta^2 - 1.37678e-7\theta^3)$				✓

Models for CHF based purely hydrodynamic instability fail to address effects of the boiling surface wettability while experimental data suggests that surface wettability characteristics significantly effect CHF conditions [82]–[85]. The limitation of the hydrodynamic approach motivated Kandlikar [85] to develop a model for CHF based on the forces on the vapor bubble parallel to the boiling surface. The model considers the change of momentum forces due to evaporation, *vapor recoil*, as the triggering factor for CHF. Kandlikar [85] postulated that the CHF occurs when those forces are balanced resulting in the following relation:

$$q''_{CHF} = \rho_v h_{lv} \frac{1 + \cos \omega}{16} \left[\frac{2}{\pi} + \frac{\pi}{4} (1 + \cos \omega) \cos \theta \right]^{1/2} \left[\frac{\sigma(\rho_l - \rho_v)g}{\rho_v^2} \right]^{1/4}, \quad (2.21)$$

where θ is the angle of the boiling surface relative to the buoyancy direction and ω is the receding contact angle. The CHF model of Kandlikar [85] indicates that CHF decreases as the contact angle increases which is in agreement with experimental trends [73], [86]–[92]. In the extreme case of a entirely non-wetting surface, the nucleate boiling regime is expected to vanish as boiling transitions immediately to film boiling upon incipience.

2.5 Geometrical Size Effect on Boiling

The typical boiling curves demonstrated in Section 2.1 characterize boiling when the characteristic dimension of the heater is large compared to the capillary length of the working fluid, $L_b = \sqrt{\sigma/g(\rho_l - \rho_v)}$. Characteristics of two-phase heat dissipation in finite geometries are significantly different compared to boiling from large surfaces in an unconfined pool. Finite geometries affect the two-phase interface dynamics which affects the flow pattern, wetting dynamics, and, moreover, heat transfer rate. Furthermore, the ebullition cycle mechanism described in Subsection 2.2.2 assumes that the characteristic length is large compared to the bubble departure diameter. Correlation of the departure diameter indicates that typically equation to the capillary length for most systems. Hence, boiling curves for heaters with characteristic length small compared to the capillary length is not expected to follow the classical boiling curve. For instance, Bakhura and Lienhard [93] collected boiling curves for small diameter horizontal heater. The authors reported boiling curve for the small

wire with a monotonic increase in heat flux along with the observation of 'patchy' boiling, where the boiling surface is partially covered in vapor blanket. The fraction of the boiling surface area covered by vapor increases as the applied heat flux increases. that the when the radius of the wire is less than $0.01L_b$ the local minimum and maximum value in the boiling curves vanish. Similarly, Lienhard colleagues [94]–[97] systematically investigated the effect of finite boiling surfaces on the critical heat flux. The study adapted the hydrodynamics instability framework described in subsection 2.2.2 and developed correlations for different shapes as summarized in Table 2.3. The lack of a universal correlation across different shapes suggests that the hydrodynamics instability criteria is not sufficient to identify the triggering mechanism for CHF in finite heater geometries.

Similarly, a small gap spacing above the boiling surface compared to the capillary length, termed 'confined boiling' herein, affects the boiling characteristics. In one of the earliest investigations into confined boiling, Katto and Yokoya [98] found that confined boiling reduces the critical heat flux (CHF) and improves the average heat transfer coefficient compared to unconfined boiling. In particular, boiling of deionized water at atmospheric pressure is sensitive to the confinement gap space for gaps smaller than 2 mm. For gaps of 2 mm and larger, the heat transfer characteristics were similar to unconfined pool boiling [99]. Later investigations observed that, in addition to the confinement gap spacing, the area of confined boiling surface impacts the heat transfer characteristics as well. Specifically, the heat transfer coefficient and critical heat flux both reduced when the diameter of confined boiling surface was increased [100]. Further, confined boiling is less sensitive to heater orientation, microgravity, and surface roughness compared to unconfined boiling [101]–[104]. Yet, the surface wettability does impact confined boiling, as recent work has shown that using a superhydrophobic confinement wall improved the thermal characteristics of confined boiling [105]. The departure from classical boiling characteristics discussed above motivated investigators to develop correlations to characterize the heat transfer rate in confined boiling configurations. Table 2.4 summarizes the empirical correlations for heat transfer rate in terms of the gap spacing, S . Furthermore, owing to the success of the hydrodynamics instability theory in predicting CHF in pool boiling, subsequent investigations adapted Zuber's framework when developing correlations for CHF for confined boiling by including the gap spacing, S , in the empirical

Table 2.3. Modified dimensionless CHF ratios, $K = \frac{CHF}{\rho_v^{0.5} h_{lv} [\sigma g (\rho_l - \rho_v)]^{1/4}}$, based on Zuber's model [71] to account to finite geometrical effect.

Geometry	Correlation	Range of Applicability
Infinite heater flat plat	$K = 1.14$	$L/L_b > 30$
Small Heater of width or diameter L with vertical side walls	$K = \frac{1.14\lambda_D^2}{A_{heater}}$	$9 < L/L_b < 20$
Horizontal cylinder of radius R	$K = 0.89 + 2.27 \exp\left(-3.44\sqrt{\frac{R}{L_b}}\right)$	$R/L_b > 0.15$
Large horizontal cylinder of radius R	$K = 0.90$	$R/L_b > 1.2$
Small horizontal cylinder of radius R	$K = 0.94 \left(\frac{R}{L_b}\right)^{-1/4}$	$0.15 \leq R/L_b \leq 1.2$
Large sphere of radius R	$K = 0.84$	$4.26 \leq R/L_b$
Small sphere of radius R	$K = 1.734 \left(\frac{R}{L_b}\right)^{-1/2}$	$0.15 \leq R/L_b \leq 4.26$
Small horizontal ribbon oriented vertically with side height H - both sides heated	$K = 1.18 \left(\frac{H}{L_b}\right)^{-1/4}$	$0.15 \leq H/L_b \leq 2.96$
Small horizontal ribbon oriented vertically with side height H - back side insulated	$K = 1.4 \left(\frac{H}{L_b}\right)^{-1/4}$	$0.15 \leq H/L_b \leq 5.86$
Small, slender, horizontal cylinder body of arbitrary cross section with transverse perimeter L_p	$K = 1.4 \left(\frac{L_p}{L_b}\right)^{-1/4}$	$0.15 \leq R/L_b \leq 5.86$
Small bluff body with characteristic dimension L	$K = C_0 \left(\frac{L}{L_b}\right)^{-1/2}$	Large L/L_b

correlation for the dimensionless CHF, K . Table 2.5 summarizes those modifications for confined configurations.

Table 2.4. Empirical correlations for confined boiling heat transfer.

Author(s)	Correlation	Range
Kapitz <i>et al.</i> [104]	$Nu = \left(\frac{\mu q_d}{\sigma h_f g \rho_f S} \right)^{1/3}$	$0.1\text{mm} < S < 1\text{mm}$ $5\text{mm} < d < 20\text{mm}$ $10 < Nu < 50$
Kiyomura <i>et al.</i> [106]	$Nu = 154 \left(\frac{c_p \mu_l T_{sat}}{h_l v} \right)^{1.72} \left(\frac{c_p \mu_l}{k_l} \right)^{-0.34} \left(\frac{D_b q''}{\mu_l h_{lv}} \right)^{0.62} \left(\frac{S}{L_b} \right)^{-0.05}$	$0.1\text{mm} < S < 13\text{mm}$ $2.23 < Nu < 167.6$
Cardosa & Passos [107]	$Nu = 30.6 \left(\frac{q''^2}{\rho_g^2 h_{lv}^2 g L_b} \right)^{-0.59} \left(\frac{q''^2 \rho_f L_b}{\rho^2 h_{lv}^2 \sigma} \right)^{-0.08} \left(\frac{c_p \mu_l}{k_l} \right)^{-0.56} \left(\frac{c_p (T_w - T_{sat})}{h_{lv}} \right)^{0.012} \left(\frac{g(\rho_l - \rho_v) S^2}{\sigma} \right)^{0.012}$	$0.1\text{mm} < S < 13\text{mm}$
Chan <i>et al.</i> [108]	$h = h_{nb} \left[1 + 0.3 \left(\frac{g(\rho_l - \rho_v) S^2}{\sigma} \right)^{-0.6} \right]$ $h_{nb} = 55 P_r^{0.12-0.434n(R_p)} (\log_{10} P_r)^{-0.55} M^{-0.5} q''^{0.67}$	$0.3 < Bo < 9.0$
Su <i>et al.</i> [109]	$\frac{q'' - 95673.2 Bo^{0.1} + 98241.2}{\Delta T_{sat}^{0.71} \lambda_l^{3.33}} = 1.907 * 10^{-12} \left(\frac{D}{S} \right)^{0.505} P_r^{1.167} (\rho_v h_{lv} n u_l)^{-2.333} \left(\frac{P}{\sigma} \right)^{2.333}$	$0.9\text{mm} < S < 20\text{mm}$ $D = 100, 300\text{mm}$
Ishibashi & Nishikawa [110]	$Nu = 16 \left(\frac{q''^2 S}{h_{lv} \rho_v \nu^{1.6} * 10^6} \right)^{1/3}$	$0.97\text{mm} < S < 2.7$

Table 2.5. Modified dimensionless CHF ratios, $K = \frac{CHF}{\rho_v^{0.5} h_{lv} [\sigma g (\rho_l - \rho_v)]^{1/4}}$, based on Zuber’s model [71] to account to geometrical confinement effect.

Author(s)	Correlation
Bonjour & Lallemand [111]	$K = \frac{0.134}{1+6.3910^{-5}(\rho_l/\rho_v)^{1.343}P_r^{0.252}(L_H/S)^{1.517}}$
Katto & Kosho [112]	$K = \frac{0.18}{1+0.00918(\rho_v/\rho_l)^{0.14}[g\frac{(\rho_l-\rho_v)d^2}{\sigma}]^{0.5}(d/S)}$
Kim & Suh [113]	$K = \frac{0.17}{1+6.8*10^{-4}(\rho_l/\rho_v)^{0.62}(D_{eq}/S)}$
Kim <i>et al.</i> [114]	$K = 0.131(0.6028S^{0.3694})$
Misale <i>et al.</i> [101]	$K = 0.185 \left(\frac{1}{1+71.43e^{-1.32S}} \right)$
Monde <i>et al.</i> [115]	$K = \frac{0.16}{1+6.7*10^{-4}(\rho_l/\rho_v)^{0.6}(L_H/S)}$

2.6 Summary and Relation to this Work

The understanding of boiling has substantially increased due to the past investigations discussed above. Section 2.1 demonstrated how the coefficient of proportionality between the boiling surface superheat, ΔT , and the applied heat flux, q , (*i.e.* boiling curves) has been used to define the boiling characteristics. Due to the complex nature of boiling, typically the boiling phenomena is divided into regimes to simplify the appropriate governing mechanisms. In fact, the boiling regimes are configuration dependent. For example, pool boiling and flow boiling exhibit different boiling regimes. While confined boiling relies on buoyancy for the departure of the generated bubbles, similar to pool boiling, the confinement wall induces a significant local fluid flow parallel to the boiling surface. Hence, unique boiling regimes are expected for confined boiling. Chapter 3 identifies those unique confined boiling regimes. One of the main thermal metrics for boiling is the heat transfer coefficient. Section 2.2.1 summarized the mechanisms for the main predictive models for the boiling heat transfer coefficient. Mainly, a convection analogy is made assuming that the generated bubbles induce location fluid motion near the boiling surface which facilitates the convective transport of heat. Section 2.2.1 reviewed different characteristic lengths and velocities used in a scaling based analysis for boiling. However, in each model a specific mechanism was the base of the developed model. For examples, one model postulates that bubbles behave as micropumps drawing cold ambient fluid. Another model treats the vapor leaving the surface as an in-

verted stagnation flow. Chapter 4 explores the appropriate mechanisms of heat transfer in confined boiling which can serve as a base for a future predictive models for the confined boiling heat transfer coefficient. Furthermore, section 2.3 summarized the common approaches for enhancing the boiling heat transfer coefficient through micro-/nano-modification of the boiling surface. The enhancements demonstrated tends to degrade due to fouling, thermal stresses, and absorbed material. Chapter 4 provides an alternative enhancement technique through confinement where the nucleation onset condition reviewed in section 2.2.2 is used to distinguish between different enhancement mechanisms.

Lastly, section 2.4 reviewed the approaches used to predict the critical heat flux that triggers the transition into film boiling. Among the widely accepted analytical approaches use is the hydrodynamics instability. This framework is used include the influence of factors that are not accounted for in the original development of the theory such as wettability, orientation, and pressure. Section 2.5 demonstrated how subsequent investigations adapted the hydrodynamics instability framework to predict the geometrical confinement effect on CHF. However, chapter 5 re-evaluates the applicability of existing CHF frameworks and proposes a new framework specifically for confinement configurations.

In brief, confinement significantly alter the boiling characteristics. Hence, a deeper mechanistic understanding of boiling in extremely compact spaces is crucial for designing effective compact two-phase thermal management. This deeper understanding will facilitate the modification of the applicable extensive work that have been develop for unconfined boiling to accommodate the effect of confinement. More broadly, further research in needed to develop design guidelines for extremely compact two-phase thermal management solutions. for extremely compact two-phase thermal management solutions.

3. BOILING IN MICROSCALE GAPS¹

Thermal management is one of the major operational concerns for data centers and accounts for a significant fraction of total power consumption. Passive immersion cooling solutions have been explored owing to their potential for offering low overall thermal resistance in very dense rack configurations where there is no room for conventional heat sinks between printed circuit boards. Further, in practice, regions of high heat flux are localized to where processing units are positioned. Non-uniform heating, as well as local hot spots, could affect thermal performance as a result of the need for rewetting of the surface with liquid during boiling. This work explores immersion cooling in submillimeter confined liquid filled gaps with localized heat sources. Specifically, this work investigates the thermofluidic characteristics of highly confined boiling surfaces. A camera is used to visualize the two-phase flow regimes and instabilities that occur prior to critical heat flux (CHF) limits. Two distinct boiling regimes are observed (namely, intermittent boiling and partial dryout). Both the heated fraction of the area within the confined region and the gap spacing affect the CHF values and thermal performance prior to CHF. The optimum thermal performance, in terms of the surface superheat, is experimentally observed for a confinement corresponding to a Bond number of 0.2. However, at this optimum condition based on surface superheat, the CHF is significantly reduced to 27 % of the unconfined CHF limit. Significant additional reductions in the CHF are also experimentally observed when the adiabatic confinement surface is extended beyond the heater edge. This additional fundamental understanding of the impact of spatial confinement on the thermal performance of immersion cooling has broad implications for two-phase thermal management solutions.

¹This section is reproduced from A. A. Alsaati, D. M. Warsinger, J. A. Weibel, and A. M. Marconnet, "Confined Immersion Cooling in Microscale Gaps," 2020 19th IEEE Intersociety Conference on Thermal and Thermomechanical Phenomena in Electronic Systems (ITherm), Orlando, FL, USA, 2020, pp. 475-481, DOI:10.1109/ITherm45881.2020.9190616

CRediT Authorship Contribution Statement: A. A. Alsaati: Conceptualization, Data Curation, Formal Analysis, Investigation, Methodology, Software, Validation, Visualization, Writing - original draft, and Writing - Review & Editing. D. M. Warsinger: Project Administration, Resources, Supervision, and Writing - Review & Editing. J. A. Weibel: Conceptualization, Funding Acquisition, Project Administration, Resources, Supervision, and Writing - Review & Editing. A. M. Marconnet: Conceptualization, Funding Acquisition, Project Administration, Resources, Supervision, and Writing - Review & Editing.

3.1 Introduction

In the modern digital era, data centers are an indispensable resource for almost any organization. The global market for cloud and data center networks was valued at \$17 billion in 2017 and growing annually at 15% [116]. US-based data centers alone are projected to consume 73 billion kWh in 2020 (an equivalent to 1.8% of total US electricity consumption) [117], [118]. Cooling is estimated to account for nearly a quarter of the total power consumption of data centers [119]. In addition to energy cost, inadequate data center cooling solutions limit computing performance and reliability. Since the early 1990's, thermal management of complementary metal-oxide-semiconductor (CMOS) based processing electronics have increasingly become the bottleneck for increasing the processing power [120]. New products and improved controls on air cooling of data centers have expanded the performance limits while providing energy savings. However, room-based approaches that condition the bulk air do not exploit the performance advantages of liquid cooling solutions applied nearer the hot surfaces of high-power electronics [121]. Additionally, rack-based liquid-cooling solutions provide the flexibility for segmenting the cooling load within the data center [117].

Currently, two-phase liquid cooling is an active research area both in academia and industry due to the improved maximum heat flux dissipation limits. In fact, researchers have demonstrated intra-chip flow boiling solutions using dielectric coolants for hotspot heat fluxes up to 2500 W cm^{-2} [122]–[127]. However, a radical change to electronics packaging approaches would be required to achieve this level of thermal performance. Any active two-phase cooling approach would further require pumps, hoses, manifolds, couplings, and other components. Passive immersion cooling has the potential to simplify two-phase cooling design by eliminating much of this additional hardware. Immersion cooling solutions become viable and attractive for cooling computing systems with very high rack packing density [128].

Passive liquid immersion cooling solutions require an understanding of boiling phenomena in highly confined spaces [129], [130]. In comparison to the extensive research on unconfined pool boiling, the existing literature focusing on confined boiling is sparse. Katto et al. [99] performed one of the earliest confined boiling studies and showed that confinement improves the heat transfer coefficient while reducing CHF. Later studies demonstrated that confined

boiling has less sensitivity to the surface orientation [131] and roughness [104] compared to unconfined conditions; however, nanostructured surfaces significantly improve the heat transfer coefficient of confined boiling [132]. Furthermore, the area of confined boiling has been found to be inversely correlated to CHF for uniform heating [100]. On the other hand, confinement has been shown to reduce heat transfer coefficient for subcooled conditions [133]. Further mechanistic understanding of the confined boiling regimes leading to these trends, as well as the effect of non-uniform heat fluxes, are crucial for implementing confined immersion cooling.

The aim of this study is to identify and characterize boiling regimes for confined boiling and to understand the effect of heat source size with respect to the confined zone. We measure boiling curves for various confinement levels (*i.e.*, the distance between the heated surface and a confining plate) and visually observe the boiling regimes to understand the heat transfer enhancement mechanisms. The study further aims to identify the confinement geometry that results in a minimum surface superheat.

3.2 Experimental Setup

Figure 3.1 shows the experimental facility for the confined immersion cooling experiments. The facility enables measurement of the boiling curve (heat flux and surface superheat) while controlling the confinement gap size, S , and the confinement diameter, D_c , and fixing the boiling diameter, D_b . To elucidate the confined boiling characteristics, the facility is equipped with a camera for visualizing the dynamic two-phase interfaces within the confinement gap.

The 25.4 mm-diameter boiling surface is oriented horizontally at the bottom of a double-wall vacuum-insulated quartz glass cylinder chamber with an approximate volume of 500 m L^{-1} and inner diameter of 75 mm. The chamber is filled with deionized water ($0.37 \text{ }\mu\text{S cm}^{-1}$) consistently to a level of 10 cm above boiling surface.

A 1000 W cartridge heater (Watlow Firerod 1039; 1.27 cm diameter, 7.62 cm length) supplies heat to the boiling surface through the 31.75 mm-diameter and 107.95 mm-height copper rod. Three T-type thermocouples (Omega; $\pm 0.3 \text{ K}$) embedded at the centerline of the copper reference rod, spaced 6.35 mm apart along rod axis, measure the temperature

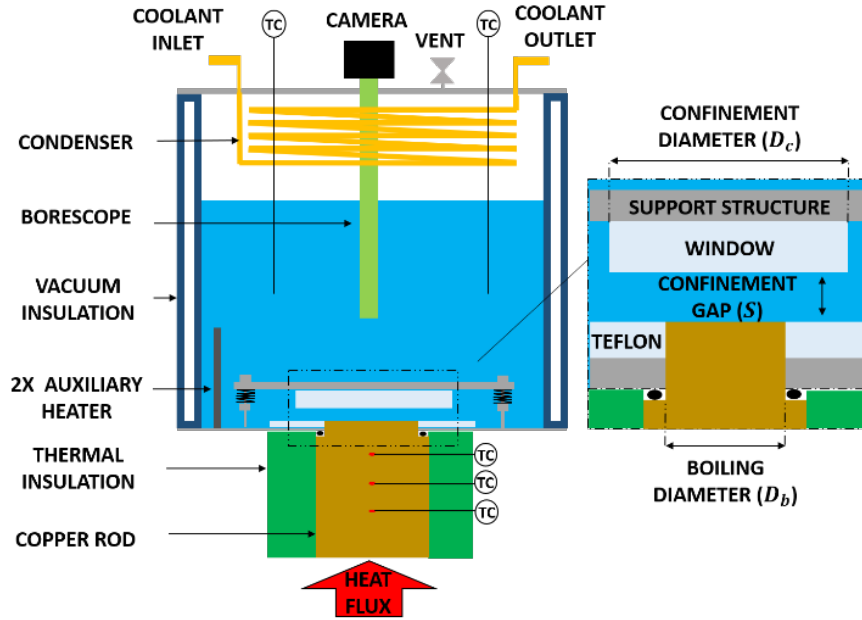


Figure 3.1. Schematic illustration of the confined boiling experimental facility. Cartridge heaters (not shown) provide heat to the copper rod from below. The heat flux and the boiling surface temperature are measured from thermocouples embedded in the copper rod. Thermal insulation surrounding the rod minimizes the radial temperature gradient and heat losses. An adjustable glass window confines boiling to within a controlled gap above the boiling surface. A camera captures the two-phase interfaces in the confinement gap as viewed through a rigid borescope. The pool of water is maintained at the saturation temperature using two auxiliary cartridge heaters with temperature control based on the thermocouples within the pool.

gradient, which is linearly correlated to the heat flux at steady state according to Fourier's law assuming one-dimensional heat flow. The radial non-uniformity in temperature at the thermocouple locations is numerically estimated to be more than an order of magnitude less than the thermocouple uncertainty. Using the measured temperature gradient to calculate the heat flux accounts for heat losses through the insulation. A DAQ (Labjack U6pro) logs the temperature measurements through Labview at a 1 Hz sampling rate. The surface temperature is linearly extrapolated from the reference rod temperature measurements using a (numerically estimated) thermal resistance of the stepped cylinder of copper beyond the topmost thermocouple which is placed 12.7 mm below the boiling surface. To limit radial conduction within the reference rod, a 1.8 cm-thick microporous insulation (MICROSIL)

surrounds the rod. The reference rod is sealed to the boiling chamber with a Viton O-ring at the step in the rod diameter.

In each experiment, a 6.35 mm-thick circular glass window is suspended above the boiling surface with an adjustable gap size, S , to provide confinement of the fluid above the boiling surface. The diameter of the window varies from the same diameter as the copper rod (25.4 mm) to 50.8 mm in diameter; this is used to control and study the effect of the relative area of the boiling surface to the confined region. The step of the copper rod protrudes 5.5 mm above the chamber base. A Teflon ring flush with the top of the boiling surface maintains a constant confinement gap throughout an extended region beyond the confinement window, providing an adiabatic boundary around the periphery of the boiling surface (see Figure 1 inset). Both the inner and outer diameter of the Teflon ring are sealed with a high temperature sealant (Permatex 81160). Three spring-loaded set screws adjust and level the confinement gap with a resolution of 2.2 $\mu\text{m}/\text{deg}$. The confinement gap size is adjusted using reference stainless steel shims. The glass window and glass boiling chamber permit optical access to the two-phase test section. The two-phase interfaces are visualized at 480 frames per second through a rigid borescope (Hawkeye Pro Hardy) where the objective lens is submerged in the liquid pool.

A chiller (PolyScience AD07R-40-A11B) circulates 90 °C cooling water through a copper coil heat exchanger enclosed inside the top of the boiling chamber to condense vapor back to the liquid pool. The facility body is electrically grounded to prevent charge accumulation and reduce measurement noise. Two submerged auxiliary cartridge heaters (Omega HDC19110; 0.32 cm diameter, 8.89 cm length) along with two T-type thermocouples (Omega; ± 0.3 K) maintain the liquid pool at saturation conditions under atmospheric pressure. The chamber is maintained at atmospheric pressure through an open vent as shown in Figure 3.1.

Prior to collecting boiling data, the working fluid is boiled vigorously using the auxiliary heaters to purge all non-condensable gasses trapped in the confined gap and dissolved in the liquid. The degassing process is maintained for a minimum of 2 hr producing a saturated water vapor condition. The working fluid is considered degassed when the boiling temperature reaches within 0.3 °C of the pure liquid saturation temperature. Once the fluid is degassed, the auxiliary heaters are controlled to maintain saturation condition in the chamber.

The boiling curve data points correspond to a fixed input heat flux where temperature measurements are stable (*i.e.*, temperature measurements change less than 0.1 °C/min for a duration of 10 min). After reaching steady state for every data point on the boiling curve, the camera records the two-phase interfaces during boiling. This steady state measurement is repeated with increasing input powers to obtain the entire boiling curve for each case presented in the results. At each increment, the main heater is turned off momentarily (20 s) and then powered to the next heat flux level. During testing, the heat flux is increased until CHF is reached, as indicated by a very steep temperature rise and confirmed via visualization of film boiling. Finer power increments are used around the incipience of boiling and CHF to improve the resolution of identifying these transitions.

3.3 Results and Discussion

3.3.1 Unconfined Pool Boiling Benchmark Testing

Prior to conducting the confined boiling measurements, the experiments are performed for an unconfined pool boiling condition without the glass window in place. Four repeated boiling curves plotting the applied heat flux (q'') as a function of the surface superheat ($T_b - T_{sat}$) are obtained to demonstrate repeatability (see Figure 3.2). The highest heat flux value in each measurement run is taken as the CHF, as the next increment in heat flux results in complete coverage of the boiling surface with a vapor film. The variation of measured CHF values for this unconfined boiling configuration is found to be within $\pm 6.6\%$ of average. The average measured CHF value is also compared to the theoretical prediction proposed by Lienhard and Dhir [72]:

$$CHF = \frac{\pi}{24} \rho_v h_{lv} \left(\frac{\sigma(\rho_l - \rho_v)g}{\rho_v^2} \right)^{\frac{1}{4}}. \quad (3.1)$$

The average measured CHF value (96.8 W/cm²) is within 12.5% of theoretical prediction (110.7 W/cm²). These unconfined boiling curves serve as a baseline for comparison to the confined boiling cases.

3.3.2 Confined Boiling Characterization

Confined boiling curves are measured for four confinement gaps ranging from 128 μm to 762 μm . For this set of tests, the confinement window has the same area as the boiling surface ($A_b/A_c = 1$) and is aligned directly above. For the presentation of confined boiling data, the gap size, S , is normalized by the capillary length, L_c , of the fluid to yield the nondimensional Bond number,

$$Bo = \frac{S}{L_c} = \frac{S}{\sqrt{\frac{\sigma}{g(\rho_l - \rho_v)}}}. \quad (3.2)$$

A Bond number much larger than unity indicates that the size vapor bubbles that depart from the boiling surface are much smaller than the gap size (or in the case of unconfined boiling, freely depart from the surface). However, for Bond numbers on the order of unity or less, these length scales are similar and the confinement wall will interface with the vapor

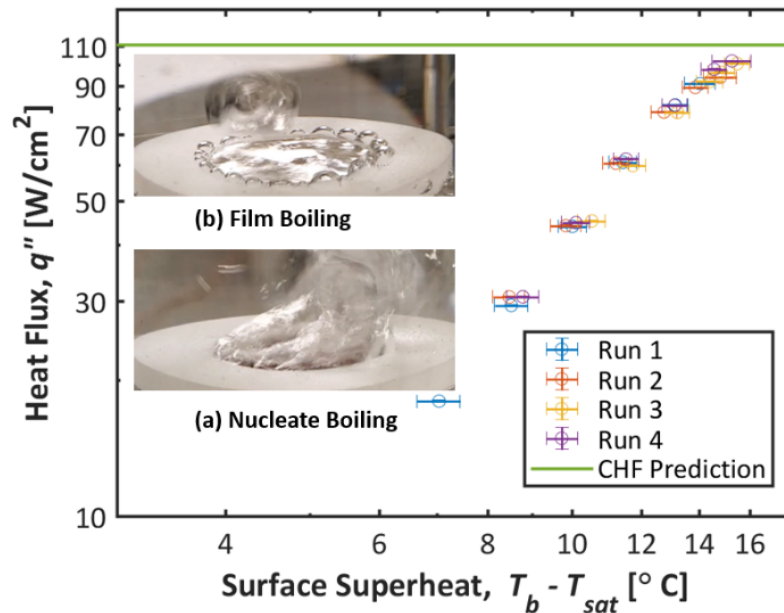


Figure 3.2. Experimental facility repeatability tests for the unconfined pool boiling curve. The highest heat flux value in each run represents the critical heat flux (CHF) compared to the theoretical prediction (green line). The inset images show the transition from (a) nucleate boiling to (b) film boiling following an increment to a heat flux higher than CHF.

bubbles generated at the boiling surface [99]. In this study, a range of Bond number from 0.05 (corresponding to $S = 128 \text{ }\mu\text{m}$) to 0.30 ($S = 762 \text{ }\mu\text{m}$) is investigated.

Boiling curves are shown in Figure 3 for multiple different Bond numbers (*i.e.*, degrees of confinement). The unconfined boiling curve is plotted as a dashed line for reference. As a general trend, the surface superheat is lower for the confined cases compared to the unconfined boiling case at similar heat fluxes. However, the critical heat flux is significantly reduced when boiling is confined. From interpretation of the boiling curve data alongside the optical visualizations, two distinct boiling regimes are identified for confined boiling beyond natural convection regime: intermittent boiling and partial dryout.

Like unconfined boiling, the natural convection regime (gray shaded region of Figure 3.3) is characterized by a lack of boiling within the gap at elevated surface superheats. At low heat flux values (approximately less than 10% of confined boiling CHF), heat is dissipated through conduction and single-phase natural convection. At higher heat flux values, the surface superheat becomes large enough to initiate nucleation within the confined space.

Upon vapor nucleation, there is a transition to the intermittent boiling regime (green shaded region of Figure 3.3). This boiling regime exhibits a time-periodic oscillatory behavior at steady state, as observed both through the transient boiling surface temperature measurements and the visualizations (see Figure 3.4). During these oscillations, the temperature of the liquid within the confined cavity rises until it reaches the minimum required superheat to achieve nucleation. Then, vapor bubbles nucleate and expand radially outward until reaching the outer periphery of the confinement window, where surface tension and buoyancy forces facilitate extraction of vapor from the confined region into the liquid pool. Consequently, liquid from the surrounding pool flows radially inward to fill the volume displaced by the departed vapor bubble. This capillary-assisted radial inward flow of liquid at the saturation temperature has a quenching effect on the boiling surface, lowering its temperature below the required nucleation temperature. This process repeats in a cyclic manner. As the heat flux increases, the frequency of this oscillatory behavior increases. The boiling curve in this complete rewetting regime exhibits a negative slope (*i.e.*, reducing time-averaged superheat with increasing heat flux) as a result of the higher quenching frequencies at higher heat fluxes.

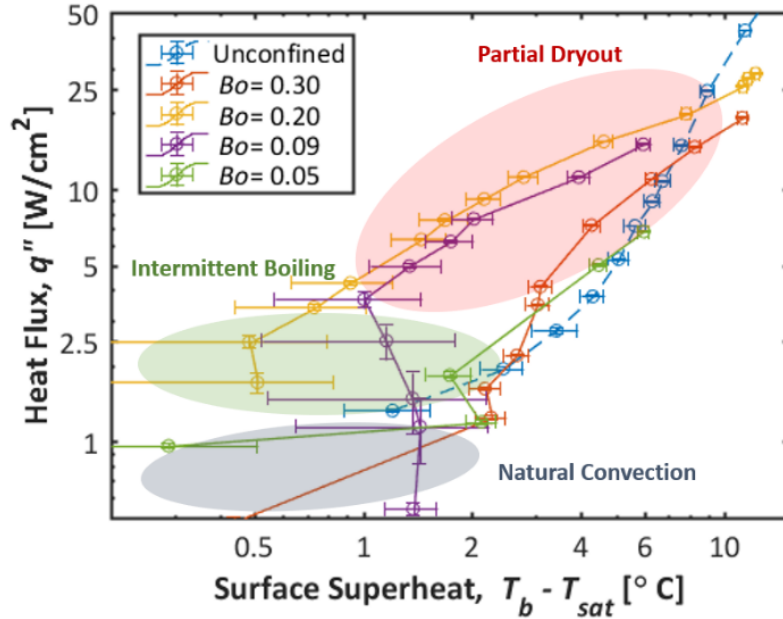


Figure 3.3. Boiling curve for different nondimensional confinement gaps sizes ($Bo = S/L$) are shown as solid lines. Natural convection (gray shaded region) is observed at low heat fluxes where no nucleation sites are activated. During intermittent boiling (shaded in green), vapor is generated slowly enough that the entire boiling surface is able to rewet following periodic vapor departure from the gap. Finally, as the vapor generation frequency increases, the boiling transition to partial dryout regime (shaded in red) where regions of the boiling surface remain continually covered with vapor. The unconfined boiling curve is shown in blue as a dashed line for reference (regimes do not apply).

As the frequency of vapor generation further increases at higher heat fluxes, the capillary forces are insufficient to overcome the viscous resistance and maintain complete rewetting of the surface with liquid as vapor escapes the confinement gap. Consequently, some regions of the boiling surface remain covered with vapor and the boiling behavior transitions into the partial dryout regime (red shaded region of Figure 3.3). The dry area is most often observed at the center of the boiling surface – that is, the locations with the largest distance from the confinement window edge. As observed from the visualizations, the percentage of dry area to wetted area increases as heat flux values increases, resulting in higher average steady state temperatures as demonstrated in the confined boiling curves. Confinement has a severe deleterious effect on the critical heat flux, with a severity that depends on the confinement

gap size. Nevertheless, of all confinement gaps tested, the maximum measured CHF is only 27% of the unconfined CHF.

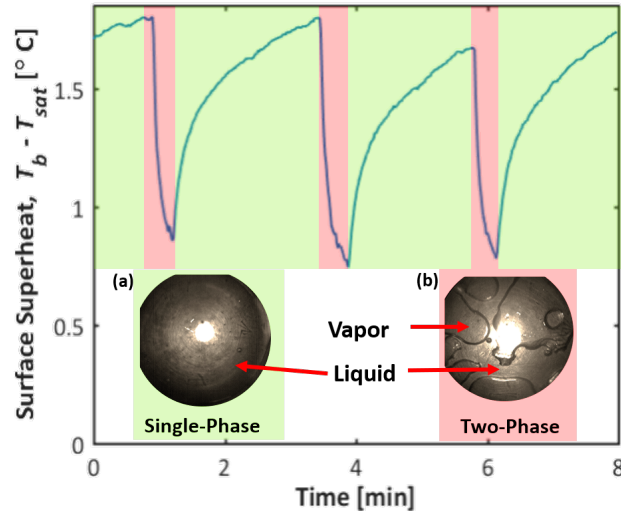


Figure 3.4. Surface temperature oscillations in the intermittent boiling regime ($Bo = 0.09$, $q''=1.5 \text{ W cm}^{-2}$). In the portions of the data where the surface temperature rises with time, the confined liquid is heated without phase change (inset (a)) until the minimum required superheat for nucleation is reached. Inset (b) illustrates the nucleation of vapor bubbles that escape from confinement region and are replaced by a sudden inrush of saturated liquid from surrounding pool that quenches the boiling surface.

3.3.3 Confined Boiling Heat Transfer Enhancement

As demonstrated with the boiling curves (Figure 3.3), confined boiling typically maintains the surface at a lower temperature compared to unconfined boiling prior to CHF. The enhancement in confined heat transfer is attributed to two potential mechanisms illustrated in Figure 3.5. The high heat transfer rates associated with nucleate boiling is widely attributed to microlayer evaporation near the three-phase contact line [30], [134]. In confined boiling, the confinement window above the boiling surface restricts the vapor bubble growth normal to the boiling surface. Hence, the vapor bubble is forced to grow radially along the boiling surface from the point of nucleation. This elongates the thin liquid layer on the boiling surface underneath the bubble (also known as the microlayer); see Figure 3.5 (a). As

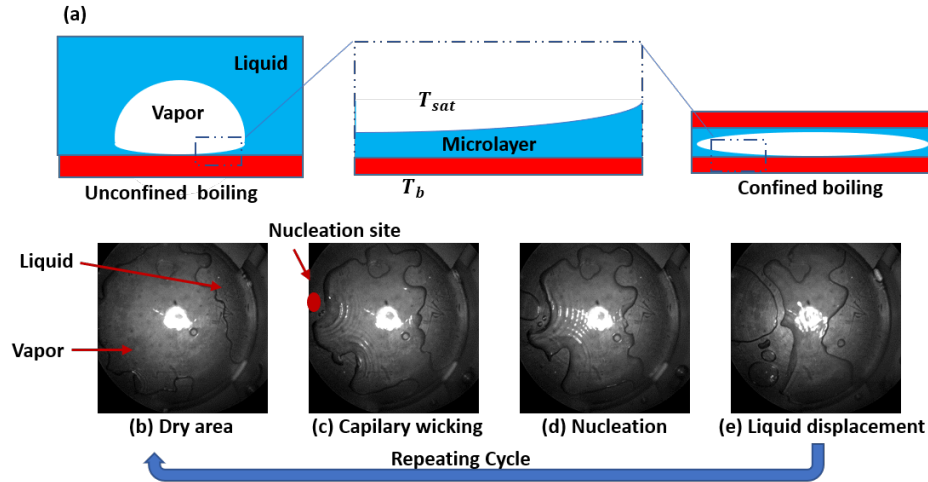


Figure 3.5. Confined boiling heat transfer enhancement mechanisms. (a) Confinement induces radial growth of vapor bubbles enlarging the microlayer coverage compared to unconfined boiling. (b-e) A time series of images that illustrate nucleation-enhanced rewetting where the volume expansion during phase change at nucleation site (red dot) displaces liquid from wet areas to dry areas.

a result, confined vapor bubbles have larger microlayer areas compared to the unconfined case where bubbles can freely depart from the boiling surface.

The second enhancement mechanism is the nucleation-enhanced rewetting. Vapor nucleation first occurs on a portion of the confinement gap filled with liquid. Rapid volume expansion due to phase change at a nucleation site is observed to force liquid to rewet dry regions of the boiling surface, as shown in the time series of images in Figure 3.5 (b-d). As a result, dry spots reside on the boiling surface for a shorter duration, lowering the average surface temperature.

3.3.4 Impact of Confinement Gap and Window Size

Both the fraction of the area within the confined region heated by the boiling surface (A_b/A_c) and gap spacing (S) affect the CHF values and thermal performance prior CHF.

In practice, regions of high heat flux generation on immersion-cooled electronic boards are localized where processing units are positioned. To understand how the relative size of localized heated regions affect the thermal performance of highly confined immersion

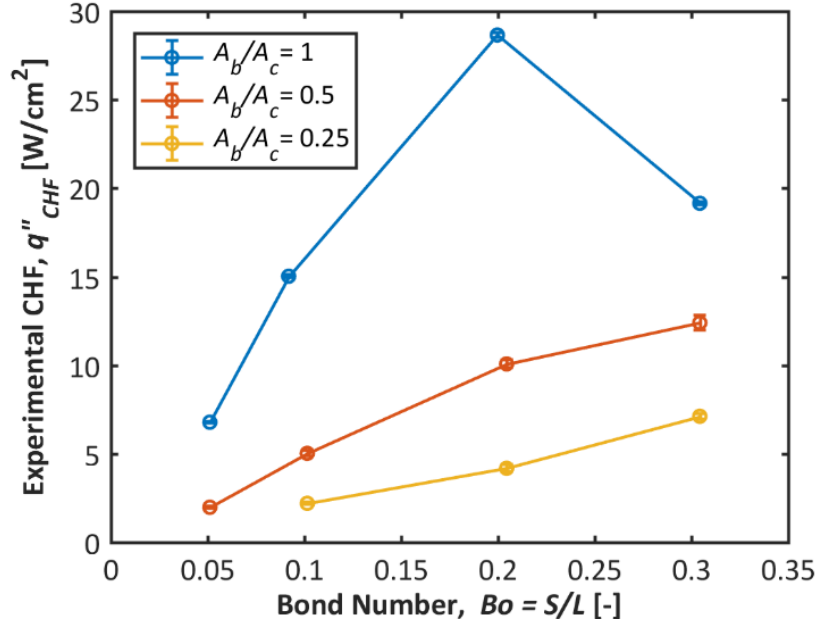


Figure 3.6. Influence of confinement gap size on the CHF for differing fractions of the area within the confined region heated by the boiling surface.

cooling solutions, boiling curves are obtained for cases where the confinement window size is extended beyond the heater edge. This study investigates an extension range from $A_b/A_c = 1$ to $A_b/A_c = 0.25$. The results indicate that positioning heat sources further from the edge of the confinement region has detrimental consequences on the performance under confined boiling conditions. Generally, the boiling curves for the extended confinement window size (not shown) illustrate the same boiling regimes previously discussed. However, at any given degree of confinement, CHF is observed to be significantly lowered when the confinement window is extended, as shown in Figure 3.6.

The thermal performance of confined boiling is highly sensitive to confinement. Two physical phenomena are correlated to the degree of confinement: the capillary pressure generated in the gap that assists rewetting and the counteracting viscous resistance. To illustrate the impact of confinement on the boiling surface temperature, Figure 3.7 illustrates the interpolated surface superheats linearly interpolated from the boiling curves for multiple constant heat fluxes as a function of Bond number for (a) $A_b/A_c = 1$ and (b) $A_b/A_c = 0.25$. Consistently, there is a local minimum in surface superheat for the $Bo = 0.2$ indicating a tradeoff

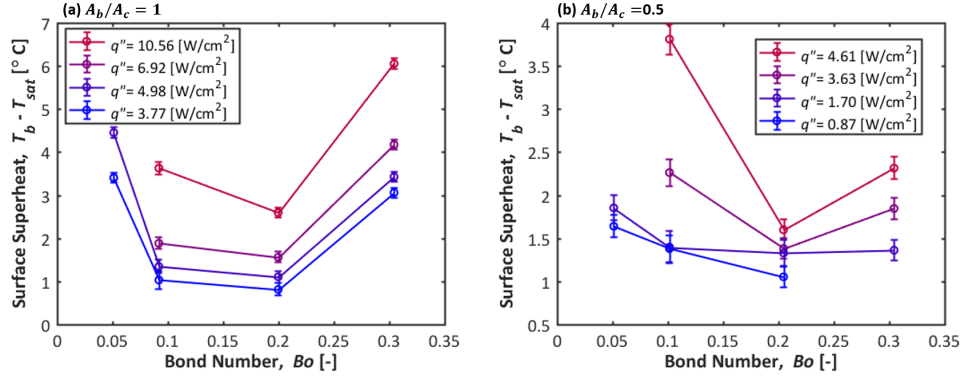


Figure 3.7. Influence of confinement gap size on the boiling surface superheat for differing heat fluxes. Cases are shown where (a) the boiling surface and confinement window are the same diameter and (b) where the boiling surface area is 1/2 of the confinement window area. A local minimum is observed near $Bo = 0.2$.

in the available capillary pressure and viscous resistance, which scale differently with the gap size S . At the minimum superheat, the confined fluid demonstrates the maximum ability for rewetting. Similar trends with Bond number are observed for the case where the confinement window extends beyond the boiling surface. These preliminary experimental results indicate that the optimum confinement gap is not sensitive to the heat flux or extension of the confinement area.

3.4 Summary

Boiling has been experimentally investigated under extremely confined gaps from 128 μm to 762 μm . Two distinct boiling regimes are identified. Similar to unconfined boiling, at low heat fluxes, heat is dissipated by conduction and natural convection. Once the boiling surface temperature reaches a minimum required superheat for nucleation, the boiling transitions into the intermittent boiling regime. This regime exhibits a time-periodic oscillatory behavior. Following vapor bubble departure from the confinement region, rewetting liquid from the surrounding pool lowers the surface superheat and boiling ceases momentarily until the surface heats back up to the nucleation temperature. In this regime, higher heat flux values corresponded to high vapor generation frequencies, higher surface quenching frequencies, and lower time-averaged surface temperatures. Finally, in the partial dryout regime at

higher heat fluxes, portions of the surface remain continually dried out, where the capillary forces are insufficient to overcome the viscous resistances necessary to completely rewet the surface as vapor is extracted from the gap at a high velocity.

Compared to unconfined pool boiling, the average confined boiling surface temperatures are lower at similar heat flux values. Nucleation-enhanced rewetting and a larger microlayer area are proposed to be the mechanisms for the enhanced thermal performance in confined boiling and merit further investigation. The optimum thermal performance is experimentally observed for a confinement gap size corresponding to a Bond number of 0.2. Despite a promising surface temperature reduction, the CHF for this optimum confinement gap size is only 27% of the unconfined CHF. Even more severe reductions in CHF are observed when the confinement region is extended to an area larger than the heater. Further investigation is recommended to improve the surface rewetting and increase CHF while preserving the heat transfer enhancement.

This improved fundamental understanding of geometrically confined boiling is important for the design of high-rack-density immersion cooling thermal solutions for data centers and other compact two-phase thermal management solutions.

4. STEM BUBBLES BOILING¹

Boiling has long been sought as the heat dissipation mechanism for a wide variety of compact thermal management applications owing to low-resistance heat transport, high heat flux limits, and surface isothermalization. This work aims to elucidate the thermofluidic transport mechanisms of boiling in extremely confined gaps through experimental measure of the temporal evolution of heat fluxes and surface temperatures during deionized water boiling, as well as high-speed visualization of bubble formation. The flow visualizations reveal small residual pockets of vapor, termed ‘stem bubbles’ herein, that remain on the boiling surface through a pinch-off process vapor escapes through the edges of the confined heated region. These stem bubbles act as seeds for vapor growth in the next phase of the boiling process and dictate the boiling performance for extremely confined boiling as defined based on a dimensionless ratio of the gap spacing to capillary length ($Bo \leq 0.35 - 0.5$). This conclusion is supported by the thermal response of the surface, namely, because activation of nucleation sites is not required for stem bubble boiling, phase change occurs at a reduced surface superheat at a given heat flux compared to nucleate boiling. Criteria for the dimensionless confinement gap spacing are identified to harness this improved heat transfer rate of the stem bubble boiling regime. This new understanding of boiling in extremely confined gaps offers a new direction to design compact two-phase thermal management solutions through utilizing the unique enhancements provided by the vapor stem bubble boiling regime.

4.1 Introduction

The performance of various electronic systems including data centers, supercomputers, and power electronics depends on the ability to maintain device temperature below a set limit

¹This section is reproduced from A. A. Alsaati,, D. M. Warsinger, J. A. Weibel, and A. M. Marconnet, “Vapor Stem Bubbles as the Dominant Heat Transfer Enhancement Mechanism in Extremely Confined Boiling”, *International Journal of Heat and Mass Transfer*, vol 177, 121520, 2021. DOI:10.1016/j.ijheat-masstransfer.2021.121520

CRedit Authorship Contribution Statement: A. A. Alsaati: Conceptualization, Data Curation, Formal Analysis, Investigation, Methodology, Software, Validation, Visualization, Writing - original draft, and Writing - Review & Editing. D. M. Warsinger: Project Administration, Resources, Supervision, and Writing - Review & Editing. J. A. Weibel: Conceptualization, Funding Acquisition, Project Administration, Resources, Supervision, and Writing - Review & Editing. A. M. Marconnet: Conceptualization, Funding Acquisition, Project Administration, Resources, Supervision, and Writing - Review & Editing.

while dissipating a large amount of waste heat [135]–[141]. For many years, air-cooled heat sinks and single-phase liquid cold plates have been relied upon to dissipate the heat generated. However, the trend of electronic component miniaturization has driven up heat fluxes to levels where these traditional methods fail to maintain safe operating temperatures. Thermal management using two-phase cooling schemes holds promise to maintain device temperatures within the allowed limits while dissipating higher heat fluxes owing to the latent heat of the cooling. Decades of research on two-phase thermal management solutions, both passive (*i.e.*, vapor chambers [142], heat pipes [143], and immersion cooling [144]) and active (*i.e.*, flow boiling based heat sinks [145]), have significantly matured these technologies. However, aggressive recent trends of embedded cooling, where the coolant flows within the die or package, in addition to the tendency to heterogeneously integrate multiple electronic devices within a single package, poses significant geometrical limitations on the available space in which two-phase cooling solutions can be implemented, motivating a further investigation into the implications of extreme geometric confinement on vapor generation mechanisms during boiling.

Nucleate boiling is the target regime of operation because of it offers the highest heat transfer coefficient in pool boiling. Improving nucleate boiling performance has motivated numerous enhancement techniques that use surface modifications to extend surface area [146], increase nucleation site density [147], and improve surface wicking [148]. These studies generally characterize the bubble nucleation behavior and performance enhancement in unconfined conditions, that is, from a boiling surface submerged in a large pool such that the vapor formed is not affected by the surrounding geometry. On the other hand, in active flow boiling schemes, the coolant is typically pumped through small channels, such that the vapor forms two-phase regimes that are well-known to be affected by the degree of geometric confinement [149]–[152]. In confined flow boiling, vapor bubbles span the entire channel cross section; the highest heat transfer coefficient is achieved in the annular flow regime, where bubble nucleation is suppressed, and the main phase change mechanism is evaporation from a thin liquid film surrounding the vapor core. The current investigation, and following review of the literature, focuses on boiling in confined gaps where there is no active pumping. Despite being entirely passive, this situation shares some traits of confined flow boiling in

that the volumetric expansion of the fluid during phase change in extremely confined spaces induces a significant local fluid flow where the vapor bubbles are highly confined by the surrounding geometry. Therefore, confined boiling is of interest as a means to passively achieve enhanced heat transfer coefficients beyond unconfined nucleate boiling.

Characteristics of two-phase heat dissipation in confined spaces are different compared to boiling from large surfaces in an unconfined pool. Confinement of the fluid affects the two-phase interface dynamics which affects the flow pattern, wetting dynamics, and, moreover, heat transfer rate. In one of the earliest investigations into confined boiling, Katto and Yokoya [98] found that confined boiling reduces the critical heat flux (CHF) and improves the average heat transfer coefficient compared to unconfined boiling. In particular, boiling of deionized water at atmospheric pressure is sensitive to the confinement gap space for gaps smaller than 2 mm. At gaps of 2 mm and above, the heat transfer characteristics were similar to unconfined pool boiling [99]. Later investigations observed that, in addition to the confinement gap spacing, the area of confined boiling surface impacts the heat transfer characteristics as well. Specifically, the heat transfer coefficient and critical heat flux both reduced when the diameter of confined boiling surface was increased [100]. Further, confined boiling is less sensitive to heater orientation, microgravity, and surface roughness compared to unconfined boiling [101]–[104]. Yet, the surface wettability does impact confined boiling, as recent work has shown that using a superhydrophobic confinement wall improved the thermal characteristics of confined boiling [105].

Since Katto and Yokoya [98] observed that the superheat of the boiling surface reduces as the confinement gap becomes smaller than the bubble detachment diameter, scholars have been attributing the enhancement in heat transfer coefficient to the deformation of the vapor bubble by the confinement plate which results in the broadening of its microlayer [98]–[105]. This microlayer theory is rooted in the extensive research on unconfined pool boiling for which the high heat transfer rate associated is widely attributed to evaporation of the microlayer of liquid near the three-phase contact line [30], [153]. However, a confinement wall also significantly alters the two-phase interface dynamics, as the bubble must grow within the confined space, and the rewetting of liquid on the boiling surface. Hence, the mechanistic explanation of the enhanced heat transfer rate in confined boiling should consider

and encompass the effect of confinement on the complete cycle of vapor bubble growth, departure from the gap, and surface rewetting.

Many experimental studies have provided insight into factors that affect confined boiling enhancement and cannot be attributed to the microlayer enhancements theory. Specifically, past works showed that the heat flux, fluid properties (viz., viscosity), surface coatings, and the geometrical shape of the confinement periphery impact confined boiling. Stutz *et al.* [154] reported that enhancement in heat transfer with confined boiling deteriorates at high heat flux. Even though the combined fluid properties would result in lowering the bubble departure diameter, Lallemand *et al.* [155] observed higher heat transfer coefficient for mixtures of water/ethylene glycol compared to pure water in confined configurations. It was concluded that the increase of fluid viscosity was advantageous for confined boiling at high heat flux. Additionally, Sarode *et al.* [105] experimentally observed that hydrophobic confining surfaces enhance the heat transfer coefficient compared hydrophilic surfaces. Souza *et al.* [132] evaluated nanocoated boiling surfaces for confined boiling. While the nanocoating reduced the heat transfer coefficient in the unconfined case due the reduction of nucleation sites, it is improved in the confined configuration. Furthermore, the enhancement was found to be sensitive to the geometrical divergence rate of the step from the confinement region to the unconfined fluid pool [131]. All of the above enhancements cannot be explained by the microlayer enhancement theory and indicate that the bubble interface dynamics play a critical role in enhancing heat transfer characteristics in confined boiling. Moreover, confined boiling often exhibits unique periodic spikes in the surface temperature as reported by Kapitz *et al.* [104]. In fact, unlike the relatively consistent bubble generation that occurs in unconfined boiling, in our past work [156], the highest heat transfer coefficient for confined boiling was observed within an intermittent boiling regime (a regime uniquely observed in confined boiling having periods of boiling interspersed with sensible heating that causes periodic spikes in the surface temperature). A deeper understanding of this distinct intermittent boiling regime is required to understand the enhancement mechanisms.

To elucidate the mechanisms that impact confined boiling, this study experimentally evaluates confined boiling across a range of gap spacings through quantification of the boiling curves and high-speed visualization of the bubble dynamics. We observe that small

residual regions of vapor left behind when vapor from a bubble escapes through the edges of the confined region, termed 'vapor stem bubbles', provide seeds for subsequent boiling without requiring nucleation of a new vapor bubble to continue the cycle of vapor growth and departure. We propose that these vapor stem bubbles, complementary with the micro-layer enhancement of the bubble growth process, are a primary mechanism of heat transfer enhancement in confined boiling, particularly in the intermittent boiling regime. In the following sections, we discuss the experimental setup used to investigate the heat transfer in confined boiling and report the influence of gap spacing on the mechanisms of vapor generation observed. Then, boiling curves for various confined geometries are evaluated to identify the dominant enhancement mechanism of confined boiling.

4.2 Experimental Methods

The confined boiling apparatus, illustrated in Figure 4.1, is designed to measure the surface heat flux and superheat for a fixed heated surface diameter, D , and controlled confinement gap spacing, S . A glass window with adjustable vertical positioning creates the confined boiling region above the heated surface. A high-speed camera is used to visualize the two-phase interface dynamics, in order to characterize the mechanisms of the enhancement in heat transfer during confined boiling. The confined boiling apparatus, described in detail below, is significantly modified from its original form used for unconfined boiling experiments, previously described by Hunter *et al.* [157].

The quartz glass double-wall vacuum-insulated chamber holds approximately 500 mL of deionized water (HACH-HQ 40d: $0.37 \mu\text{S cm}^{-1}$) within a 75 mm inner diameter. The vacuum insulation minimizes heat losses from the liquid pool. The 25.4 mm-diameter boiling surface is oriented horizontally at the bottom of the boiling chamber. Prior to collecting each boiling curve data set, the boiling surface is polished using 2000 grit emery paper to remove any oxidation. After polishing, the boiling surface has a contact angle of 86.8° . Throughout the experiments the liquid level was maintained about 100 mm above the boiling surface.

A cartridge heater (Watlow Firerod 1039; 12.7 mm diameter, 76.2 mm length; 1000 W) heats the 107.95 mm-long and 31.75 mm-diameter reference copper rod. Adjusting the sup-

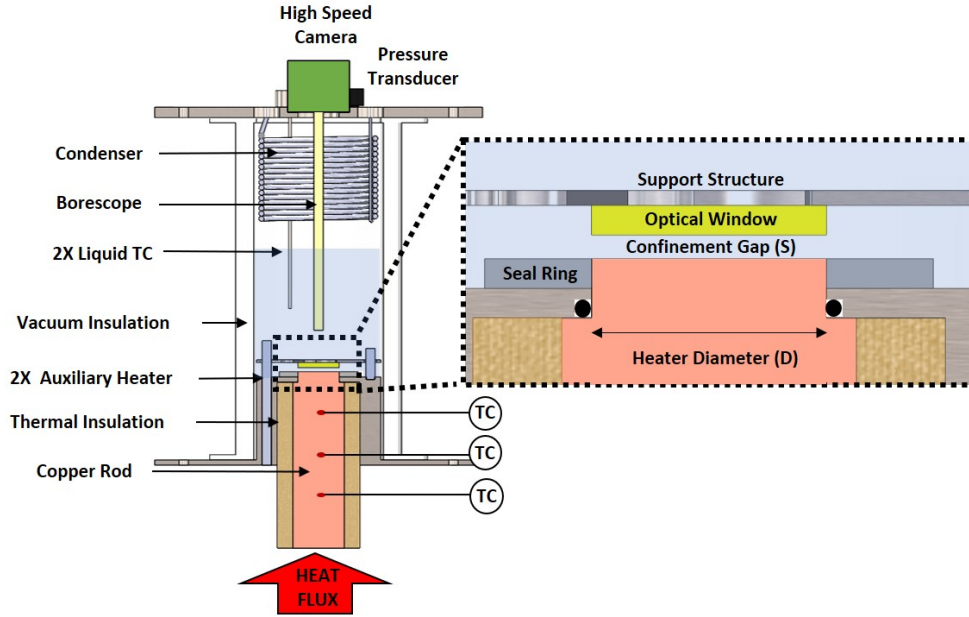


Figure 4.1. Cross-sectional schematic of the confined boiling experimental apparatus. An electrical heater supplies heat into a copper rod of known thermal conductivity. Three temperature measurements along the rod with embedded thermocouples quantify the heat flux and are extrapolated to estimate the boiling surface temperature. A glass window confines boiling to within the gap of controlled the vertical distance between the boiling surface and the confinement wall, S . A high-speed camera captures the two-phase interface dynamics through a rigid borescope during boiling. Two auxiliary heaters maintain the liquid pool at the saturation temperature. A pressure transducer measures the chamber internal pressure. The exterior of the boiling chamber and the copper rod are well insulated to minimize heat losses.

plied voltage controls the heat flux into boiling surface. The temperature gradient along the reference rod is measured by three embedded T-type thermocouples (Omega; ± 0.3 K). The thermocouples are spaced 6.35 mm apart along the centerline of the reference rod. One-dimensional heat flow is assumed such that the temperature gradient can be linearly correlated to the heat flux at steady state according to Fourier's law. A 18 mm-thick micro-porous insulation (MICROSIL) covers the perimeter of the reference rod to minimize heat losses. As the reference rod steps down from 31.75 mm diameter to the 25.4 mm diameter boiling surface, the temperature of the boiling surface is linearly extrapolated using a numerically-estimated thermal resistance of the step from the closest thermocouple temper-

ature (12.7 mm below the boiling surface) and the measured heat flux. Minimal spatial temperature inhomogeneities are expected on the boiling surface because of the relatively large copper reference block between the heat source and the boiling surface. The temperature measurements are logged at 1 Hz sampling rate via a data acquisition (DAQ) system (LabJack U6pro) through LabVIEW. The thermocouple cold junction compensation is done using a built-in temperature sensor within the DAQ.

A Viton O-ring seals the reference rod to the boiling chamber. The boiling apparatus body is electrically grounded to reduce measurement noise and prevent charge accumulation. In addition to the main heater, the apparatus is equipped with two additional submerged auxiliary cartridge heaters (Omega HDC19110; 3.2 mm diameter, 88.9 mm length) to maintain the fluid in the reservoir at saturation conditions. To purge non-condensable gases dissolved in the working fluid and trapped within the confinement space, the auxiliary heaters boil the working fluid vigorously for a minimum of 2 h prior to collecting boiling data on saturated water vapor conditions. Throughout the data collection period, the liquid in the reservoir is maintained within 0.3 °C of the saturation temperature by the auxiliary heaters. A condenser coil within the chamber maintains the pressure inside the boiling chamber at 101.8 kPa as monitored using an internal pressure transducer (ASHCROFT, G17MEK15F2VAC/30). An external DC power supply (HP E 3611A) excites the pressure transducer and a DAQ (NI 9219) logs the pressure measurements. A chiller (Thermo Fisher, ARCTIC A 25) circulates 95 °C cooling water through the stainless-steel condenser coil enclosed inside the boiling chamber to condense vapor back to liquid. Two T-type thermocouples (Omega; ± 0.3 K) monitor the liquid reservoir temperature.

To study confined boiling, a 6.35 mm-thick circular glass window is suspended above the boiling surface. The confinement window diameter matches the 25.4 mm diameter boiling surface. The confinement window has a static contact angle of 85.0 °. Three spring-loaded set screws level and adjust the confinement gap height, S , with a resolution of 2.2 $\mu\text{m}/^\circ$. Stainless steel reference shims are used to calibrate the confinement gap spacing. The copper boiling surface protrudes 5.5 mm above the chamber base. To prevent boiling off the sidewalls of this protrusion, a Teflon ring seals (Permatex 81160) and insulates the protruded side walls. The glass confinement window permits top-down optical viewing of the confined boiling region.

A high-speed camera (Photron FASTCAM 100K) captures the two-phase interface dynamics at 10,000 frames per second through a rigid borescope (Hawkeye Pro Hardy) submerged in the liquid reservoir. A plasma light source (THORLABS, HPL5345) illuminates the confined test section.

A boiling curve is obtained by measuring the steady state surface superheat as a function of the heat flux supplied to boiling surface. We define steady state as when the temperature measurements vary by less than 0.1 °C/min for 10 min. At steady state, the camera records flow visualization movies of the two-phase interface dynamics. After collecting steady state data at a given heat flux, the power is increased and the system is allowed to reach a new steady state. This process is repeated to obtain the entire boiling curve up to the critical heat flux. This CHF event is observed in the data as a very rapid surface temperature rise and the system is immediately shut down. The highest heat flux reported therefore corresponds to the last steady state data point prior to CHF.

To characterize the influence of confinement, boiling curves are acquired for multiple different confinement gap spacing in separate tests. The confinement gap spacing, S , is varied from 254 μm to 2286 μm . The Bond number, Bo , normalizes the confinement gap spacing by the capillary length, L_c , as:

$$Bo = \frac{S}{L_c} = \frac{S}{\sqrt{\frac{\sigma}{g(\rho_l - \rho_v)}}}, \quad (4.1)$$

where ρ_l and ρ_v are the density of liquid and vapor respectively, and g is the gravitational acceleration. Boiling is generally considered unconfined when the Bond number is much larger than unity, meaning the size of the vapor bubbles departing the boiling surface are much smaller than the confinement gap spacing. However, the confinement wall interacts with the vapor bubbles when the Bond number is near or below unity. The aforementioned confinement gap spacings are selected to focus on confined boiling behaviors and correspond to a Bond number range from 0.10 (at $S = 254 \mu\text{m}$) to 0.91 ($S=2286 \mu\text{m}$).

4.3 Results and Discussion

The confinement gap spacing determines the thermal and the dynamic behavior of confined boiling. This section reports and discuss the visual observations and thermal characteristics as the confinement gap spacing is varied. Two distinct characteristic behaviors are observed with respect to the gap spacing, namely: nucleation-suppressed confined boiling characterized by enhancement of the heat transfer coefficient through vapor stem bubbles; and nucleation-active confined boiling where nucleate boiling predominates by critical heat flux is reduced compared to unconfined conditions.

4.3.1 Confined Boiling Flow Visualization

Figures 4.2 and 4.3 show time series of images from the high-speed flow visualizations that illustrate the confinement gap spacing effect on the two-phase interface dynamics during boiling. A transition in boiling characteristics is observed around some spacing threshold, below which nucleation is suppressed (Figure 4.2). Vapor bubbles span the gap between the confinement wall and the boiling surface, restricting vapor bubble growth to a two-dimensional plane parallel to the boiling surface. Eventually, the trapped bubble grows and reaches the outer periphery of the confinement zone. The combination of buoyancy and surface tension forces facilitate the extraction of vapor from the confinement zone. Consequently, liquid is replenished from surrounding pool. However, the liquid rewetting rate varies spatially based on the viscous resistance between the two-phase interface and confinement outer periphery. The variable rewetting rate along the two-phase interface results in splitting of the confined vapor bubble as it exits the confinement gap, with only partial escape of the vapor. As illustrated in the supplemental video, no pinning of the interface is observed. This rewetting process leaves a residual vapor ‘stem’ bubble in the gap from which then next vapor generation cycle stems, and so the process continues in a repeating manner.

In contrast, active nucleation sites are observed for gap spacings larger than the threshold. Vapor is able to completely exhaust from the gap due to the lesser viscous resistance to rewetting, and stem bubbles are not formed. Rather, as shown in Figure 4.3, isolated

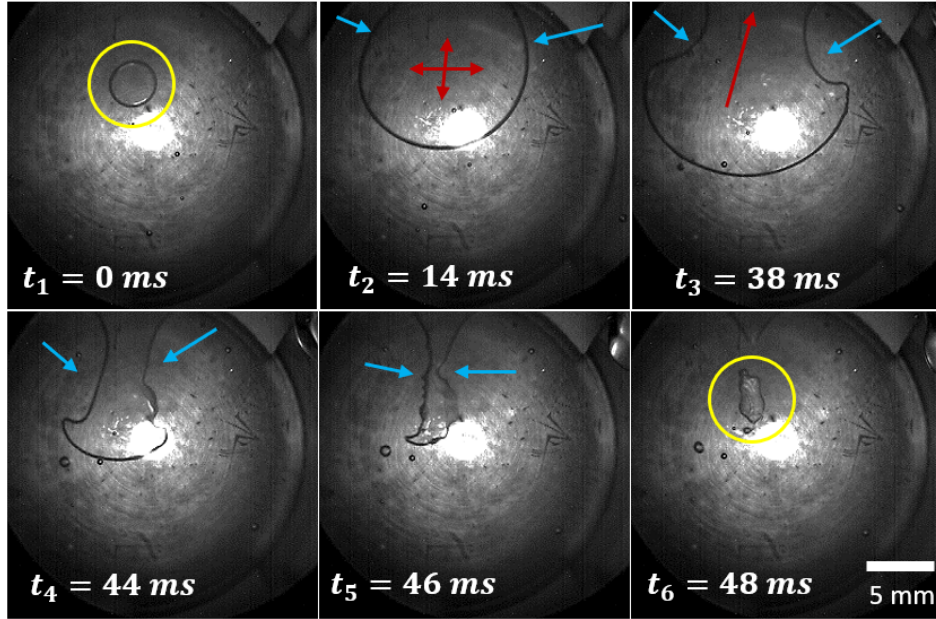


Figure 4.2. Top view of the boiling surface at several points in time for a nucleation-suppressed confined circular boiling surface ($Bo = 0.30$ with $q'' = 10 \text{ W/cm}^2$). As the vapor expands (red arrows in t_2) and then escapes (red arrow in t_3) confinement, liquid replaces the vapor volume within the confined region (blue arrows in t_4 and t_5). Within the extremely confined boiling region, rewetting occurs at different rates at different positions along the two-phase interface. Viscous resistance slows the rewetting of regions further from the confinement edge as shown at time steps t_4 and t_5 . As a result, most of the vapor bubble escapes the confined region, but partially leaves behind a stem vapor bubble in the confined space at in time step t_6 . This new vapor bubble stems from the vapor left from the preceding vapor bubble and the cycle repeats.

spherical vapor bubbles grow from active nucleation sites after vapor departs from the gap. Then, adjacent bubbles formed at different nucleation sites eventually coalesce into single bubbles having lower surface curvature. The change in bubble curvature, and the associated internal pressure forces across the two-phase interface, allowing for an abrupt increase in the growth rate of the coalesced vapor bubble. Due to the complete evacuation of vapor from the confinement gap, the vapor bubbles in following cycles also initiate from vapor embryos at nucleation sites on boiling surface. Note that for nucleation active confined boiling at higher powers, multiple bubbles often form throughout the surface and these cycles happen simultaneously and not necessarily synchronously.

4.3.2 Effect of Confinement Gap Spacing on Boiling Heat Transfer

Confined boiling curves are measured for five confinement gap spacings from 254 μm to 2286 μm . First, to validate the boiling facility measurements, four repeated unconfined pool boiling curves are measured without suspending the confinement glass above the boiling surface. The measured CHF values of these unconfined pool boiling tests were all within $\pm 6.6\%$ of average measurement ($q''_{CHF} = 96.8 \text{ W/cm}^2$). Additionally, the average CHF value is within 12.5% of the theoretical value for finite surfaces [72] of 110.7 W/cm^2 .

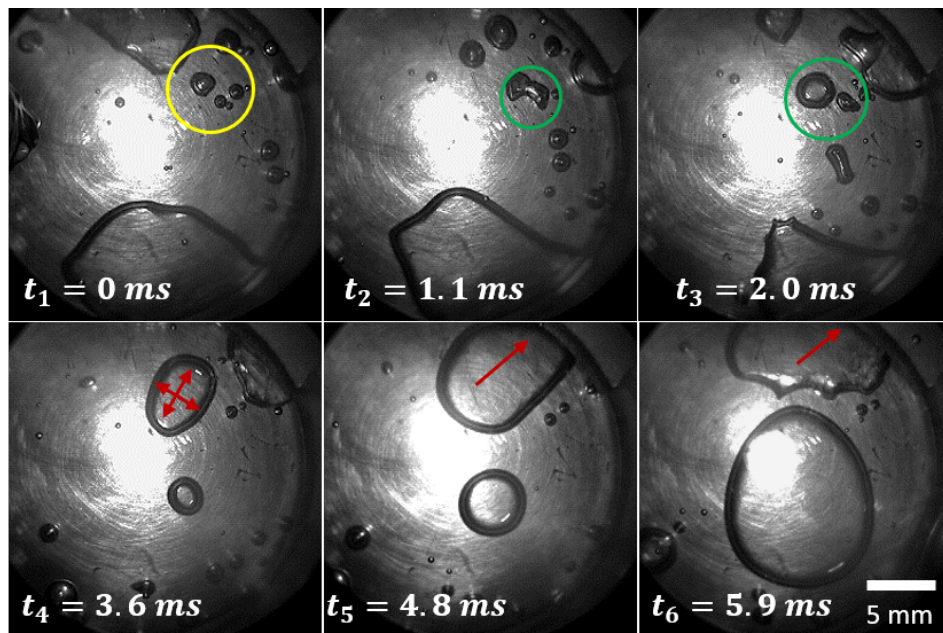


Figure 4.3. Top view of the boiling surface at several points in time for a nucleation-active confined circular boiling surface ($Bo = 0.63$, $q'' = 14 \text{ W/cm}^2$). Consecutive isolated bubbles forms from an active nucleation site as shown inside the yellow circle at time step t_1 . Then, adjacent bubbles formed at different nucleation sites eventually coalesce into single bubbles having lower surface curvature as demonstrated inside the green circles at time steps t_2 and t_3 . The change in bubble curvature, and the associated internal pressure forces across the two-phase interface, allow for an abrupt increase in the growth rate of the coalesced vapor bubble (red arrows in time step t_4). The vapor bubble escapes confinement completely when it reaches the confinement edge (red arrows in time steps t_5 and t_6).

Boiling curves for varying confinement gap spacing are obtained by measuring the steady state surface superheat as a function of the heat flux supplied to boiling surface. The confined boiling data are compared to the average of the unconfined pool boiling data by plotting the surface superheat (Figure 4.4) and heat transfer coefficient (Figure 4.5) as a function of the heat flux.

The transition in the two-phase dynamics characteristics with respect to gap spacing influences the boiling curves during confined boiling. For the case of nucleation-active confined boiling, the minimum incipience superheat criterion for nucleation site activation must be met to initiate and maintain boiling. While surface wettability affects nucleation onset, ultimately, the driving force, surface superheat, must overcome the interface surface tension for a given vapor embryo size for the bubble to grow. Minimum incipience criteria have been developed by Hsu [21], [26] where the vapor embryo is assumed to exist at the mouth of a cavity on the boiling surface and subjected to the bulk liquid temperature gradient as illustrated in Figure 4.6. Hereafter, the minimum incipient heat flux, q_i'' , for a given superheat required for incipience, $T_i - T_{sat}$, is expressed as follow:

$$q_i'' = \frac{k_l h_{lv}}{a^* 8 \sigma T_{sat} \nu_{lv}} (T_i - T_{sat})^2, \quad (4.2)$$

where k_l is the fluid thermal conductivity, h_{lv} is the latent heat of vaporization, σ is the surface tension, ν_{lv} is the difference of specific volume between phases, $T_i - T_{sat}$ is the difference between the minimum incipience surface temperature and saturation temperature, and a^* is a geometrical factor that relates the height of the vapor embryo to the radius of the vapor embryo. Note that we use $a^* = 1.6$ for unconfined boiling while $a^* = 1.0$ for confined boiling. A brief derivation of Equation 4.2 can be found in the appendix.

For unconfined boiling, during nucleate boiling, new vapor bubbles grow from the residual vapor embryo left behind the departed bubbles at the nucleation site in a cyclic manner, usually referred to as the ebullition cycle. The residual vapor bubble radii are larger than cavity mouth radius [26], and therefore, boiling can be maintained at active nucleation sites at superheats lower than the incipience criterion for the unconfined configuration. However, nucleation-active confined boiling improvement is limited by the minimum incipient boiling

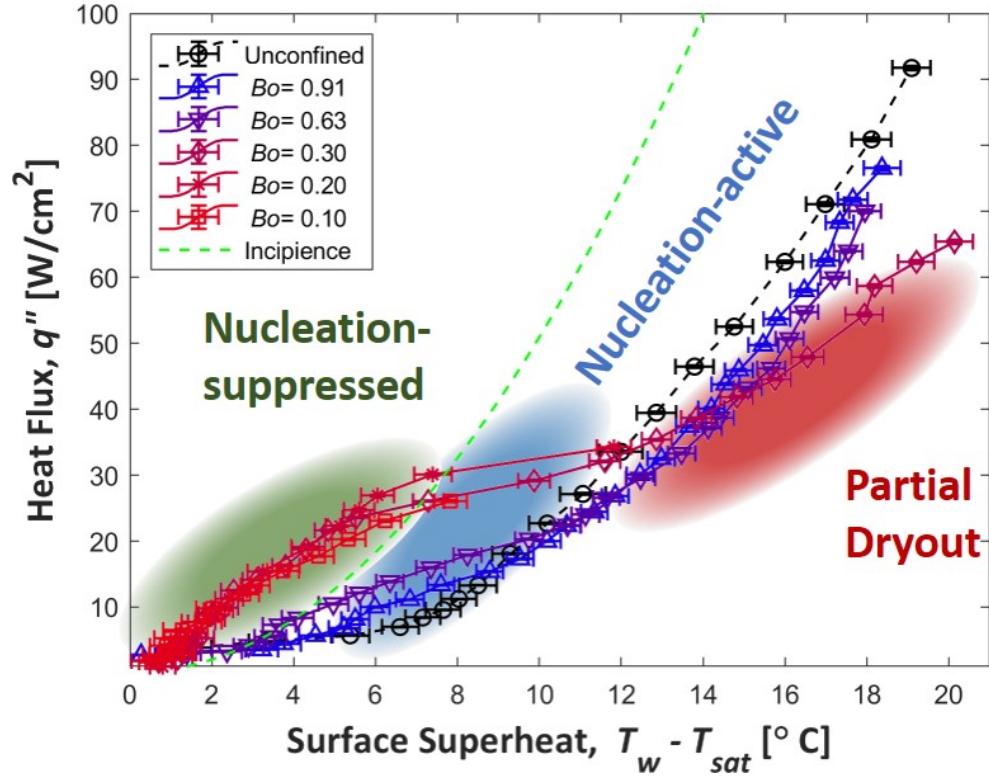


Figure 4.4. Boiling curves for different non-dimensional confinement gap size ($Bo = S/L_c$). The boiling process spans three distinct characteristics highlighted by different shaded regions. In the *partial dryout* (shaded in red), regions of the boiling surface remain continually covered with vapor due to restriction of liquid replenishing imposed by the confinement wall. As a result, boiling occurs at a higher surface superheat compared to a similar heat flux in the unconfined boiling curve. The blue shaded region is the *nucleation-active* confined boiling region. Nucleation-active confined boiling is limited by the minimum superheat for incipience as expressed in Equation 4.2 (green dashed line). Enhancements to the heat transfer coefficient are mainly attributed to the larger evaporative microlayer in confined boiling, where active nucleation sites are required to generate new vapor bubble, as demonstrated for nucleation-active confined boiling curves ($Bo = 0.9$ and 0.63). On the other hand, for nucleation-suppressed confined boiling ($Bo = 0.1, 0.2,$ and 0.3), vapor generates from the vapor stem bubbles left behind from a previous bubble growth and escape cycle in the *nucleation-suppressed* region (shaded in green). The relatively large radius of stem bubbles compared to vapor embryos allows vapor generation at superheat lower than the minimum superheat required for vapor embryos growth from the boiling surface.

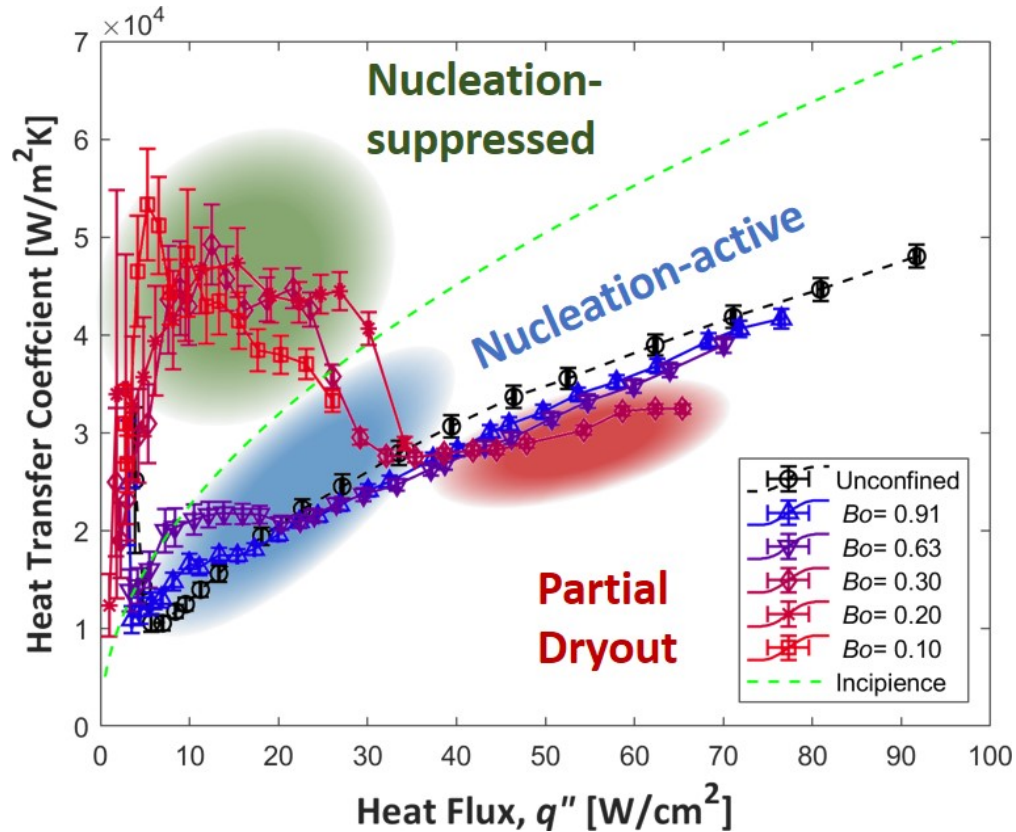


Figure 4.5. Heat transfer coefficient for different non-dimensional gap sizes ($Bo = S/L_c$) as a function of heat flux. For the unconfined boiling case, the heat transfer coefficient increases with heat flux due to the increase in the active nucleation site density reaching a maximum unconfined heat transfer coefficient at CHF. However, in nucleation-suppressed confined boiling ($Bo = 0.1, 0.2$ and 0.3), the maximum heat transfer coefficient is achieved at the low range of heat flux values due to the stem bubble boiling enhancement mechanism. Similar enhancements are not observed in nucleation-active confined boiling ($Bo = 0.63$ and 0.9), where the main heat transfer coefficient enhancement mechanism is the extension in the area of the evaporative microlayer which is limited to the minimum incipience superheat criterion (dashed green line).

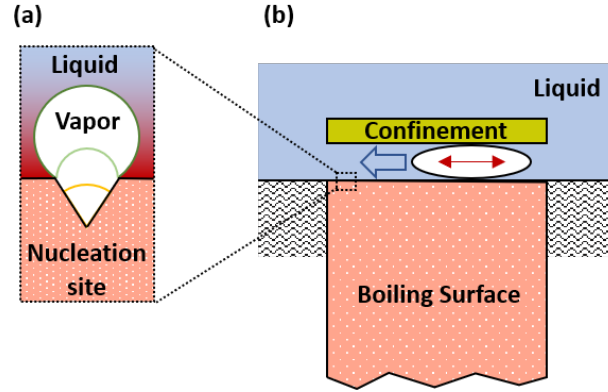


Figure 4.6. Schematic of (a) bubble growth at a nucleation site and (b) bubble growth within a confined boiling system. As the confined vapor bubble grows parallel to boiling surface (red arrow), the induced flow (blue arrow) agitates the protruded region of the vapor embryos and reduces its radius to the local surface roughness on the boiling surface. As a result, nucleation sites within the confined boiling space are hydrodynamically deactivated and the minimum superheat for nucleation onset is required to maintain boiling within the confined space. Note the color gradient in the left panel illustrates the temperature gradient from the surface temperature (red) to the saturation temperature (blue).

criteria expressed in Equation 4.2 (nucleate boiling is highlighted in the blue shaded region). In the nucleation-active confined boiling curves ($Bo = 0.63$ and 0.91), at low heat fluxes, the vapor bubbles expand parallel to the boiling surface. This increases the microlayer area underneath the vapor bubble which enhances heat transfer rate at a given surface superheat relative to the unconfined boiling curves. We attribute the microlayer enhancement constraint in nucleation-active confined boiling to hydrodynamic deactivation of nucleation sites. As the confined vapor bubbles grow parallel to boiling surface, the induced flow agitates the protruded region of the residual vapor bubble and reduces its radius to the surface cavity mouth radius as illustrated in Figure 4.6. As a result, the minimum criteria for incipient boiling is required to maintain nucleation-active confined boiling.

In contrast, in the nucleation-suppressed confined boiling (green-shaded region), vapor stem bubbles are available to sustain phase change without requiring activation or growth of vapor embryo at nucleation sites (as in the nucleation-active confined boiling). Nevertheless, an active nucleation site is needed only to initiate the phase change process in the

nucleation-suppressed region resulting in initial temperature overshoot. However, after boiling initiation, an active nucleation site is no longer needed and stem bubbles facilitate thermal enhancements beyond the minimum incipience boiling criterion in nucleation-suppressed confined boiling cases ($Bo = 0.10, 0.20, \text{ and } 0.30$). On the other hand, once the minimum incipience boiling criterion is met at the higher range of heat flux (Equation 4.2), simultaneous occurrence of both vapor stem bubbles and nucleate boiling are visually observed as illustrated in the supplemental video. Bubbles nucleate while the liquid rewets the boiling surface, limiting the radial inward penetration of the liquid in the confined gap. As a result, the nucleation-suppressed confined boiling curves abruptly shifts into a partial dryout boiling region where regions of boiling surface remain continually covered in vapor due to the restriction of liquid replenishing imposed by the confinement wall. Consequently, the average boiling surface superheat exceeds the equivalent superheat of an unconfined boiling in a similar heat flux value (red shaded region). This notable shift in surface superheat indicates *that stem bubble boiling is the dominant heat transfer enhancement mechanism leading to an increased heat transfer coefficient in nucleation-suppressed confined boiling configurations.*

4.3.3 Vapor Stem Bubbles

Figure 4.7 schematically illustrates the proposed mechanism by which vapor stem bubbles enhance heat transfer in confined boiling configurations. The significant viscous resistance varies the rewetting rate along the two-phase interface in nucleation-suppressed confined boiling which results in splitting of the confined vapor bubble as it exits the confinement gap, with only partial escape of the vapor. The size of residual vapor stem bubble is on the same scale as the confinement gap spacing. Due to the difference in two-phase interface radius, surface tension forces on vapor stem bubbles are weaker compared to vapor embryos in nucleation site. Hence, the vapor stem bubble can begin to grow at surface superheat lower than incipience minimum criterion and without requiring activation of additional nucleation sites on the boiling surface, thereby lowering the overall thermal resistance in nucleation-suppressed confined boiling.

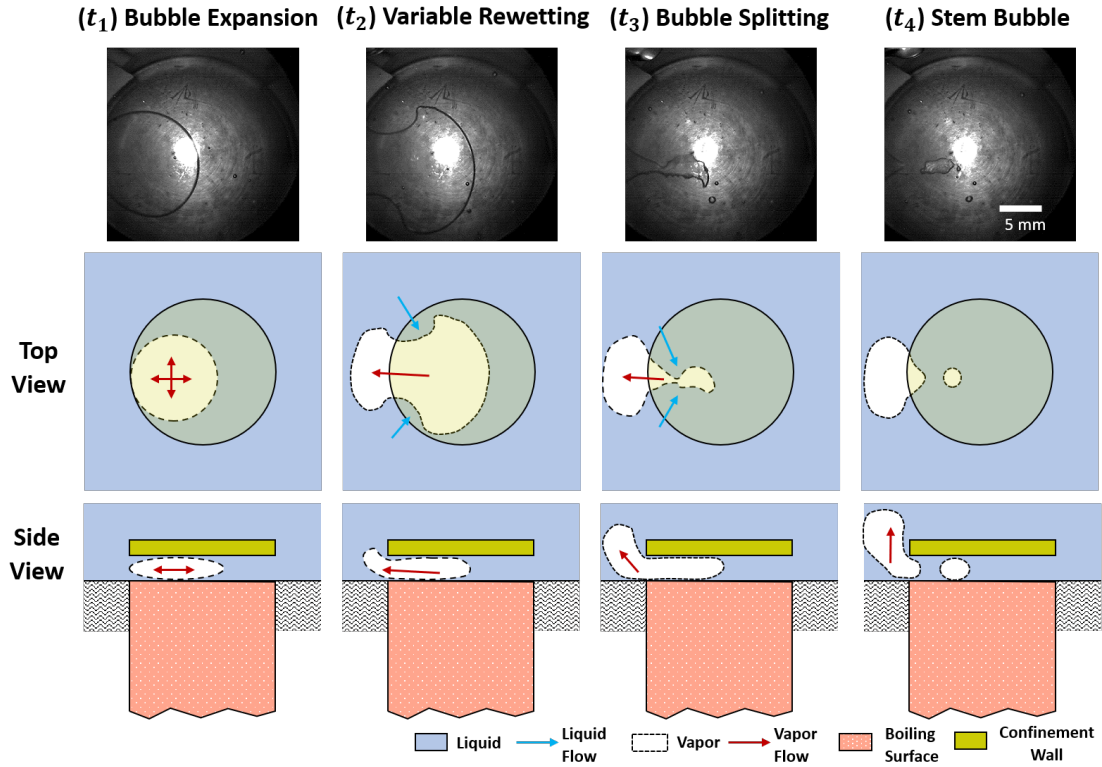


Figure 4.7. Flow visualizations and complementary schematics of the cycle of bubble growth and escape in nucleation-suppressed confined boiling. The time series demonstrates a life cycle of vapor bubble growing between the boiling surface and the confinement wall. In the first image t_1 , confinement limits the bubble to growing only parallel to the boiling surface. After the bubble reaches the edge of the confined zone, it can escape into the liquid pool. Liquid replaces the escaped vapor bubble at variable wetting rates across the two-phase interface, t_2 . The red arrows illustrate the vapor outflow of the confinement and the blue arrows illustrate the liquid inflow. Viscous resistance slows the rewetting for regions furthest from confinement edge which results in vapor splitting and partial vapor escape as illustrated in t_3 . Thus, stem vapor bubbles form from the residual trapped vapor within the confined space, t_4 . Because no active nucleation sites are required for stem bubble boiling, phase change occurs at reduced superheat compared to nucleate based boiling. This cycle then repeats.

The concept of vapor stem bubbles can potentially explain some of the previous confined boiling experimental observations that cannot be explained by the microlayer theory enhancement alone, as reviewed in the introduction. In boiling regimes with these vapor stem bubbles, interface dynamics and fluid viscosity control the formation of the residual stem bubble. Further, the chaotic nature of boiling has a stochastic effect on forming the residual stem bubble within the confined space. In other words, even for a steady constant operating condition, there is a probability of complete vapor bubble escape for which a stem vapor bubble is not left behind for the next bubble generation cycle. In this case, active nucleation sites are required to reinitiate phase change on boiling surface. Since, these nucleation-site vapor embryos have smaller radius than the vapor stem bubble, the heat will momentarily be dissipated through the sensible heating of local fluid until the minimum superheat required for nucleation site activation is reached. As a result, the high heat transfer coefficient caused by the phase change is briefly not observed. This momentary pause of phase change would result in the distinct intermittent boiling regimes uniquely observed in confined boiling configurations [156].

Vapor stem bubbles are formed during confined boiling only when confinement gap is smaller than a spacing threshold. In order to harness the enhanced thermal performance of this boiling behavior in applications, it is crucial to generally predict the gap spacing threshold below which these stem bubbles form (*i.e.*, the transition from nucleation-suppressed to nucleation-active confined boiling). The formation of isolated spherical nucleated vapor bubbles is one of the distinct characteristics of nucleation-active confined boiling. On the other hand, significant viscous resistance induces the formation of the stem bubbles in nucleation-suppressed confined boiling. Therefore, one would expect that the confinement gap threshold is closely related to the vapor bubble growth dynamics near the heated surface. In general, the bubble growth process at any instant of time is affected by the interaction of the pressure difference across the two-phase interface and the fluid momentum, as well as by the rate of heat transfer across the two-phase interface. The contribution of each of these factors varies throughout the life cycle of the vapor bubble. Inertia-controlled growth dominates the hemispherical growth at early stages of bubble growth. During inertia-controlled growth, heat transfer to the interface is not the limiting factor, but rather the growth is limited by

the momentum interaction between the bubble and the surrounding liquid. Once the vapor internal pressure equilibrates with surrounding liquid pressure, the bubble transforms into spherical shape and its growth rate is limited by relatively slower heat transfer rate across the two-phase interface [21], referred to as thermal-controlled growth. Hence, thermal-controlled growth exhibits lower viscous resistance compared to the inertia growth due to the difference in growth rate.

We propose that the rate of the vapor bubble growth directly correlates to the transition between nucleation-suppressed and nucleation-active confined boiling. We attribute the formation of stem bubbles to the variable liquid rewetting rate along the two-phase interface due to the significant viscous resistance. Because the viscous resistance of liquid flow is proportional to velocity, viscous resistance is expected to split the trapped bubble when the interface velocity is relatively high. The faster inertia-controlled bubble growth leads to higher viscous resistance compared to the thermal-controlled bubble growth. In addition, the trapped bubble could reach the confinement edge before equilibrating its internal vapor pressure to surrounding liquid pressure during the inertia-controlled growth. Furthermore, consequent stem bubbles would have radii of curvature smaller than the transition radius between inertia- controlled and thermal-controlled bubble growth, and hence, it would have high internal pressure which helps increasing the bubble ejection velocity from the confinement region. As a result, liquid replaces the escaped bubble volume at equally high velocity resulting in the formation of stem bubbles. In other words, vapor stem bubble enhancement mechanism is significant when the confinement gap is smaller than the transition radius from inertia-controlled to thermal-controlled growth. Van Stralen *et al.* [158] proposed that the temporal-dependence of the radius of the vapor bubble, $R(t)$, can be modelled as a superposition of the radii in the inertial-controlled, R_1 , and the thermal controlled, R_2 , regimes as:

$$R(t) = \frac{R_1(t)R_2(t)}{R_1(t) + R_2(t)}, \quad (4.3)$$

where R_1 and R_2 are defined as:

$$R_1 = 0.8165 \left(\frac{\rho_v h_{lv} (T_w - T_{sat}) \exp\left(-\left(\frac{t}{t_d}\right)^{1/2}\right)}{\rho_l T_{sat}} \right) t, \quad (4.4)$$

$$R_2 = \left[1.9544 \left(b^* \exp\left(-\left(\frac{t}{t_d}\right)^{1/2}\right) \right) + 0.3730 Pr_l^{-1/6} \left(\exp\left(-\left(\frac{t}{t_d}\right)^{1/2}\right) \right) \right] Ja (\alpha_l t)^{1/2}, \quad (4.5)$$

where ρ_l , α_l , and Pr_l are the density, thermal diffusivity, and Prandtl number of the liquid, h_{lv} is the latent heat of vaporization, $(T_w - T_{sat})$ is the superheat of the boiling surface, t is time, Ja is Jakob number, and t_d is the bubble departure time, which is obtained based on the departure diameter, d_d , using the following equations [17], [159]:

$$d_d = \sqrt{\frac{0.04^2 Ja^2 \sigma}{g(\rho_l - \rho_v)}}, \quad (4.6)$$

and

$$t_d = \frac{d_d}{0.59 \left(\frac{\sigma(\rho_l - \rho_v)}{\rho_l^2} \right)^{1/4}}. \quad (4.7)$$

b^* is a geometrical correction factor to account for the fact that only portion of the hemispherical bubble near the heated surface is in contact with the superheated liquid. This parameter is defined as [158]:

$$b^* = 1.3908 \frac{R_2(t_d)}{Ja \sqrt{\alpha t}} - 0.1908 Pr_l^{-1/6}. \quad (4.8)$$

Figure 4.8 (a) the ratio of the heat transfer coefficient between confined and unconfined boiling ($h_{con}(q'')/h_{\infty}(q'')$) as a function of the heat flux for various gaps spacings. Figure 4.8 (a) illustrates the thermal enhancement magnitudes for various confined boiling spacings compared to similar heat flux levels in an unconfined configuration. Confinement enhances heat transfer at the lower range of heat fluxes tested while degrading heat transfer at the higher range of heat fluxes. Figure 8 (b) shows the temporal evolution of the non-dimensionalized di-

iameter of the vapor bubble ($\Gamma = d/L$) using the above bubble growth model (Equations 4.3) for the range of superheats required for onset of nucleate boiling as observed during unconfined boiling testing ($T_i - T_{sat} \sim 4\text{-}5$ °C). The criteria for onset of nucleation depend on the working fluid wettability and the surface morphology. Since the same boiling surface and working fluid are used in the unconfined tests, the nucleation onset superheat in unconfined boiling is used. During inertia-controlled growth, the bubble grows relatively fast and in a hemispherical shape. As the bubble growth transitions to the thermal-controlled growth, the bubble transforms into a spherical shape. In this study the transition between the two regimes is identified when the bubble growth rate decays by 90% of initial value. From Figure 8(b) we see this transition diameters, Γ , occur in the range of $\sim 0.35 - 0.5$. Comparing to Figure 8(a), there is a noteworthy increase in the heat transfer enhancement when the confinement gap spacing, Bo , becomes smaller than this bubble transition diameters, Γ (note that both of these parameters are normalized by the same capillary length scale, so they can be directly compared in magnitude). This indicates that the transition in heat transfer enhancement mechanism from stem bubble boiling (nucleation-suppressed confined boiling) to microlayer based enhancement (nucleation-active confined boiling) occurs when the gap spacing is sufficiently small to obstruct the initial hemispherical vapor growth normal to the boiling surface.

4.4 Summary

In summary, we measure heat transfer characteristics and observe the interface dynamics for confined boiling of water occurring in confinement gap spacings from $Bo = 0.10$ to 0.91 . In agreement with earlier work on confined boiling, confinement enhances the heat transfer rate compared to unconfined boiling. However, previous work purported that the primary mechanism of enhancement was increased evaporation from a microlayer underneath the distorted vapor bubble, which cannot explain all past observations of enhancement in the past literature. Our work shows that the microlayer is indeed attributable for enhancement in heat transfer, but only for nucleation-active confined boiling ($0.5 \leq Bo \leq 1.0$). On the other hand, for nucleation-suppressed confined boiling ($Bo \leq 0.35 - 0.5$), newly observed vapor stem

bubbles offer the dominant mechanism to enhance heat transfer. In this extremely confined regime, non-uniform surface rewetting results in only partial evacuation of the vapor exiting from the confinement gap. Thus, stem vapor bubbles form from the residual trapped vapor within the confined space. Because no active nucleation sites are required for stem bubble boiling, phase change occurs at reduced superheat compared to nucleate based boiling. This newly reported enhancement mechanism was observed both visually via a high-speed camera and is supported by the measured thermal response. Based on this improved understanding, three distinct confined boiling characteristics are identified (namely: nucleation-suppressed confined boiling, nucleation-active confined boiling, and partial dryout). Additionally, a threshold for the confinement gap spacing has been identified to predict the occurrence of stem bubble boiling. This improved understanding of the enhancement in heat transfer in

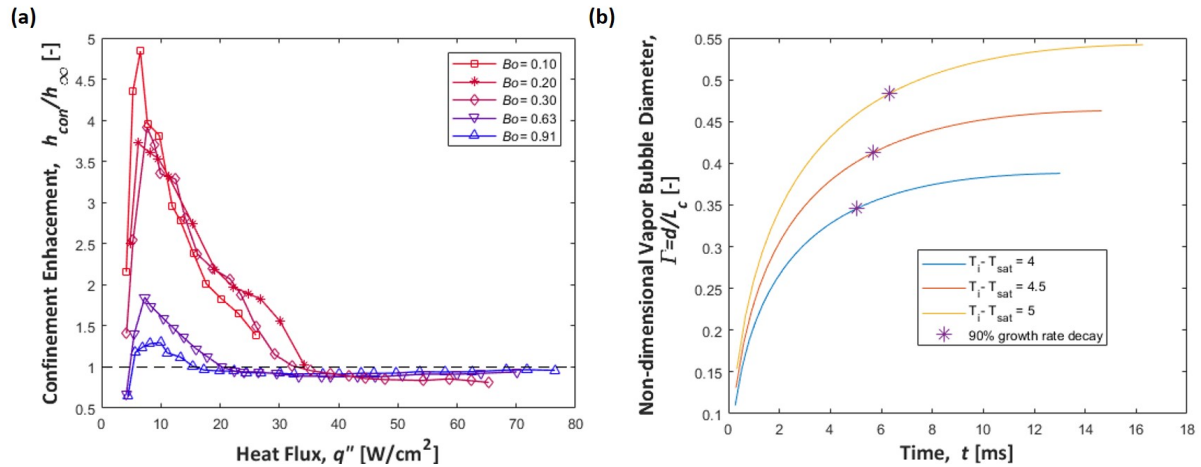


Figure 4.8. (a) Confinement enhancement ratio in the heat transfer coefficient compared to unconfined boiling ($h_{con}(q'')/h_{\infty}(q'')$) as a function of heat flux illustrating the impact of the gap size on the transition between nucleation-active to nucleation-suppressed confined boiling. (b) Temporal evolution of the non-dimensional vapor bubble diameter (d/L_c) predicted from Equations 4.3-4.8 for the range of heat fluxes required for the onset of nucleate boiling observed experimentally ($T_i - T_{sat} \sim 4-5$ °C). The transition between inertia controlled and thermal controlled growth regimes occurs when the growth rate decays by 90% of initial value. Enhancements in heat transfer due to the vapor stem bubbles are significant when the confinement gap is smaller than the transition between the two bubble growth regimes.

extremely confined boiling has an important impact on designing compact two-phase thermal management solutions.

4.A Nucleation Onset Model

The incipience model used in Equation 4.2 is based on Hsu [26]. Starting from a mechanical force balance across the two-phase interface:

$$P_v = P_l + \frac{2\sigma}{r}, \quad (4.9)$$

where σ is the surface tension. Combining with the Clausius Clapyron equation,

$$\frac{\partial P}{\partial T} = \frac{T v_{fg}}{h_{fg}}, \quad (4.10)$$

and the conduction based temperature drop for the liquid near the boiling surface results in the following expression:

$$T_l = T_{sat} + \frac{T_{sat} v_{vf}}{h_{fg}} = T_w - \frac{q'' a^* r}{k_l}, \quad (4.11)$$

where a^* is a geometrical factor that relates the height to the radius of the vapor embryo. In the confined configuration, a^* equals to 1 due to hydrodynamic deactivation. For the unconfined configuration, a^* equals to 1.6 [30] due to the ebullition cycle. Rearranging terms yields the following expression that can be solved for the active vapor embryo size:

$$\frac{q'' a^* r^2}{k_l} - (T_w - T_{sat})r + \frac{T_{sat} v_{fg} 2\sigma}{h_{fg}} = 0. \quad (4.12)$$

Specifically, the range of active vapor embryos sizes is given by

$$\begin{cases} r_{max} \\ r_{min} \end{cases} = \frac{(T_w - T_{sat}) \left\{ \begin{matrix} + \\ - \end{matrix} \right\} \sqrt{(T_w - T_{sat})^2 - \frac{8q'' \sigma T_{sat} v_{vg}}{k_l h_{fg}}}}{2a^* \frac{q''}{k_l}}. \quad (4.13)$$

The onset condition corresponds to $r_{tan} = r_1 = r_2$, such that

$$r_{tan} = \frac{(T_w - T_{sat})}{2a^* \frac{q''}{k_l}}. \quad (4.14)$$

Plugging Equation 4.14 into Equation 4.12 yields the criteria for the heat flux at the onset of nucleate boiling:

$$q''_{onset} = \frac{h_{fg}k_i(T_w - T_{sat})^2}{8a^*\sigma T_{sa}T v_{fg}}. \quad (4.15)$$

5. CRITICAL HEAT FLUX (CHF) IN CONFINED GAPS

Boiling enables high rates of heat transfer from a surface made possible at a relatively low thermal resistance motivating the use of two-phase cooling for increasingly compact thermal management solutions. However, extreme geometrical confinement of the liquid above the boiling surfaces is known to have detrimental effects on maximum heat transfer rate by inducing premature onset of film boiling. Moreover, previously developed critical heat flux (CHF) models for confined geometries focused on triggering mechanisms associated with unconfined pool boiling and, thus, are not generalizable. This work proposes a new mechanistic model for predicting CHF during boiling within a narrow gap, specifically developed to account for confinement effects on the triggering mechanism. The model postulates that occurrence of CHF coincides with the irreversible growth of a dry spot on the boiling surface. Three competing forces govern the two-phase interface dynamics, namely vapor recoil, surface tension, and hydrostatic forces. Dryout is triggered when the vapor recoil force due to vaporization at the two-phase interface balances the combined surface tension and hydrostatic forces leading to irreversible growth of the dry spot. The present work offers a predictive confined CHF model that accounts for confined boiling surface shape, size, orientation, confinement gap spacing, and working fluid properties, with a single fluid-specific fitting coefficient that represents the ratio of vapor area to the confinement opening area near CHF conditions. Notably, the developed CHF model is also effective in predicting the threshold gap below which confinement reduces pool boiling CHF. The model is compared to 197 experimentally measured confined CHF data points available from 10 studies in the literature that represent 7 different working fluids and a range of boiling surface inclinations and shapes. The model predicts the confinement-reduced CHF values with a mean error of 2% and standard deviation of 21%, which is less than half of the error compared to all other available predictive models. This clarification of the triggering mechanism and improved prediction accuracy of CHF, as offered by the current study, will enable broader practical system implementation of compact two-phase cooling technologies.

5.1 Introduction

The use of the latent heat of vaporization during boiling facilitates the removal of high heat densities while maintaining the boiling surface below operational temperature limits. Therefore, boiling is used in various energy conversion and heat exchanging applications [160]. To meet demands for compact and lightweight thermal management devices, increasing the surface-to-volume ratio of two-phase heat exchangers is advantageous in various industrial and scientific applications [161]. There is also growing interest in developing miniature cooling technologies that use passive boiling principles in confined geometries such as thermosyphons [162], pulsating heat pipes [163], immersion cooling, [129], and two-phase heat spreaders [164].

The ubiquity of pool boiling in many industrial and thermal management applications has motivated researchers for decades to understand and characterize the associated transport processes and limits [21]. One of the most important boiling characteristics for two-phase thermal management systems is the critical heat flux (CHF), which represents the maximum heat flux at which nucleate boiling can be sustained; above this limit, a system under constant heat flux condition will transition to film boiling [160]. Operating the system above CHF (*i.e.*, in the film boiling regime) results in a drastic increase in the thermal transport resistance due to the formation of a stable vapor blanket that can lead to a catastrophic temperature rise. Restricting boiling to occur in a narrow gap above the boiling surface, termed ‘confined boiling’ hereinafter, significantly alters the thermofluidic characteristics of pool boiling [8]. Primarily, vapor bubbles are forced to grow parallel to the boiling surface, extending the vapor coverage area associated with each nucleation site, whereas many of the models developed for pool boiling focus on vapor flow normal to the boiling surface. Therefore, the applicability of existing predictive macroscale CHF models needs to be carefully examined to account for these effects of confinement.

This work develops a model to predict CHF that accounts for the mechanistic influence of small gap spacing above the boiling surface, heater size, shape, and orientation on pool boiling. First, a review of the existing confined CHF models is presented. Then, we propose a new model for the CHF during boiling in a confined gap based on the micro-hydrodynamics

along the triple contact line on the boiling surface. The accuracy and generality of the developed CHF model, in comparison to previous models, is evaluated against an experimental dataset collected from the literature. Notably, the developed CHF model is also effective in predicting the threshold gap below which confinement reduces pool boiling CHF.

5.2 State-of-the-Art Models for CHF in Confined Geometries

The phenomenon of CHF has been experimentally reported since the late 19th century. In 1888, Lang [165] experimentally observed that the boiler efficiency in generating steam drastically decreases when the boiling surface superheat reaches a certain limit. Many researchers have since observed the CHF phenomenon and provided further insights into this behavior. However, boiling is a chaotic and a complex two-phase flow phenomenon owing to the dynamic evolution of multiple interfaces covering a wide range of length scales extending from the macroscale down to the molecular level [166]. Therefore, dimensionless groups and empirical constants are often employed in developing correlations useful for engineering applications. Bonilla and Perry [91] proposed one of the earliest correlations for CHF purely from experimental data. While empirical correlations lack generality and are only applicable in the range of conditions tested, incorporating mechanistic aspects of boiling into such empirical correlations can broaden their range of applicability. This section discusses theoretical frameworks that have been developed as a basis for a wide range of available models to predict CHF; the specific focus of this brief review is on pool boiling in confined configurations, that is, when the growth of vapor bubbles normal to the boiling surface is interfered with another solid surface before complete detachment of the bubble from the boiling surface, such as due to a parallel plate that forms a narrow gap above the boiling surface.

Geometrical confinement above the boiling surface and/or boiling from heaters of small sizes compared to the bubble dimensions significantly alters the thermofluidic characteristics of pool boiling compared to large surfaces. While there is not yet an agreed upon criterion for the dimension threshold for boiling a liquid in a confined gap above a heated surface, many works compare the gap spacing (or height), S , or the characteristic length of the

heater, such as diameter, D , or length, L , to the capillary length of the working fluid, L_c , to define a cutoff where the dimensions alter the pool boiling characteristics. For decades, it has been experimentally observed that confinement reduces the critical heat flux [98], [99], [101]–[104]. Significant progress has been made in understanding the underlying mechanism of flow boiling in microchannels where the working fluid is actively pumped through the confined gaps [167], [168]. However, less is understood about the mechanism of CHF during pool boiling in confined geometries, where the vapor bubbles must depart the surface by buoyancy [8]. Although many experimental studies have characterized the effect of geometrical confinement on pool boiling, a predictive correlation for CHF that can be applied to wide range of heater sizes, orientations, gap spacings, and working fluids has not yet been developed [8].

A common approach taken to predict the CHF for confined boiling is to modify models originally developed for unconfined pool boiling with factors that account for the effect of confinement. The seminal work of Zuber [71] formulated one of the most widely adopted theoretical frameworks for predicting the CHF for unconfined pool boiling from large flat surfaces. This hydrodynamic theory postulates that vapor generated at the boiling surface forms a periodic array of vapor jets, and that the CHF occurs when the liquid-vapor interfaces of these jets become unstable and block liquid supply back to the boiling surface. Using the critical Helmholtz velocity [70] as the instability criteria, Zuber [71] proposed the following relation for CHF, $q''_{\text{CHF},Z}$:

$$\frac{q''_{\text{CHF},Z}}{\rho_v^{0.5} h_{\text{lv}} [\sigma g (\rho_l - \rho_v)]^{1/4}} = K, \quad (5.1)$$

where K is constant, hereafter referred to as the dimensionless CHF ratio. The original work [71] proposed $K = \frac{\pi}{24}$, for finite surface. Later, Lienhard and Dhir [72] refined the model to show that a value of $K = \frac{\pi}{16(3)^{1/4}}$ was more accurate for flat boiling surfaces much larger than the Helmholtz unstable wavelength.

Despite being perhaps the most common model developed to date, the generalizability of Zuber’s CHF prediction has been criticized [69], [72], [73], [166] because it does not account for pressure, surface conditions, viscosity, and wettability despite experimental data suggest-

Table 5.1. A summary of the dimensionless CHF ratios modified to account for additional factors, $K = \frac{q''_{\text{CHF,Z}}}{\rho_v^{0.5} h_{lv} [\sigma g(\rho_l - \rho_v)]^{1/4}}$.

Dimensionless CHF Ratio	Wettability	Pressure	Viscosity	Orientation	Confinement	Reference
$K = \pi/24$						[71]
$K = \frac{\pi}{16(3)^{1/4}}$						[72]
$K = 0.171 \frac{(1+0.324 \times 10^{-3} \beta^2)^{1/4}}{(0.018 \beta)^{1/2}}$	✓					[74]
$K = 0.0336(\pi - \beta)^3 R_a^{0.125}$	✓					[75]
$K = 0.811 \left(\frac{1+\cos \beta}{16} \right) \left[\frac{2}{\pi} + \frac{\pi}{4}(1 + \cos \beta) + \frac{351.2 \cos \beta}{1+\cos \beta} \left(\frac{R_a}{S_m} \right) \right]^{1/2}$	✓					[76]
$K = [0.18 - 0.14(P/P_c)^{5.68}]$		✓				[77]
$K = 0.13 + 4 \left[\frac{\rho_l \sigma^{3/2}}{\mu_l^2 [g(\rho_l - \rho_g)]^{1/2}} \right]^{-2/5}$			✓			[78]
$K = 0.131 \left[-0.73 + \frac{1.73}{1+10^{-0.021(185.4-\theta)}} \right] \times \left[1 + \frac{55-\beta}{100} (0.56 - 0.0013\theta) \right]$	✓			✓		[79]
$K = [(0.229 - 4.27 \times 10^{-4} \theta)^{-6} + (0.577 - 2.98 \times 10^{-3} \theta)^{-6}]^{-1/6}$				✓		[80]
$K = 0.131(1 - 0.001117\theta + 7.79401 \times 10^{-6} \theta^2 - 1.37678 \times 10^{-7} \theta^3)$				✓		[81]
$K = \frac{0.134}{1+6.39 \times 10^{-5} (\rho_l/\rho_v)^{1.343} P_r^{0.252} (L/S)^{1.517}}$					✓	[111]
$K = \frac{0.18}{1+0.00918 (\rho_v/\rho_l)^{0.14} [g \frac{(\rho_l - \rho_v) D^2}{\sigma}]^{0.5} (D/S)}$					✓	[112]
$K = \frac{0.17}{1+6.8 \times 10^{-4} (\rho_l/\rho_v)^{0.62} (D_{eq}/S)}$					✓	[113]
$K = 0.131(0.6028 S^{0.3694})$					✓	[114]
$K = 0.185 \left(\frac{1}{1+71.43 e^{-1.32 S}} \right)$					✓	[101]
$K = \frac{0.16}{1+6.7 \times 10^{-4} (\rho_l/\rho_v)^{0.6} (L/S)}$					✓	[115]

ing that all of these factors have a strong influence on the CHF. Nevertheless, owing to the success of the underlying hydrodynamic instability theory in predicting CHF in pool boiling, subsequent investigations [74]–[81] attempting to resolve these effects on CHF typically adapted Zuber’s framework by including additional empirical factors in the dimensionless CHF ratio, K . The first portion of Table 5.1 summarizes those modifications for unconfined configurations.

Similarly, this hydrodynamic instability theory has been commonly reused as a framework for CHF predictions that accounts for the confinement effect [101], [111]–[115]. The second portion of Table 5.1 summarizes empirical correlations have been developed for the dimensionless CHF ratio, K , as a function of the confinement gap spacing, S , channel length, L , and heater diameter, D . However, it is crucial to revisit the underlying assumptions taken in developing these CHF models based on the hydrodynamic instability theory to reassess their generalized applicability for confined boiling configurations.

The hydrodynamic instability framework idealizes the vapor flow morphology as being large vapor columns normal to the boiling surface. Further, these vapor columns are assumed to arrange in a rectangular array on the boiling surface, as depicted in Figure 5.1-a, where the array spacing is equal to the dominant unstable Taylor wavelength, $\lambda_H = 2\pi(3\sigma/[(\rho_l - \rho_v)g])^{1/2}$. Vapor column diameters were further assumed be half of the vapor column spacing. The CHF occurs when the average vapor velocity, u_v is equal to the critical Helmholtz velocity, u_c :

$$u_c = \left[\frac{2\pi\sigma}{\rho_v\lambda_H} \right]^{1/2}. \quad (5.2)$$

Using energy and mass conservation, the average vapor velocity, u_v , is

$$u_v = \frac{16 q''_{\text{CHF,Z}}}{\pi\rho_v h_{\text{lv}}}. \quad (5.3)$$

Combining Eqn. 5.2 and Eqn. 5.3 leads to the CHF correlation in Eqn. 5.1. While this idealization is rational (albeit disputed) for unconfined conditions, as illustrated in Figure 5.1-b, the existence of a confinement wall above the boiling surface would surely prohibit the

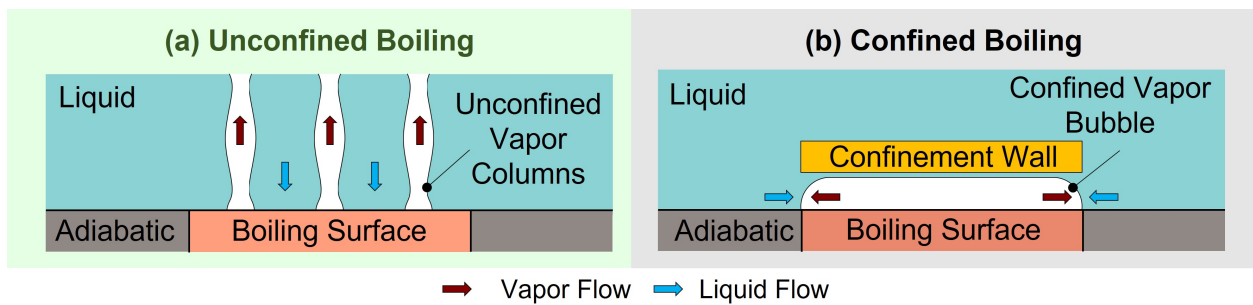


Figure 5.1. Two-phase interface dynamics comparison during unconfined and confined pool boiling. (a) Illustration of the theoretical framework for the hydrodynamic instability theory for predicting CHF in saturated pool boiling on an infinite unconfined flat plate. The CHF is postulated to occur when the two-phase interfaces of the unconfined vapor columns are unstable based on the Helmholtz criterion. (b) Illustration of the effect of a confinement wall above a horizontal boiling surface on the two-phase interface dynamics. Instead of forming vapor columns normal to the surface, vapor bubbles are forced to grow parallel to the boiling surface. In both panels, arrows indicate the liquid (blue) and vapor (red) flow paths.

formation of such vapor columns normal to the boiling surface. As a result, the mechanism of CHF for confined pool boiling is expected to differ significantly.

Several studies develop alternative approaches for predicting the CHF for confined pool boiling that do not use hydrodynamic instability frameworks. Chang and Yao [169] investigated the CHF phenomena in confined geometries by conducting experiments on a vertical cylindrical heater confined by a concentric tube where the bottom opening is sealed and the fluid can access the confinement cavity from the top opening only. In contrast to confined CHF models in Table 5.1, their developed confined CHF model is based on the well-established understanding of hydrodynamic countercurrent flooding in tubes, namely, the Wallis [170] correlation for countercurrent flooding. The final form of the confined CHF prediction based on the countercurrent flow framework is

$$\frac{q''_{\text{CHF,Co}}}{\rho_v h_{\text{fg}}} \sqrt{\frac{\rho_v}{gD(\rho_l - \rho_v)}} = \frac{0.38}{(1 + (\rho_v/\rho_l)^{0.25})^2(L/S)}. \quad (5.4)$$

In this configuration, gravity pulls the liquid down while buoyancy lifts the vapor up. The flooding phenomenon was best described as a transition from counter-current flow to a co-current flow, where the vapor flow reverses the flow direction of a fraction of the liquid entering the cavity [171]. While this framework is specifically tailored to the two-phase flow regimes expected in confined configurations, the chosen CHF triggering mechanism, countercurrent flooding, contradicts the experimental observations by others [172]–[174], which have shown that during confined boiling the heated surface partially dries out at high heat fluxes just before reaching the CHF condition. In other words, liquid only rewets regions near the confined heater perimeter, such that the interior regions of the gap further away from the perimeter are solely occupied by vapor. Chyu [175] also developed a confined CHF model not based on the hydrodynamic instability theory. Rather, their analysis was based on a one-dimensional momentum conservation of the two-phase flow in narrow vertical channels. Their analysis postulated that the CHF occurs when the buoyancy driven upward momentum is insufficient to balance the momentum of the displaced liquid and associated frictional forces. The expression CHF was derived to be

$$q''_{\text{CHF,Co}} = \rho_v h_{\text{lv}}(S/L) \left[\frac{gL \sin \theta (\rho_l / \rho_v - 2)}{1 + fL/(2S)} \right]^{0.5}, \quad (5.5)$$

where L is the channel length and f is the friction factor defined as

$$f = 0.13 \left(\frac{\rho_l - \rho_v}{\rho_v} \right)^{0.5} \left[s \left(\sqrt{g \frac{\rho_l - \rho_v}{\sigma}} \right) \right]^{1.3}. \quad (5.6)$$

While such a friction-based framework is suitable for vertical channels, where the buoyancy drives the vapor flow upward and liquid is supplied from the bottom inlet to the channel, it is challenging to extrapolate this framework into horizontal confined surfaces that have no clear distinction between liquid inlet and vapor outlet along the confinement perimeter. In contrast to earlier semi-empirical models, Zhao *et al.*[176] developed an analytical model for the confined CHF based on the depletion rate of the liquid microlayer underneath the confined bubble,

$$q''_{\text{CHF,Co}} = \frac{q_{\text{pl}}(t_{\text{ib}} + t_s) + \int_{t_{\text{ib}}+t_s}^{t_{\text{d}}+t_s} \frac{k\Delta T_s}{\delta_{\text{ma}}} dt}{\tau_{\text{D}}}, \quad (5.7)$$

where q_{pl} is the heat flux of the unconfined pool boiling, t_{d} , t_{ib} and t_s are respectively the total duration for the complete depletion of the microlayer underneath the coalesced confined vapor bubble, the microlayer evaporation duration at the critical thickness and the bubble growth time as the bubble reaches the confinement wall, δ_{ma} is the microlayer thickness, ΔT_s is the boiling surface superheat. The analysis considered that the confinement wall forces the individual vapor bubbles to grow parallel to the boiling surface resulting in coalescence and formation of a vapor ‘mushroom’ inside the confined space, where τ_{D} is the period of the vapor mushroom formation. This approach is impractical for engineering applications because many of terms in Eqn. 5.7 cannot be quantified *a priori* for a given confined boiling configuration.

5.3 CHF Model Development

The literature review above identified the lack of a mechanistic CHF correlations for confined boiling configurations that can be readily applied to across a wide range of parameters. Generally, the boiling process consists of a various energy transport process coupled with the flow hydrodynamics. Energy needs to transfer across the solid-liquid interface, through the liquid, and across the liquid-vapor interface; generated vapor must flow away while liquid rewets the boiling surface. Interruptions of any of these individual transport mechanisms would act to limit the overall boiling transport as well. Further, the specific boiling system configuration may determine which of these transport mechanisms is the rate-limiting factor. Hence, models for the CHF generally postulate that one of the transfer mechanisms is the weak link when developing the model framework [21]. Scattering of thermal energy carriers (phonons) across the solid-liquid interface (e.g., the Kapitza resistance) is unlikely to be the limiting transport mechanism [64], [177]. Similarly, the maximum possible vapor flux, and associated heat transfer rate, across the liquid-vapor interface based on kinetic theory is typically much larger compared to the other transfer mechanisms [65]. Thus, researchers have historically attributed the limit to hydrodynamic mechanisms, either focusing on the far-field vapor-liquid counterflow or the near-surface liquid delivery to the evaporating contact line [21].

Experimental visualizations including our own past work has revealed that confined boiling surfaces exhibit partial dryout as the CHF conditions are approached [172]–[174]. In other words, liquid does not rewet the entire boiling surface. Further, the fraction of the surface experiencing partial dryout qualitatively increases as the heat flux increases near the CHF condition. Therefore, the triggering mechanism for CHF in confined configuration should consider the near-surface micro-hydrodynamic forces around the triple contact line. In fact, this mechanism is argued to be the triggering mechanism even for unconfined pool boiling. Theofanous and colleagues [166], [178], [179] challenged the widely held view that the hydrodynamic instability is the triggering mechanism for pool boiling CHF and postulated that CHF is triggered when the forces along the triple contact line are balanced, leading to irreversible growth of a dry spot area on the boiling surface. Kandlikar [85] also used a

similar approach to develop a model for unconfined CHF that accounts for both surface wettability and orientation.

Considering this triggering mechanism for CHF in confined boiling, a predictive model must consider the forces acting on the two-phase interface. Figure 5.2-a depicts the forces considered in the model developed herein. Namely, surface rewetting is assumed to be governed by a balance between the surface tension force, F_S , the hydrostatic force, F_G , and the vapor recoil force, F_m . At low heat fluxes, both hydrostatic and surface tension forces can overcome the vapor recoil force allowing for complete rewetting of the boiling surface. On the other hand, as the applied heat flux increases, the vapor recoil force due to evaporation becomes larger than the combined hydrostatic and surface tension forces forming a partial dry patch at inner most region of confined space. The average equilibrium spread of the region experiencing partial dryout grows irreversibly proportional to the average applied heat flux until it encompasses the entire heater area, leading to a boiling crisis at the CHF condition. Furthermore, the two-phase interface is assumed to undergo unstable undulations along its perimeter, as illustrated in Figure 5.2-b. Just prior to CHF, the two-phase undulation is assumed to be at the heater perimeter where only a portion of the two-phase interface is in contact with the boiling surface. In the model developed below, it is important to note that the heater surface is assumed to entirely cover one side of the confinement gap while the opposing confinement wall is assumed to be adiabatic, as shown.

Vapor recoil forces the contact line to recede and can be evaluated based on the dynamic pressure, P_d , of the vapor phase:

$$P_d \approx 1/2\rho_v u_v^2. \quad (5.8)$$

Assuming that all of the heat is dissipated by the latent heat of vaporization, the vapor velocity is

$$u_v = \frac{q_i''}{\rho_v h_{lv}}, \quad (5.9)$$

where q_i'' is the heat flux at the vaporization interface, which can be expressed as $q_i'' = (q_b'' A_b) / A_i$ where the subscript b indicates heat flux based on the area of the boiling surface.

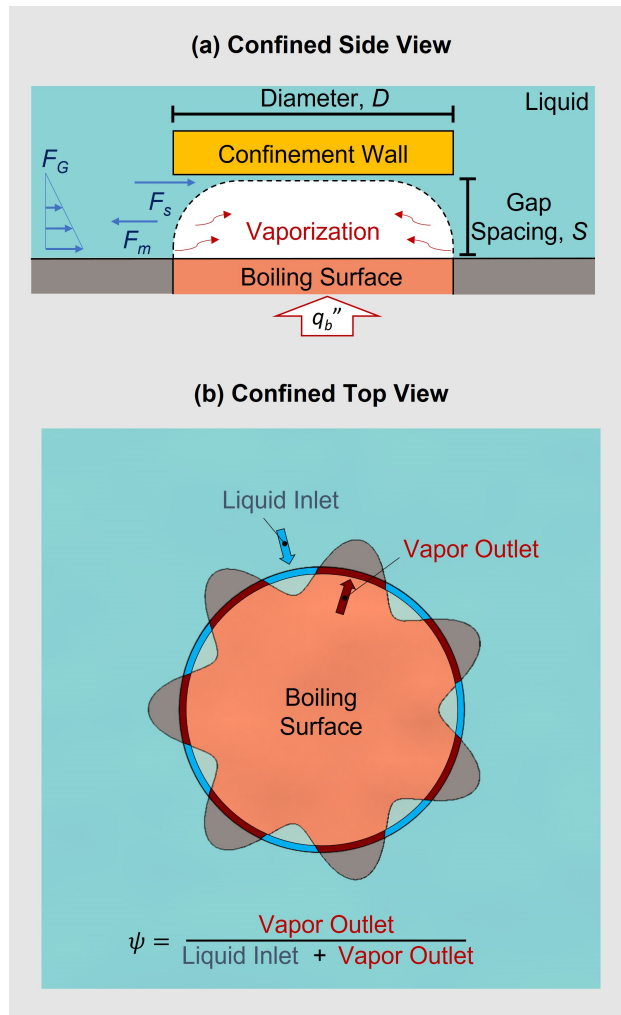


Figure 5.2. Micro-hydrodynamics at the contact line as the governing mechanism for CHF in confined geometries (a) Side-view schematic of the cross-section of the confined boiling system where a bubble is growing within a gap spacing, S , from the boiling surface of a diameter, D . Forces governing the two-phase interface dynamics are illustrated with blue arrows. These include the hydrostatic forces, F_G , surface tension forces, F_S , and the vapor momentum forces, F_m . (b) Cross-sectional top view of the base of the confined vapor bubble just prior to CHF. Undulations in the perimeter of the bubble extend partially outside the confined boiling region allowing partial rewetting of the boiling surface near the confinement space perimeter (*i.e.*, the liquid inlet regions). The ratio of the vapor outlet regions (shown in red) to the full perimeter of the boiling surface (combined red and blue line), defined as ψ , is the single fitting parameter in our newly developed correlation.

The area of the two-phase interface depends on its shape of the two-phase interface and is an unknown. However, the vaporization area at CHF is assumed to be linearly correlated with the confinement inlet-outlet opening area to the unconfined reservoir, A_{gap} . A correlation parameter, ψ , is hence introduced and represents the ratio of the interface area to the confinement opening area. This ratio is assumed to be dependent on the working fluid properties only. Combining the equations above results in the following expression for the vapor momentum force:

$$F_m = \frac{q_b'^2 A_b^2}{2\rho_v h_{lv}^2 A_{\text{gap}}(1 - \psi)}. \quad (5.10)$$

At the CHF condition, the model postulates that the vapor recoil forces are balanced by surface tension and hydrostatic pressure. Surface tension acts at the three-phase contact lines of the confined vapor. Because the confinement wall is adiabatic, we assume that no evaporation takes place from the top two-phase interface of the confined vapor bubble. Hence, a liquid layer over the confinement wall is preserved and not depleted at CHF (i.e., the confinement wall remains completely wetted). This assumption agrees with visual observations from our previous work [172]. On the other hand, the evaporating liquid microlayer on the boiling surface is assumed to be completely depleted such that the contact line is normal to the boiling surface. Based on these assumptions, the surface tension forces acting at the liquid layer over the adiabatic confinement wall can be expressed as:

$$F_s = \epsilon\sigma, \quad (5.11)$$

where ϵ is the perimeter of the boiling surface. It is worth noting that the proposed CHF model assumes that the microlayer contact is completely depleted at CHF such that the triple contact line is normal to the boiling surface. However, if this condition is not satisfied the influence of the contact angle would be included in model fitting where the contact angle is lumped with other fluid properties in one fitting parameter, ψ . Lastly, the hydrostatic force can be expressed in term of the effective depth of the interface, H_i , as follow:

$$F_G = H_i g(\rho_l - \rho_v) A_{\text{gap}}. \quad (5.12)$$

Critical heat flux is triggered when

$$F_s = F_s + F_G. \quad (5.13)$$

Combining Equations (5.10-5.13) yields an expression for CHF:

$$q''_{\text{CHF,Co}} = \sqrt{\frac{2\rho_v h_{\text{lv}}^2 A_{\text{gap}}(1 - \psi)}{A_b^2} (\epsilon\sigma + H_i g(\rho_l - \rho_v) A_{\text{gap}})}; \quad \left(\frac{q''_{\text{CHF,Co}}}{q''_{\text{CHF,Z}}} < 1 \right). \quad (5.14)$$

The development of the confined CHF expression enables the prediction of the gap spacing threshold, below which confinement reduces the CHF compared to unconfined pool boiling. The predicted gap spacing threshold corresponds to the value where the confined CHF (Eqn. 5.14) matches the unconfined pool boiling CHF (Eqn. 5.1). Hence, the geometrical confinement effect on CHF can be indicated by the ratio between confined CHF and unconfined CHF:

$$\frac{q''_{\text{CHF,Co}}}{q''_{\text{CHF,Z}}} = \sqrt{\frac{2A_{\text{gap}}(1 - \psi)\epsilon}{K^2 A_b^2} \left(L_c + \frac{H_i A_{\text{gap}}}{\epsilon L_c} \right)}, \quad (5.15)$$

where K is the dimensionless unconfined CHF ratio defined in Eqn 5.1 and L_c is the capillary length of the working fluid. Boiling is considered unconfined when the confined CHF to the unconfined CHF ratio is larger than unity. Figure 5.5 illustrates the absolute mean error of the confined CHF model increases if the proposed cutoff is increased beyond the threshold values of unity. Thus, the model proposed here is deemed accurate for cases where the predicted CHF with confinement is lower than the CHF predicted for unconfined boiling.

The generic expression for CHF in Eqn. 5.14 can be expressed for a particular geometry. For example, the CHF for a circular horizontal confined boiling surface of a diameter, D , and gap size, S , is

$$q''_{\text{CHF,Co}} = \sqrt{\frac{32\rho_v h_{\text{lv}}^2 S(1 - \psi)}{D^2} \left(\sigma + g \frac{S^2}{2} (\rho_l - \rho_v) \right)}. \quad (5.16)$$

Similarly, the CHF expression can be tailored to an inclined straight channel of length, L , uniform rectangular cross-sectional area with channel height, *i.e.* gap size, S and channel width, W . When the channel is submerged in liquid pool with two openings at both ends of the channel and inclination angle, θ , where $\theta = 90^\circ$ represents a vertical channel, the CHF can be expressed as:

$$q''_{\text{CHF,Co}} = \sqrt{\frac{8\rho_v h_{lv}^2 S(1-\psi)}{L^2} \left(\sigma + g(SL \sin \theta + \frac{S^2}{2} \cos \theta)(\rho_l - \rho_v) \right)}. \quad (5.17)$$

5.4 Results and Discussion

The confined pool boiling CHF model presented by Eqn. 5.14 is compared to experimental data available from 10 distinct studies in the literature [100], [102], [111]–[113], [115], [172], [180]–[182]. To the best of our knowledge, this dataset comprises all the data that quantifies the effect the gap spacings on the CHF of confined pool boiling, in particular where there is an adiabatic wall parallel to the heated surface (and having the same area) that confines the boiling to the narrow gap formed between. All data are under atmospheric pressure conditions and for flat boiling surfaces without enhancement modifications such as porous coatings. This data set includes a total of 197 experimental measurement of CHF under confined conditions using various working fluids that include water, ethanol, FC-72, HFE-7100, R113, n-pentane, and benzene. In general, two confinement geometries are considered, circular horizontal confined boiling surfaces (Eqn. 5.16) and both vertical and inclined rectangular channels where heating is applied to one side of the channel and the entire channel is submerged in a liquid pool (Eqn. 5.17). Table 5.2 summarized the dataset including the ranges of confinement gap spacings.

Table 5.2. Collected database of experimental CHF in confined geometries.

Working Fluid	Shape	Geometry Range	Reference
Water	Circular Horizontal	S = [0.2-2.2] mm D = 25.4 mm	[172]
n-pentate	Circular Horizontal	S = [0.1-0.5] mm D = 12 mm	[180]
Water	Circular Horizontal	S = [0.1-0.3] mm D = [5-20] mm	[100]
Water, R113, Ethanol, Benzene	Circular Horizontal	S = [0.1-8] mm D = [10-20] mm	[112]
Water	Circular Horizontal	S = 0.1 mm D = 20 mm	[181]
HFE-7100	Circular Horizontal	S = [0.5-3.5] mm D = 30 mm	[102]
R113	Rectangular Vertical Channel	S = [0.3 – 2.5] mm L = 50 mm W = 20mm	[111]
FC72	Rectangular Vertical Channel	S = [0.4 – 1] mm L = 20 mm W = 20 mm	[182]
Water, Ethanol	Rectangular Vertical Channel	S = [0.45-5] mm L = [20-50] mm W = 10 mm	[115]
Water	Inclined Rectangular Channel	S = [1-2] mm L = 35 mm W = 15 mm; $\theta = [0 - 90]$	[113]

As discussed in the confined CHF model development above, the ratio of the interface area to the confinement opening area is an unknown assumed to depend on the working fluid. In effect, estimated values for ψ are obtained through a least-squares fitting of the model predictions to the experimental dataset. The predictive model is also able to predict the gap spacing threshold, below which confinement reduces the CHF compared to unconfined pool boiling, as well as accurately predict this reduction of the CHF.

Figure 5.3 compares the CHF model predictions to the experimental data points categorized by fluid type. The vapor area ratio is found to range from $0.92 < \psi < 0.97$ across various working fluids. The experimental and predicted values are both normalized against Zuber’s limit for unconfined boiling (Eqn. 5.1). The proposed model accurately depicts the effect of confinement on CHF, as indicated by the agreement with the experimental data in the range of where the predictions are less than gap spacing threshold estimated by the Zuber limit ($q''_{CHF,Co} < q''_{CHF,Z}$). In this range, the predictions collapse within the gray-shaded region indicating $\pm 30\%$ from the experimental data. As expected, the model is not suitable when it predicts a CHF value larger than the Zuber limit ($q''_{CHF,Co} > q''_{CHF,Z}$). In this range, the experimental data are accurately predicted by Zuber’s limit, with the data points collapsing into the green-shaded region indicating $\pm 30\%$ from Zuber’s limit. In practice, the proposed model should be employed for accurate prediction of CHF only for gap spacings below the threshold, and above the threshold Zuber’s limit should instead be used. Thus, the predicted threshold in the gap spacing separating the confined and unconfined boiling regimes thereby corresponds to approximately unity in the normalized predicted heat flux value ($q''_{CHF,Co}/q''_{CHF,Z}=1$) and the limiting gap spacing, S , can be determined as a function of system parameters from Equations 5.15 - 5.17.

Figure 5.4 compares the error in the prediction of CHF data for gap spacings below the threshold using the model developed in this work to other models in the literature, which are based on different triggering mechanism for CHF. The threshold gap spacing is defined uniquely for each model when the predicted CHF matches Zuber’s limit for pool boiling. Several works [101], [111]–[115] based on the hydrodynamic instability framework are illustrated in green in Figure 5.4. Despite having a low mean error, these models demonstrate the widest range of error among the tested models, indicating their lack of generality in predicting confined CHF across different geometries and fluid types. This is attributed to the fact that these models presume a CHF triggering mechanism that is associated with unconfined boiling when developing the empirical correlation.

The correlations of Chang and Yao [169] and Chyu [175], highlighted in blue in Figure 5.4, include the confinement effects on the hydrodynamics of the two-phase interface. This framework reduces the spread of error; however, both models drastically underestimate the

CHF values on average. The model of Chang & Yao [169] postulates that CHF coincides with the countercurrent flooding phenomenon. Yet, there are experimental observations indicate the flooding, or partial dryout, occurs at heat fluxes lower than the CHF value [172]–[174]. This explains the tendency of the model to underestimate the experimental CHF values in confined configurations. Similarly, the model of Chyu [175], which is based on a friction framework, underestimates CHF values. This model assumes that the generated vapor traverses the entire confined space from the evaporation interface at the liquid inlet opening to the unconfined space through a vapor outlet opening. While this scenario can be correct in vertical channels, during confined boiling in a horizontal gap, the inlet and outlet openings are not well defined and generated vapor does not necessarily flow through the entire confined space.

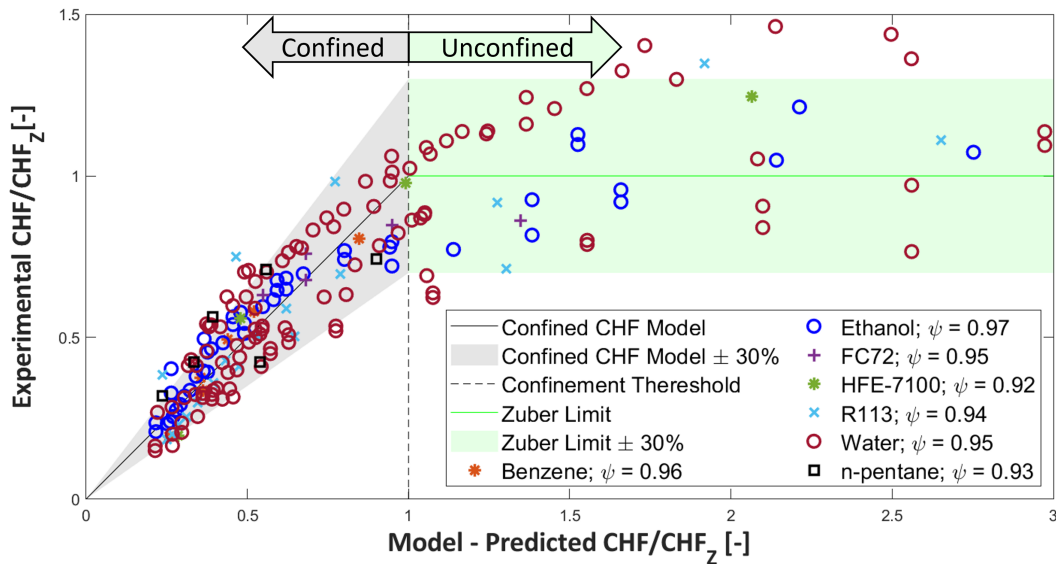


Figure 5.3. Assessment of the proposed model for CHF in confined geometries. Both the experimental and predicted CHF are normalized by the prediction for the unconfined CHF from Zuber [71]. The solid black reference line indicates a perfect match, and the gray shaded region indicates $\pm 30\%$ from this reference line. This comparison is limited to a region where the proposed model is valid, namely, up to Zuber’s limit for unconfined conditions (a value of 1 on the normalized axes). Thereafter, a green line indicates Zuber’s limit and the shaded region illustrates $\pm 30\%$ around this limit.

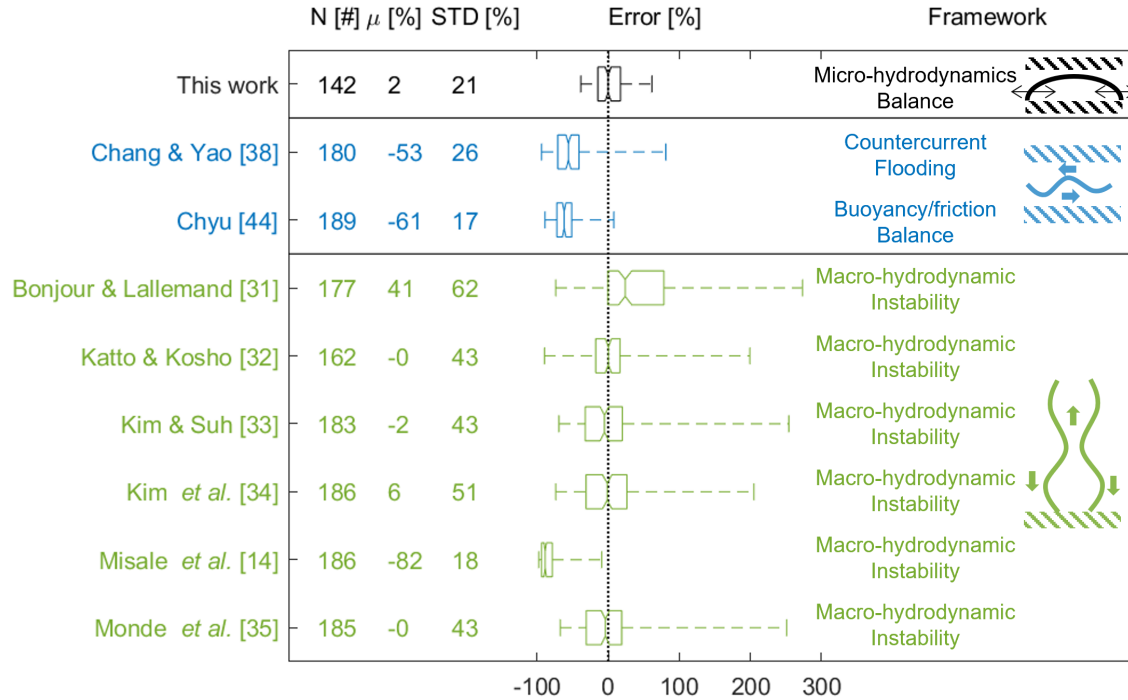


Figure 5.4. Accuracy of the confined CHF models. The error is calculated by comparing the model to the experimental data points (N) in the dataset that are below the gap spacing threshold. The mean (μ) and standard deviation (STD) of the prediction error for each model are tabulated within the plot. The notch in the box marks the mean error, whereas the box edges mark the 25th and the 75th percentiles. The dashed whiskers illustrate the full range of the calculated error in the data set. The results of the proposed model that is based on the micro-hydrodynamics balance in this work is shown in black in the first row, demonstrating low mean error and a narrow spread of the error compared to the models shown in subsequent rows that are based on alternative frameworks.

The confined CHF model proposed in this work based on a micro-hydro-dynamics force balance, as marked in black in the top row, demonstrates both a very low mean error and narrow spread of error compared to other existing models. We believe the enhanced accuracy of this model is due to capturing the correct triggering mechanism for CHF in confined geometries. Specifically, the boiling crisis in confined geometries is caused by an imbalance of forces acting on the triple contact line that leads to irreversible growth of the dry spot on the boiling surface.

5.5 Summary

The boiling crisis in confined geometries has been previously described using empirical corrections made to models originally developed for unconfined geometries, which limits their accuracy outside a small range of applicability. To aid in engineering design, it is necessary to develop more generalized mechanistic CHF models for confined boiling. Therefore, it is critical to identify the triggering mechanism for CHF specific to boiling in these confined configurations. In this work, we developed a new mechanistic CHF model that accurately predicts the influence of confinement geometry on the boiling crisis. The model postulates that the insufficient liquid rewetting forces at the boiling surface edges are the triggering mechanism for CHF in confined geometries. A modeling framework was therefore developed based on the micro-hydrodynamics of the triple contact line on the boiling surface considering the competing vapor recoil, surface tension, and hydrostatic forces that govern the two-phase interface dynamics. Dryout is triggered when the vapor recoil force due to vaporization at the two-phase interface balances the combined surface tension and hydrostatic forces, leading to irreversible dryout of the surface.

The accuracy of the newly developed model is assessed by comparing to all available experimental data for confined CHF in the literature, consisting of 7 working fluids and a range of confinement gap spacings, heater sizes, shapes, and orientations. Notably, the model is able predict CHF for horizontal confined surfaces that have no clear distinction between liquid inlet and vapor outlet along the confinement perimeter. The model is able to predict the experimental CHF data with a mean percentage error of 2% and a standard deviation of 21% when the boiling dynamics are governed by confinement, a vast improvement compared to other confined CHF models available in the literature. The model is also able to identify the limit at which confinement no longer affects CHF, above which unconfined pool boiling CHF models should be used. In addition to offering a prediction tool for pool boiling CHF in confined conditions, this work provides a framework that can potentially be extended to include additional forces, such as liquid momentum forces, for predictions in flow boiling applications.

5.A Confinement Threshold Limit

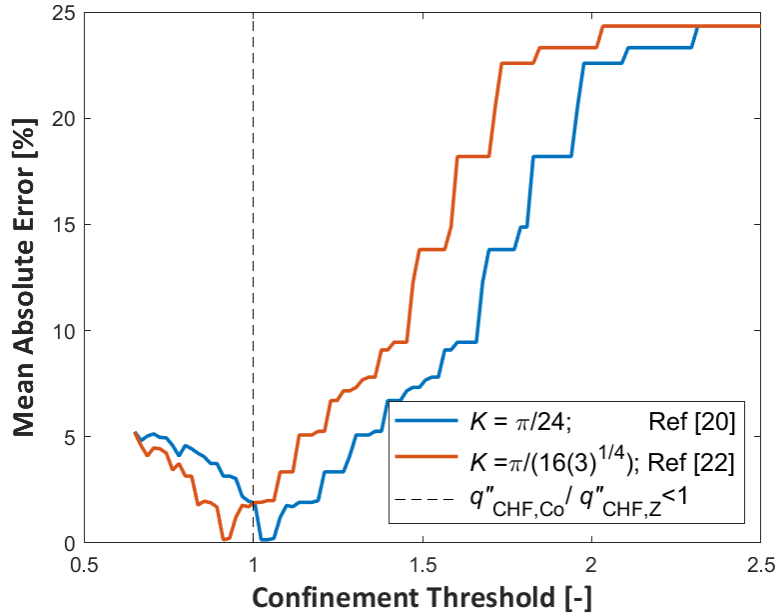


Figure 5.5. Sensitivity of the Confinement Threshold. The error is calculated by comparing the model for the confined CHF model (Eqn. 5.14) to the experimental data points in the dataset that are below the proposed confinement threshold limit (Eqn. 5.15). The vertical black dashed line corresponds to the confinement threshold of one where the confined CHF matches the unconfined CHF. The confinement threshold depends on the dimensionless unconfined CHF ratio, K . The error is calculated for two values of K found in the literature (blue and orange lines). In both cases, the minimum error is found near a ratio of one indicating that the cutoff in the applicability of the model is when the predicted CHF with confinement match the unconfined prediction.

6. CONCLUSIONS AND FUTURE OUTLOOK

6.1 Conclusions

This dissertation investigated the implications of the high degree of geometrical confinements on two-phase heat dissipation characteristics. Specifically, this work experimentally quantified the thermal and the hydrodynamic impact of gap spacing above the boiling surface and the fraction of the area within the confined region heated by the boiling surface. Then, leveraging the understanding of phenomena involved in confined boiling, a mechanistic-based model was developed to predict the implication of geometrical confinement on thermal characteristics. This dissertation advances the current state of knowledge regarding the implications of geometrical confinements on boiling regimes, heat transfer coefficient, and critical heat flux.

Experimental results showed that the thermofluidic characteristics of the two-phase heat transfer are significantly affected by the spatial confinement. This work revealed the existence of two distinct boiling regimes uniquely observed in boiling in confined configurations (namely, intermittent boiling and partial dryout). Intermittent boiling exhibits a time-periodic oscillatory behavior where the heat dissipation method from the boiling surface alternate between single-phase and two-phase heat dissipation. In a nucleation-active confined boiling, rewetting liquid from unconfined pool lowers the surface superheat and boiling ceases monetarily until the surface heats up to the nucleation temperature. On the other hand, in the partial dryout confined boiling regime, portion of the surface remain continually dried out, where the capillary forces are insufficient to overcome the viscous resistance necessary to completely rewet the boiling surface.

Previous experimental studies reported that geometrical confinement improves the heat transfer coefficient and purported that the primary mechanism of enhancement is the enlargement of the evaporative microlayer area underneath the distorted vapor bubble. However, this mechanism cannot explain all the observations of heat transfer enhancement. Chapter 3 proposed nucleation enhancement wetting as a complimentary enhancement mechanism in nucleation-active confined boiling. Particularly, the confinement wall enhances the liquid micro-convection flow parallel to the boiling surface which improves the rewetting of the dry

spots on the boiling surface. On the other hand, for extremely confined boiling, Chapter 4 reported the observation of nucleation-suppressed boiling. The flow visualization revealed small residual vapor pockets, termed ‘stem bubbles’, remain on the surface through a pinch-off process as vapor bubbles escape the confinement. The presence of these stem bubbles seeds the consequent vapor generation cycle and mitigates the need for bubbles to nucleate on the surface. Stem bubbles dominate the enhancement in extremely confined boiling surpassing the maximum enhancement limit of nucleate-active boiling.

Lastly, the confinement wall restricts the replenishing of liquid and limits the rewetting of the boiling surface. As a result, confinement significantly lowers the dryout limit. This effect is exacerbated when the confinement wall extends beyond the heated region of the boiling surface. In Chapter 5, a mechanistic-based model for confined CHF is developed based on the micro-hydrodynamic force balance along the triple contact line. The developed model postulated that the CHF occurrences coincide with the irreversible growth of the dry spot on the boiling surface. The developed model demonstrated improved accuracy compared to alternative model which enables increased confidence in the actual CHF limit.

6.2 Future Outlook

The reported improved mechanistic understanding of heat transfer characteristics in confined boiling has an important impact and offers a new direction for designing compact two-phase thermal management solutions. However, further research efforts are needed to facilitate the technology transfer into practical systems. Specifically, scientific investigations to aid the development of the confined boiling technology targeting three objectives are proposed. First, the use of stem bubble boiling enhancement for dielectric coolants. Second, developing a technique to control the formation of stem bubbles. Third, developing guidelines to use the confinement wall wettability in order to improve the thermal performance of extremely compacted two-phase heat exchangers.

6.2.1 Stem Bubble Boiling of Dielectric Coolants

Water is an excellent working fluid from the thermal management perspective; however its use is often prohibited in applications requiring electric insulation such as the direct cooling of electronics and power devices. Highly wetting dielectric working fluids, including perfluorocarbons, hydrofluoroethers, and fluoroketones, are commercially available. However, the high wetting nature of those working fluid cause appreciable penetration of the liquid into the boiling surface cavities. The penetration yields vapor embryos that are smaller than the surface cavities, hence, increasing the incipience surface superheat. Previous studies reported that 46 °C surface superheat is required to initiate nucleation of perfluorocarbons (for example, FC-72) [183]. This thermal overshoot can potentially cause thermal shock to the electronic package and lead to reliability complications. Stem bubble boiling can be sustained without the need for continually active nucleation sites. Hence, operating in this regime can potentially overcome these challenges. In particular, observations reveal that stem bubbles are formed only when the confinement gap is smaller than a spacing threshold. In order to harness the enhancement of this boiling behavior in application, it is crucial to predict the gap spacing threshold below which these stem bubbles form. In Chapter 4, a framework was introduced to identify the threshold spacing with relation to the physical properties of the working fluid. However, this framework needs to be validated with dielectric working fluids. Hence, I propose to extend the experiments t dielectric fluids in order to further validate the framework.

6.2.2 Control the Formation of Stem Bubbles

The chaotic nature of boiling has a stochastic effect on forming the residual stem bubble within the confined space. In other words, even for a steady constant operating condition, there is a probability of complete vapor bubble escape for which a stem vapor bubble is not left behind for the next bubble generation cycle. In this case, active nucleation sites are required to reinitiate phase change on boiling surface. Since, these nucleation-site vapor embryos have smaller radius than the vapor stem bubble, the heat will momentarily be dissipated through the sensible heating of local fluid until the minimum superheat required

for nucleation site activation is reached. As result, the momentary pause of phase change would lower the time average heat transfer coefficient. As an illustration, boiling curves for hydrophilic confinement wall is collected and compared to the untreated confinement wall. Visualization of the two-phase interfaces confirms that hydrophilic surfaces promote the complete rewetting of the confined boiling surface. Therefore, stem bubble enhancement are reduced for hydrophilic surface compared to the untreated surfaces as shown in Figure 6.1. To increase the probability of stem bubble formation, I propose the use of heterogeneous surfaces with patterns of hydrophobic sites within the hydrophilic surface. Hydrophobic site can split the trapped vapor bubble as it escapes the confinement, lowering the probability of complete rewetting of the boiling surface as shown in Figure 6.2. In addition, the location of the stem bubbles might be influenced by the location of the hydrophobic split sites. To this end, hydrophobic split sites can be strategically located close to hot spots to potentially improve the local heat transfer coefficient.

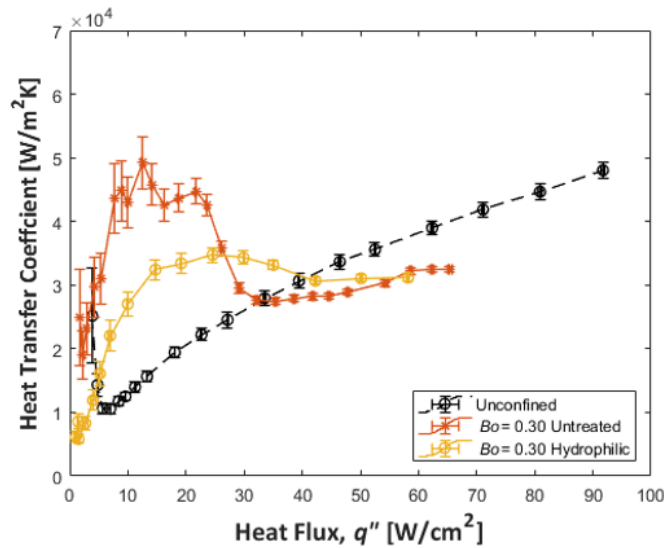


Figure 6.1. Illustration of the confinement wall wettability effect on the heat transfer coefficient. Hydrophilic confinement wall promote complete rewetting of the boiling surface which reduces the enhancement associated with stem bubbles.

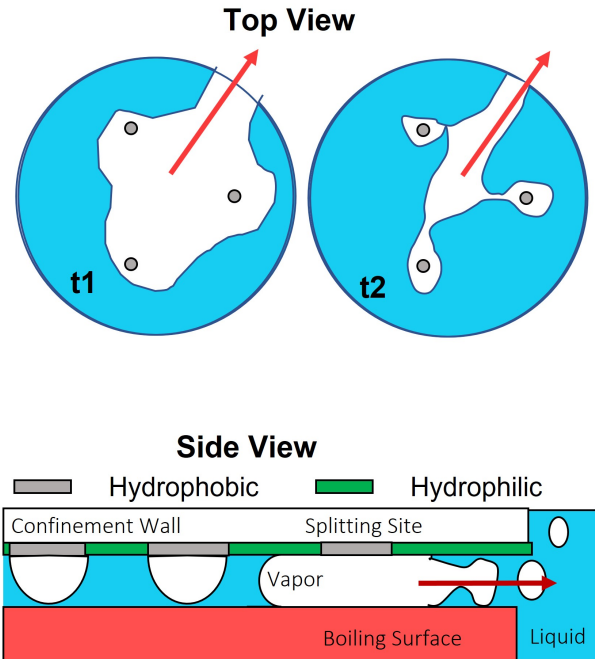


Figure 6.2. Illustration of the confinement wall wettability pattern concept for improving probability of stem bubble formation. Hydrophobic sites splits the vapor bubble as it escapes the confinement reducing the probability of complete rewetting.

6.2.3 Use Confinement Wall Wettability for Confined CHF Enhancement

While confinement enhances the heat transfer coefficient, it has been demonstrated that confinement reduces the critical heat flux (CHF) of a boiling surface significantly. Even more severe reductions in CHF are observed when the region with confined fluid thickness is extended to an area larger than the heated zone. Chapter 5 illustrated that forces governing the near-field liquid rewetting at the confined heater edge are critical in determining the maximum heat flux that can be dissipated through the confined boiling surface. Mainly, the confined CHF, Equation 5.14, is determined by the geometrical dimensions, working fluid properties, and the ratio of vapor area at the confinement edge, α . While geometrical dimension and working fluid can be easily controlled to achieve the targeted CHF, constraints can be imposed on the limit is which those two factors can be manipulated. For example, thermal management solutions in electronic packages have restrict volumetric constrains and fluid properties constrains. In such cases, the manipulation of the ratio of vapor area at the

confinement perimeter can be advantageous in enabling the dissipating of targeted power of the confined boiling surfaces. I propose the use of super hydrophobic patterns on the confinement wall to designate vapor outlet and liquid intel sections along the confinement perimeter as shown in Figure 6.3. The super hydrophobic layer can facilitate the formation of a thin vapor layer on the confinement wall. As the trapped vapor bubble expands and reaches the super hydrophobic region, vapor regions can coalesce reducing the mass transport resistance for the radial outflow of vapor in selected regions only

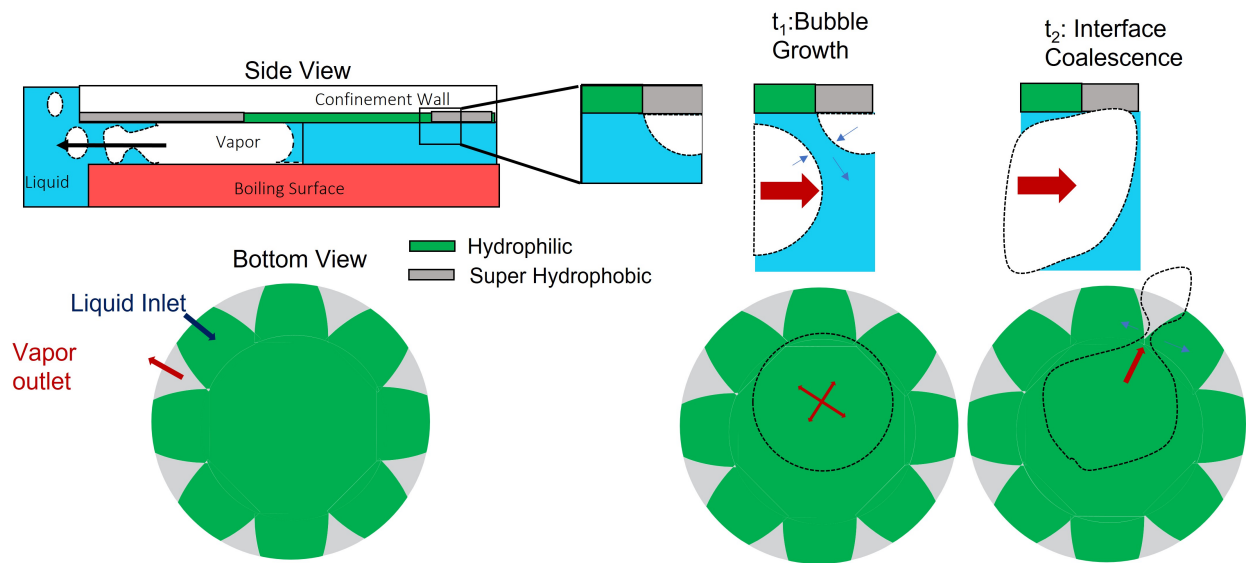


Figure 6.3. Illustration of the confinement wall wettability pattern concept for manipulating the vapor area ratio at the confinement perimeter. The thin vapor layer on the super hydrophobic surface coalesce with the expanding trapped vapor bubble. As a results, mass transport of teh radially outflow of vapor is reduced on selected sections only.

REFERENCES

- [1] J. Buongiorno, M. Corradini, J. Parsons, and D. Petti, “Nuclear Energy in a Carbon-Constrained World: Big Challenges and Big Opportunities,” *IEEE Power and Energy Magazine*, vol. 30, pp. 365–401, 1 1988.
- [2] C. Cai, I. Mudawar, and H. Liu, “Mechanistic Method to Predicting Minimum Heat Flux Point Wall Temperature in Saturated Pool Boiling,” *International Journal of Heat and Mass transfer*, vol. 156, 119854 2020.
- [3] I. Mudawar, “Recent Advances in High-flux, Two-phase Thermal Management,” *Journal of Thermal Science and Engineering Applications*, vol. 5, p. 021 012, 2013.
- [4] S. Nukiyama, “The Maximum and Minimum Values of the Heat Q Transmitted from Metal to Boiling Water Under Atmospheric Pressure,” *Journal of Japanese Society of Mechanical Engineers*, vol. 37, pp. 367–374, 1934.
- [5] N. Nishikawa, “Historical Development in the Research of Boiling Heat Transfer,” *Journal of Japanese Society of Mechanical Engineers*, vol. 30, pp. 897–905, 264 1987.
- [6] V. K. Dhir, “Boiling Heat Transfer,” *Annual Review of Fluid Mechanics*, vol. 30, pp. 365–401, 1 1988.
- [7] J. H. Lienhard, “Snares of Pool Boiling Research: Putting our History to Use,” in *IMAPS Device Packaging Conference*, Fountain Hills, AZ, USA, 2018.
- [8] L. Cheng, “Fundamental Issues of Critical Heat Flux Phenomena During Flow Boiling in Microscale-channels and Nucleate Pool Boiling in Confined Spaces,” *Heat Transfer Engineering*, vol. 34, pp. 1016–1043, 2013.
- [9] D. Reay, *Heat pipes. Theory, Design and Applications*, 6th edition. Elsevier, 2014.
- [10] J. A. Weibel and S. V. Garimella, “Chapter Four - Recent Advances in Vapor Chamber Transport Characterization for High-Heat-Flux Applications,” *Advances in Heat Transfer*, vol. 45, pp. 209–301, 2013.
- [11] W. Rohsenow, “A Method of Correlating Heat Transfer Data for Surface Boiling of Liquids,” *Trans ASME*, vol. 74, pp. 969–975, 1952.
- [12] T. Bergman, A. Lavine, F. Incropera, and D. Dewitt, *Fundamentals of Heat and Mass Transfer*, Seventh edition. John Wiley and Sons, 2011.
- [13] K. Forster and N. Zuber, “Dynamics of Vapor Bubbles and Boiling Heat Transfer,” *AIChE J*, vol. 1, pp. 531–535, 1955.

- [14] K. Forster and R. Greif, “Heat Transfer to a Boiling Liquid – Mechanisms and Correlations,” *ASME J. Heat Transfer*, vol. 81, pp. 45–51, 1959.
- [15] J. Jung, S. Kim, and J. Kim, “Observations of the Critical Heat Flux Process During Pool Boiling of FC-72,” *J. Heat Transfer*, vol. 136, pp. 041501-1–041501-12, 2014.
- [16] B. Mikic and W. Rohsenow, “Bubble growth rates in non-uniform temperature field,” *Prog. Heat Mass Transf*, vol. 2, pp. 283–292, 1969.
- [17] N. Zuber, “Nucleate Boiling - The Region of Isolated Bubbles - Similarity with Natural Convection,” *International Journal of Heat and mass Transfer*, vol. 6, pp. 53–65, 1963.
- [18] S. V. Stralen, “The boiling paradox in binary liquid mixtures,” *Chem. Eng. Sci*, vol. 25, pp. 149–171, 1970.
- [19] R. Judd and K. Hwang, “A Comprehensive Model for Nucleate Boiling Heat Transfer, Including Microlayer Evaporation,” *ASME J. Heat Transf*, vol. 98, pp. 623–629, 1976.
- [20] K. Stephan and M. Abdelsalam, “Heat-transfer Correlations for Natural Convection Boiling,” *Int. J. Heat Mass Transf*, vol. 32, pp. 73–87, 1980.
- [21] V. P. Carey, *Liquid-Vapor Phase-Change Phenomena*, Second. New York, NY: Taylor and Francis, 2008.
- [22] V. P. Carey, *Liquid-Vapor Phase-Change Phenomena : An Introduction to the Thermophysics of Vaporization and Condensation Processes in Heat Transfer Equipment*, third edition. CRC Press, 2020.
- [23] E. Harvey, W. McElroy, and A. Whiteley, “On Cavity Formation in Water,” *J. Appl. Physf*, vol. 18, pp. 162–172, 1947.
- [24] T. Knapp, “Cavitation and nuclei,” *Trans. ASME*, vol. 80, pp. 1315–1324, 1958.
- [25] R. Sabersky and C. Gates, “Effect of Pressure on Start of Nucleation in Boiling Heat Transfer,” *Jet Propul*, vol. 25, p. 67, 1955.
- [26] Y. Y. Hsu, “On the Size Range of Active Nucleation Cavities on a Heating Surface,” *ASME. Journal of Heat Transfer*, vol. 84, pp. 207–213, 1962.
- [27] M. Jakob and W. Fritz, “Versuche tiber den Verdampfungsvorgang,” *Forsch. Geb. Ing*, vol. 22, pp. 435–447, 1931.
- [28] H. Kurihara and J. Myersr, “The Effects of Superheat and Surface Roughness on Boiling Coefficients,” *AICHE J*, vol. 6, pp. 83–91, 1960.

- [29] S. Chowdhury and R. Winterton, “Surface Effects in Pool Boiling,” *Int. J. Heat Mass Transfer*, vol. 28, pp. 1881–1889, 1985.
- [30] Y. Y. Hsu and R. W. Graham, “An Analytical and Experimental Study of the Thermal Boundary Layer and Ebullition cycle in Nucleation Boiling,” *NASA*, vol. TN-D-594, 1961.
- [31] P. Marto and W. Rohsenow, “Effects of Surface Conditions on Nucleate Pool Boiling of Sodium,” *J. Heat Transfer*, vol. 88, pp. 196–203, 1966.
- [32] K. Ferjancic and I. Golobic, “Surface Effects on Pool Boiling CHF,” *Exp. Therm. Fluid Sci.*, vol. 25, pp. 565–571, 2002.
- [33] H. Hu, J. A. Weibel, and S. V. Garimella, “A Coupled Wicking and Evaporation Model for Prediction of Pool Boiling Critical Heat Flux on Structured Surfaces,” *International Journal of Heat and Mass Transfer*, vol. 136, pp. 373–382, 2019.
- [34] H. J. Kwak, J. H. Kim, B. S. Myung, M. H. Kim, and D. E. Kim, “Behavior of Pool Boiling Heat Transfer and Critical Heat Flux on High Aspect-ratio Microchannels,” *International Journal of Thermal Science*, vol. 125, pp. 111–120, 2018.
- [35] N. Dhillon, J. Buongiorno, and K. Varanasi, “Critical Heat Flux Maxima During Boiling Crisis on Textured Surfaces,” *Nature Communication*, vol. 6, pp. 1–12, 2015.
- [36] W. Nakayama, T. Daikoku, and T. Nakajima, “Effects of pore diameters and system pressure on saturated pool nucleate boiling heat transfer from porous surfaces,” *J. Heat Transfer*, vol. 104, pp. 286–291, 1982.
- [37] J. Chang and S. You, “Heater Orientation Effects on Pool Boiling of Micro-porous-enhanced Surfaces in Saturated FC-72,” *J. Heat Transfer*, vol. 118, pp. 937–943, 1996.
- [38] S. Kim, G. Lee, J. Kang, K. Moriyama, M. Kim, and H. Park, “Boiling heat transfer and critical heat flux evaluation of the pool boiling on micro structured surface,” *Int. J. Heat Mass Transfer*, vol. 91, pp. 1140–1147, 2015.
- [39] Y. Takata, S. Hidaka, J. Cao, *et al.*, “Effect of Surface Wettability on Boiling and Evaporation,” *Energy*, vol. 30, pp. 209–220, 2005.
- [40] L. Heitich, J. Passos, E. Cardoso, M. da Silva, and A. Klein, “Nucleate Boiling of Water Using Nanostructured Surfaces,” *J Braz. Soc. Mech. Sci. Eng.*, vol. 36, pp. 181–192, 2014.
- [41] B. Kim, H. Lee, S. Shin, G. Choi, and H. Cho, “Interfacial Wicking Dynamics and its Impact on Critical Heat Flux of Boiling Heat Transfer,” *Appl. Phys. Letters*, vol. 105, pp. 191671-1–191671-4, 2014.

- [42] M. Rahman, E. Ölçerögl, and M. McCarthy, “Role of Wickability on the Critical Heat Flux of Structured Superhydrophilic Surfaces,” *Langmuir*, vol. 30, pp. 11 225–11 234, 2014.
- [43] V. Carey, C. Wemp, E. McClure, and S. Cabrera, “Mechanism Interaction During Droplet Evaporation on Nanostructured Hydrophilic Surfaces,” in *paper IMECE2018-87991, Proc. ASME 2018 International Mechanical Engineering Congress and Exposition, IMECE2018*, Pittsburgh, PA, USA, 2018.
- [44] S. Cabrera and V. Carey, “Comparison of Droplet Evaporation and Nucleate Boiling Mechanisms on Nanoporous Superhydrophilic Surfaces,” in *paper SHTC2019-3539, Proc. ASME 2019 Summer Heat Transfer Conf., SHTC2019*, Bellevue, WA, USA, 2019.
- [45] H. O’Hanley, C. Coyle, J. Buongiorno, *et al.*, “Separate Effects of Surface Roughness, Wettability, and Porosity on the Boiling Critical Heat Flux,” *Appl. Phys. Lett.*, vol. 103, p. 024 102, 2013.
- [46] A. Zou and S. Maroo, “Critical Height of Micro/Nano Structures for Pool Boiling Heat Transfer Enhancement,” *Appl. Phys. Lett.*, vol. 103, p. 024 102, 2013.
- [47] R. Chen, M. Lu, V. Srinivasan, Z. Wang, H. Cho, and A. Majumdar, “Nanowires for Enhanced Boiling Heat Transfert,” *Nano Lett.*, vol. 9, 548–553, 2009.
- [48] C. Li, Z. Wang, P. Wang, Y. Peles, N. Koratkar, and G. Peterson, “Nanostructured copper inter-faces for enhanced boiling,” *Small*, vol. 4, 1084–1088, 2008.
- [49] M. Lu, R. Chen, V. Srinivasan, V. Carey, and A. Majumdar, “Critical Heat Flux of Pool Boiling on Si Nanowire Array-coated Surfaces,” *Int. J. Heat Mass Transf.*, vol. 54, 5359–5367, 2011.
- [50] Z. Yao, Y. Lu, and G. Kandlikar, “Pool Boiling Heat Transfer Enhancement Through Nanostructures on Silicon Microchannels,” *J. Nanotechnol. Eng. Med.*, vol. 3, 031002-1 to 031002-8, 2012.
- [51] A. Betz, J. Jenkins, C. Kim, and D. Attinger, “Boiling Heat Transfer on Superhydrophilic, Superhydrophobic, and Superbiphilic Surfaces,” *Int. J. Heat Mass Transf.*, vol. 57, 733–741, 2013.
- [52] A. Betz, J. Xu, H. Qiu, and D. Attinger, “Do Surfaces with Mixed Hydrophilic and Hydrophobic Areas Enhance Pool Boiling?” *Appl. Phys. Lett.*, vol. 97, p. 141 909, 2010.
- [53] M. Rahman, U. Ölcerogl, and M. McCarthy, “Role of Wickability on the Critical Heat Flux of Structured Superhydrophilic Surfaces,” *Langmuir*, vol. 30, 11225–11234, 2014.

- [54] C. Y. Lee, M. BhuiyaKwang, and J.Kim, “Pool Boiling Heat Transfer with Nano-porous Surface,” *International Journal of Heat and Mass Transfer.*, vol. 53, pp. 4274–4279, 2010.
- [55] E. D. andT. Izci, A. Alagoz, T. Karabacak, and A.Koşar, “Effect of Silicon Nanorod Length on Horizontal Nanostructured Plates in Pool Boiling Heat Transfer with Water,” *International Journal of Thermal Science*, vol. 82, pp. 111–121, 2014.
- [56] B. Bourdon, P. D. Marco, R. Riobóo, M. Marengo, and J. D. Coninck, “Enhancing the Onset of Pool Boiling by Wettability Modification on Nanometrically Smooth Surfaces,” *Int. Commun. Heat Mass Transfer*, vol. 45, pp. 11–15, 2013.
- [57] B. Bourdon, R. Rioboo, M. Marengo, E. Gosselin, and J. D. Coninck, “Influence of the Wettability on the Boiling Onset,” *Langmuir*, vol. 28, pp. 1618–1624, 2012.
- [58] B. Bourdon, E. Bertrand, P. D. Marco, M. Marengo, R. Rioboo, and J. D. Coninck, “Wettability Influence on the Onset Temperature of Pool Boiling: Experimental Evidence onto Ultra-smooth Surfaces,” *Adv. Colloid Interface Sci.*, vol. 221, pp. 34–40, 2015.
- [59] H. Jo, H. Kim, H. Ahn, *et al.*, “Wettability Influence on the Onset Temperature of Pool Boiling: Experimental Evidence onto Ultra-smooth Surfaces,” in *Proceedings of the ASME 2009 7th International Conference on Nanochannels, Microchannels and Minichannels*, ASME, Pohang, South Korea, 2009.
- [60] H. Jo, S. Kim, H. Kim, J. Kim, and M. Kim, “Nucleate Boiling Performance on Nano/Microstructures with Different Wetting Surfaces,” *Nanoscale Res. Lett.*, vol. 7, p. 242, 2012.
- [61] H. Phan, N. Caney, P. Marty, S. Colasson, and J. Gavillet, “Surface Wettability Control by Nanocoating: the Effects on Pool Boiling Heat Transfer and Nucleation Mechanism,” *Int. J. Heat Mass Transfer*, vol. 52, pp. 5459–5471, 2009.
- [62] H. Phan, N. Caney, P. Marty, S. Colasson, and J. Gavillet, “How Does Surface Wettability Influence Nucleate Boiling?” *CR. Mec*, vol. 337, pp. 251–259, 2009.
- [63] H. Jo, D. Yu, H. Noh, H. Park, and M. Kim, “Boiling on Spatially Controlled Heterogeneous Surfaces: Wettability Patterns on Microstructures,” *B, Appl. Phys. Lett.*, vol. 106, p. 181 602, 2015.
- [64] G. Pollack, “Kapitza Resistance,” *Rev. Mod. Phys.*, vol. 41, pp. 48–81, 1969.
- [65] W. Gambill and Lienhard, “ An Upper Bound for the Critical Boiling Heat Flux,” *ASME-JSME Thermal Engineering Joint Conf*, vol. 3, pp. 621–626, 1987.
- [66] W. Rohsenow and P. Griffith, “ Correlation of Maximum Heat Transfer Data for Boiling of Saturated Liquids,” *Chem. Eng. Prog. Symp. Ser.*, vol. 18, pp. 47–49, 1956.

- [67] Y. Chang and N. Snyder, "Heat Transfer in Saturated Boiling," *Chem. Eng. Prog. Symp. Series*, vol. 56, pp. 25–38, 1960.
- [68] S. Kutateladze, "On the transition to film boiling under natural convection," *Kotloturbostroenie*, vol. 3, p. 10, 1948.
- [69] Y. Chang, "A Theoretical Analysis of Heat Transfer in Natural Convection and in Boiling," *Trans. ASME*, vol. 79, pp. 1501–1513, 1957.
- [70] G. I. Taylor, "The Instability of Liquid Surfaces when Accelerated in a Direction Perpendicular to their Plane," *Proceedings of the Royal Society of London. Series A, Mathematical and Physical Sciences*, vol. 201, 1950.
- [71] N. Zuber, "Hydrodynamic Aspects of Boiling Heat Transfer," *AEC Report AECU*, vol. 4439, 1959.
- [72] J. H. Linehard and V. K. Dhir, "Extended Hydrodynamic Theory of The Peak and Minimum Pool Boiling Heat Fluxes," *NASA CR-2270*, 1973.
- [73] J. Lienhard, V. Dhir, and D. Riherd, "Peak Pool Boiling Heat Flux Measurements on Finite Horizontal Flat Plates," *ASME J. Heat Transf.*, vol. 95, pp. 477–482, 1973.
- [74] Y. Kirichenko and P. Chernyakov, "Determination of the First Critical Thermal Flux on Flat Heaters," *Journal of Engineering Physics and Thermophysics*, vol. 20, pp. 699–703, 1971.
- [75] J. Ramilison, P. Sadasivan, and J. Lienhard, "Surface Factors Influencing Burnout on Flat Heaters," *Journal of Heat Transfer*, vol. 114, pp. 287–290, 1992.
- [76] J. Kim, S. Jun, R. Laksnarain, and S. You, "Effect of Surface Roughness on Pool Boiling Heat Transfer at a Heated Surface Having Moderate Wettability," *International Journal of Heat and Mass Transfer*, vol. 101, pp. 992–1002, 2016.
- [77] L. Wang, Y. Li, F. Zhang, F. Xie, and Y. Ma, "Correlations for Calculating Heat Transfer of Hydrogen Pool Boiling," *International Journal of Hydrogen Energy*, vol. 41, pp. 17118–17131, 2016.
- [78] V. Borishanskii, "On the Problem of Generalizing Experimental Data on the Cessation of Bubble Boiling in Large Volume of Liquids," *Report No. Ts. K.I.T 28*,
- [79] L. Liao, R. Bao, and Z. Liu, "Compositive Effects of Orientation and Contact Angle on Critical Heat Flux in Pool Boiling of Water," *Heat and Mass Transfer*, vol. 44, pp. 1447–1453, 2008.

- [80] M. El-Genk and H. Bostanci, "Saturation Boiling of HFE-7100 from a Copper Surface, Simulating a Microelectronic Chip," *International Journal of Heat and Mass Transfer*, vol. 46, pp. 1841–1854, 2003.
- [81] M. Arik and A. Bar-Cohen, "Ebullient Cooling of Integrated Circuits by Novec Fluids," in *in: Proceedings of the Pacific Rim International Intersociety Electronic Packaging Conference*, 2001, pp. 18–32.
- [82] P. Berenson, "Transition Boiling Heat Transfer from a Horizontal Surface," in *AICHE Paper 18, ASME-AICHE Heat Transfer Conference*, Buffalo, NY, 1960.
- [83] E. Hahne and T. Diesselhorst, "Hydrodynamic and Surface Effects on the Peak Heat Flux in Pool Boiling," in *Proc 6th Int. Heat Transf. Conf.*, vol. 1, 1978, pp. 209–214.
- [84] N. Nagai and V. Carey, "Assessment of Surface Wettability and its Relation to Boiling Phenomena," *Therm. Sci. Eng.*, vol. 10, pp. 1–9, 2002.
- [85] S. Kandlikar, "A theoretical model to predict pool boiling CHF incorporating effects of contact angle and orientation," *J. Heat Transf.*, vol. 123, pp. 1071–1079, 2001.
- [86] S. P. Liaw and V. K. Dhir, "Effect of Surface Wettability on Transition Boiling Heat Transfer from a Vertical Surface," *Proceedings of the Eighth International Heat Transfer Conference, San Francisco, CA.*, vol. 4, pp. 2031–2036, 1986.
- [87] J. M. Ramilison and J. H. Lienhard, "Transition Boiling Heat Transfer and the Film Transition Regime," *ASME J. Heat Transf.*, vol. 109, pp. 746–752, 1987.
- [88] V. I. Deev, V. E. Keilin, I. A. Kondratenko, and V. I. Petrovichev, "Nucleate and Film Pool Boiling Heat Transfer to Saturated Liquid Helium," *Cryogenics*, vol. 17, pp. 557–562, 1977.
- [89] L. Bewilogua and H. Vinzelberg, "Heat Transfer in Cryogenic Liquids under Pressure," *Cryogenics*, vol. 3, pp. 121–125, 1975.
- [90] N. A. and F. W. Staub, "Low Pressure Pool Boiling and Critical Heat Flux Limits for R-113," *AICHE Symp. Ser.*, vol. 225, pp. 35–40, 1983.
- [91] C. Bonilla and C. Perry, "Heat Transmission to Boiling Binary Liquid Mixtures," *Transactions of American Society of Chemical Engineers*, vol. 37, pp. 685–705, 1941.
- [92] A. Sakurai and M. Shiotsu, "Temperature-Controlled Pool-Boiling Heat Transfer," *Proceedings of the Fifth International Heat Transfer Conference*, vol. 4, pp. 81–85, 1974.

- [93] N. Bakhru and J. H. Lienhard, “Boiling from Small Cylinders,” *International Journal of Heat and Mass Transfer*, vol. 15, pp. 2011–2025, 1972.
- [94] J. H. Lienhard, V. K. Dhir, and D. M. Riherd, “Peak Pool Boiling Heat Flux Measurements on Finite Horizontal Flat Plates,” *ASME Journal of Heat Transfer*, vol. 95, pp. 477–482, 1973.
- [95] J. H. Lienhard and V. K. Dhir, “Hydrodynamic Prediction of Peak Pool-boiling Heat Fluxes from Finite Bodies,” *ASME Journal of Heat Transfer*, vol. 95, pp. 152–158, 1973.
- [96] K. H. Sun and J. H. Lienhard, “The Peak Pool Boiling Heat Flux on Horizontal Cylinders,” *International Journal of Heat and Mass Transfer*, vol. 13, pp. 1425–1439, 1970.
- [97] J. S. Ded and J. H. Lienhard, “The Peak Pool Boiling Heat Flux from a Sphere,” *AIChE Journal*, vol. 18, pp. 337–342, 1972.
- [98] Y. Katto and S. Yokoya, “Experimental Study of Nucleate Pool Boiling in Case of Making Interference-plate Approach to the Heating Surface,” in *Proceedings of 3rd International Journal of Heat Transfer Conference*, Chicago, USA, 1966, pp. 219–227.
- [99] Y. Katto, S. Yokoya, and K. Terakoa, “Nucleate and Transition Boiling in a Narrow Space Between Two Horizontal Parallel Disk Surfaces,” *Bulletin of JSME*, vol. 20, pp. 638–643, 1977.
- [100] M. Kapitz, F. Reinker, and S. aus der Wiesche, “Viscous Fingering and Heat Transfer During Boiling in a Hele–Shaw Cell,” *Experimental Thermal and Fluid Science*, vol. 67, pp. 18–23, 2015.
- [101] M. Misale, G. Guglielmini, A. Priarone, and C. Ambientale, “HFE-7100 Pool Boiling Heat Transfer and Critical Heat Flux in Inclined Narrow Spaces,” *International Journal of Refrigeration*, vol. 32, pp. 235–245, 2009.
- [102] M. Misale, G. Guglielmini, and A. Priarone, “Nucleate Boiling and Critical Heat Flux of HFE-7100 in Horizontal Narrow Spaces,” *Experimental Thermal and Fluid Science*, vol. 35, pp. 772–779, 2011.
- [103] R. R. Souza, J. C. Passos, and E. M. Cardoso, “Confined and Unconfined Nucleate Boiling under Terrestrial and Microgravity Conditions,” *Applied Thermal Engineering*, vol. 51, pp. 1290–1296, 2013.
- [104] M. Kapitz, L. Schmiedinghoff, S. J. Lüling, and S. aus der Wiesche, “Impact of Surface Parameters on Confined Boiling Heat Transfer in a Hele-Shaw Cell,” *Heat and Mass Transfer*, vol. 55, pp. 2533–2604, 2019.

- [105] A. Sarode, R. Raj, and A. Bhargav, “On the Role of Confinement Plate Wettability on Pool Boiling Heat Transfer,” *international Journal of Heat and mass Transfer*, vol. 156, p. 119 723, 2020.
- [106] I. Kiyomura, T. Mogaji, L. Manetti, and E. Cardoso, “A Predictive Model for Confined and Unconfined Nucleate Boiling Heat Transfer Coefficient.,” *Applied Thermal Engineering*, vol. 127, pp. 1274–1284, 2017.
- [107] E. Cardoso and J. Passos, “Nucleate Boiling of n-Pentane In a horizontal Confined Space.,” *Heat Transfer Engineering*, vol. 34, pp. 470–478, 2013.
- [108] Chan, M. Aaron, C. Yap, and K. Ng, “A Correlation for Confined Nucleate Boiling Heat Transfer.,” *Journal of Heat Transfer*, vol. 133, p. 074 502, 2011.
- [109] G. Su, Y. Wu, and K. Sugiyama, “Subcooled Pool Boiling of Water on a Downward-facing Stainless Steel Disk in a Gap,” *International Journal of Multiphase Flow*, vol. 34, pp. 1058–1066, 2008.
- [110] E. Ishibashi and K. Nishikawa, “Saturated Boiling Heat Transfer in Narrow Spaces.,” *International Journal of Heat and Mass Transfer*, vol. 12, pp. 863–893, 1969.
- [111] J. Bonjour and M. Lallemand, “Effects of Confinement and Pressure on Critical Heat Flux During Natural Convective Boiling in Vertical Channels,” *International Communications in Heat and Mass Transfer*, vol. 24, pp. 191–200, 2 1997.
- [112] Y. Katto and Y. Kosho, “Critical Heat Flux of Saturated Natural Convection Boiling in a Space Bounded by Two Horizontal Co-Axial Disks and Heated From Below,” *International Journal of Multiphase Flow*, vol. 5, pp. 219–224, 1979.
- [113] Y. H. Kim and K. Y. Suh, “One Dimensional Critical Heat Flux Concerning Surface Orientation and Gas Size Effects,” *Nuclear Engineering and Design*, vol. 226, pp. 277–292, 2003.
- [114] J. Kim, D. Shin, S. You, and J. Lee, “Pool boiling heat transfer on bare and microporous surfaces confined in a narrow gap,” *International Journal of Heat and Mass Transfer*, vol. 162, p. 120 329, 2020.
- [115] M. Monde, H. Kusuda, and H. Uehara, “Critical Heat Flux During Natural Convective Boiling in Vertical Rectangular Channels Submerged in Saturated Liquid,” *ASME Journal of Heat Transfer*, vol. 104, pp. 300–303, 1982.
- [116] M. Sullivan, “Cloud and Data Center Network Technologies: Global Market Through 2022,” *BCC Research LLC, IFT103A*, 2018.

- [117] R. Rake, “North America Data Center Cooling Market by Component, Type of Cooling, Type of Data Center, Industry Vertical: Opportunity Analysis and Industry Forecast, 2018 - 2025,” *Allied Market Reserach*, 2019.
- [118] A. Shehabi, S. J. Smith, D. A. Sarto, *et al.*, “United States Data Center Energy Usage Report,” *Lawrence Berkeley National Laboratory, Berkeley, California*, 2019.
- [119] L. A. Barroso, U. Hölzle, J. Clidaras, and Parthasarathy, *The Datacenter as a Computer: An Introduction to the Design of Warehouse-Scale Machines*, third edition. Morgan and Claypool, 2018.
- [120] S. V. Garimella, T. Persoons, J. A. Weibel, and V. Gektin, “Electronics Thermal Management in Information and Communications Technologies: Challenges and Future Directions,” *IEEE Transactions on Components, Packaging and Manufacturing Technology*, vol. 7, pp. 1191–1205, 8 2017.
- [121] H. C. Coles and S. E. Greenberg, “Direct Liquid Cooling for Electronic Equipment,” *Lawrence Berkeley National Laboratory, Berkeley, CA.,* 2014.
- [122] H. Altman, A. Gupta, and M. Tyhach, “Thermal Management Research – from Power Electronics to Portables,” in *ASME International Technical Conference and Exhibition on Packaging and Integration of Electronic and Photonic Microsystems*, San Francisco, California, USA, 2015.
- [123] K. P. Drummond, D. Back, M. D. Sinanis, *et al.*, “Characterization of Hierarchical Manifold Microchannel Heat Sink Arrays Under Simultaneous Background and Hotspot Heating Conditions,” *International Journal of Heat and Mass Transfer*, vol. 126, pp. 1289–1301, 2018.
- [124] T. J. Chainer, M. D. Schultz, P. R. Parida, and M. A. Gaynes, “Improving Data Center Energy Efficiency With Advanced Thermal Management,” *IEEE Transactions on Components, Packaging and Manufacturing Technology*, vol. 7, 8 2017.
- [125] D. F. Hanks, Z. Lu, J. Sircar, *et al.*, “Nanoporous Membrane Device For Ultra High Heat Flux Thermal Management,” *Microsyst Nanoeng*, vol. 4, 1 2018.
- [126] P. Asrar, X. Zhang, C. E. Green, M. Bakir, and Y. K. Joshi, “Flow Boiling of R245fa in a Microgap with Staggered Circular Cylindrical Pin Fins,” *International Journal of Heat and Mass Transfer*, vol. 121, pp. 239–342, 2018.

- [127] D. G. Bae, R. K. Mandel, S. V. Dessiatoun, *et al.*, “Embedded Two-phase Cooling of High Heat Flux Electronics on Silicon Carbide (SiC) Using Thin-film Evaporation and an Enhanced Delivery System (FEEDS) Manifold-microchannel Cooler,” in *16th IEEE International Conference on Thermal and Thermomechanical Phenomena in Electronic Systems (ITherm)*, Orlando, FL, USA, 2017.
- [128] G. R. Wagner, J. R. Schaadt, J. Dixon, *et al.*, “Test Results From the Comparison of Three Liquid Cooling Methods for High-power Processors,” in *in Proc. 15th IEEE Thermal and Thermomechanical Phenomena in Electronic Systems (ITherm)*, Las Vegas, NV, USA, 2016.
- [129] H. Coles and M. Herrlin, “Immersion Cooling of Electronics in DoD Installation,” *Lawrence Berkeley National Laboratory, Berkeley, CA*, 2017.
- [130] P. E. Tuma, “The Merits of Open Bath Immersion Cooling of Datacom Equipment,” in *in 26th Annual IEEE Semiconductor Thermal Measurement and Management Symposium (SEMI-THERM)*, Santa Clara, CA, USA, 2010.
- [131] E. Cardoso, O. Kannengieser, B. Stutz, and J. C. Passos, “FC72 and FC87 Nucleate Boiling Inside a Narrow Horizontal Space,” *Experimental Thermal and Fluid Science*, vol. 35, pp. 1038–1045, 2011.
- [132] R. R. Souza, E. M. Cardoso, and J. Passos, “Confined and Unconfined Nucleate Boiling of HFE7100 in the Presence of Nanostructured Surfaces,” *Experimental Thermal and Fluid Science*, vol. 91, pp. 312–319, 2017.
- [133] J. Passos, F. Hirata, L. Possamai, M. Balsamo, and M. Misale, “Confined boiling of FC72 and FC87 on a downward facing heating copper disk,” *International Journal of Heat and Fluid Flow*, vol. 25, pp. 313–319, 2004.
- [134] M.G.Cooper and A.J.P.Lloyd, “The Microlayer in Nucleate Pool Boiling,” *International Journal of Heat and Mass Transfer*, vol. 12, pp. 895–913, 13 1969.
- [135] I. Mudawar, “Assessment of High Heat Flux Thermal Management Schemes,” *IEEE Transactions on Components, Packaging and Manufacturing Technology*, vol. 24, pp. 122–141, 2001.
- [136] I. Mudawar, “Two-phase Microchannel Heat Sinks: Theory, Applications, and Limitations,” *Journal of Electronic Packaging*, vol. 133, p. 041 002, 2011.
- [137] I. Mudawar, “Recent Advances in High-flux, Two-phase Thermal Management,” *Journal of Thermal Science and Engineering Applications*, vol. 5, p. 021 012, 2013.

- [138] G. Liang and I. Mudawar, “Review of Spray Cooling Part 1: Single-phase and Nucleate Boiling Regimes, and Critical Heat Flux,” *International Journal of Heat and Mass Transfer*, vol. 115, pp. 1174–1205, 2017.
- [139] J. Broughton, V. Smet, R. R. Tummala, and Y. Joshi, “Review of Thermal Packaging Technologies for Automotive Power Electronics for Traction Purposes,” *Journal of Electronics Packaging*, vol. 140(4), p. 040 801, 2018.
- [140] K. W. Jung, C. Zhang, T. Liu, M. Asheghi, and K. E. Goodson, “Thermal Management Research – from Power Electronics to Portables,” in *IEEE Symposium on VLSI Technology*, Honolulu, HI, 2018.
- [141] D. Mallik, R. Mahajan, N. Raravikar, K. Radhakrishnan, K. Aygun, and B. Sankman, *Flip-Chip Packaging for Nanoscale Silicon Logic Devices: Challenges and Opportunities*, In: Morris J. (eds) Nanopackaging. Springer, Cham, 2018.
- [142] J. A. Weibel and S. V. Garimella, “Recent Advances in Vapor Chamber Transport Characterization for High-Heat-Flux Application,” *Advances in Heat Transfer*, vol. 45, pp. 209–301, 2013.
- [143] A. Faghri, “Review and Advances in Heat Pipe Science and Technology,” *Journal of Heat Transfer*, vol. 134(12), p. 123 001, 2012.
- [144] R. Chu, R. Simons, M. Ellsworth, R. Schmidt, and V. Cozzolino, “Review of Cooling Technologies for Computer Products,” *IEEE Transactions on Device and Materials Reliability*, vol. 4, pp. 568–585, 4 2004.
- [145] S. G. Kandlikar, “History, Advances, and Challenges in Liquid Flow and Flow Boiling Heat Transfer in Microchannels: A Critical Review,” *Journal of Heat Transfer*, vol. 134, p. 034 001, 3 2012.
- [146] G. Klein and J. Westwater, “Heat Transfer from Multiple Spines to Boiling Liquids,” *AIChE Journal*, vol. 17, pp. 1050–1056, 1971.
- [147] R. Shimada, J. Komai, Y. Hirono, S. Kumagai, and T. Takeyama, “Enhancement of Boiling Heat Transfer in a Narrow Space Restricted by an Interference Plate with Holes,” *Experimental Thermal and Fluid Science*, vol. 4, pp. 587–593, 1991.
- [148] S. Liter and M. Kaviany, “Pool Boiling CHF Enhancement by Modulated Porous Layer Coating: Theory and Experiment,” *Internatioanl Journal of Heat and Mass Transfer*, vol. 44, pp. 4287–4311, 2001.

- [149] T. Harirchian and S. V. Garimella, “A Comprehensive Flow Regime Map for Microchannel Flow Boiling with Quantitative Transition Criteria,” *International Journal of Heat and Mass Transfer*, vol. 53, pp. 2694–2702, 13-14 2010.
- [150] S. G. Kandlikar, “Fundamental Issues Related to Flow Boiling in Minichannels and Microchannels,” *Experimental Thermal and Fluid Science*, vol. 26, pp. 389–407, 2-4 2002.
- [151] Z. LIU and R. H. S. WINTERTON, “A General Correlation for Saturated and Subcooled Flow Boiling in Tubes and Annuli, Based on a Nucleate Pool Boiling Equation,” *International Journal of Heat and Mass Transfer*, vol. 34, pp. 2759–2766, 11 1991.
- [152] P. A. Kew and K. Cornwell, “Correlations for the Prediction of Boiling Heat Transfer in Small Diameter Channels,” *Applied Thermal Engineering*, vol. 17, pp. 705–715, 8-10 1997.
- [153] M.G.Cooper and A.J.P.Lloyd, “The Microlayer in Nucleate Pool Boiling,” *International Journal of Heat and Mass Transfer*, vol. 12, pp. 895–913, 1969.
- [154] B. Stutz, M. Lallemand, F. Raimbault, and J. Passos, “Nucleate and Transition Boiling in Narrow Horizontal Spaces,” *Heat and Mass Transfer*, vol. 45, pp. 929–935, 2009.
- [155] M. Lallemand, J. Bonjour, D. Gentile, and F. Boulanger, “The Physical Mechanisms Involved in the Boiling of Mixtures in Narrow Spaces,” in *International Heat Transfer Conference*, Kyongjiu, Korea, 1998, pp. 515–519.
- [156] A. Alsaati, J. A. Weibel, and A. Marconnet, “Confined Immersion Cooling in Microscale Gaps,” in *IEEE Intersociety Conference on Thermal and Thermomechanical Phenomena in Electronic Systems (ITherm)*, Orlando, FL, USA, 2020.
- [157] C. N. Hunter, N. R. Glavin, C. Muratore, *et al.*, “Micro-patterned substrates with nano-scale elements for pool boiling,” in *ASME/JSME 8th Thermal Engineering Joint Conference*, Honolulu, Hawaii, USA, 2011.
- [158] S. J. D. V. Stralen, M. S. Sohal, R. Cole, and W. M. Sluyter, “Bubble Growth Rate in Pure and Binary Systems: Combined Effect of Relaxation and Evaporation Microlayer,” *International Journal of Heat and mass Transfer*, vol. 18, pp. 453–467, 1975.
- [159] R. Cole, “Bubble Frequencies and Departure Volumes at subatmospheric Pressures,” *AIChE Journal*, vol. 13, pp. 779–783, 1967.
- [160] G. Liang and I. Mudawar, “Pool Boiling Critical Heat Flux (CHF) – Part 1: Review of Mechanisms, Models, and Correlations,” *International Journal of Heat and Mass Transfer*, vol. 117, pp. 1352–1367, 2018.

- [161] J. Brandner, E. Anurjew, L. Bohn, *et al.*, “Concepts and Realization of Microstructure Heat Exchangers for Enhanced Heat Transfer,” *Experimental Thermal and Fluid Science*, vol. 30, pp. 801–809, 2006.
- [162] A. S. Sundaram and A. Bhaskaran, “Thermal Modeling of Thermosyphon Integrated Heat Sink for CPU Cooling,” *Journal of Electronics Cooling and Thermal Control*, vol. 1, pp. 15–21, 2011.
- [163] D. Bastakoti, H. Zhang, D. Li, W. Cai, and F. Li, “An Overview on the Developing Trend of Pulsating Heat Pipe and its Performance,” *Applied Thermal Engineering*, vol. 141, pp. 305–332, 2018.
- [164] J. H. Moon, D. Fadda, D. H. Shin, J. S. Kim, J. Lee, and S. M. You, “Boiling-driven, Wickless, and Orientation-independent Thermal Ground Plane,” *International Journal of Heat and Mass Transfer*, vol. 167, p. 120 817, 2021.
- [165] C. Lang, “Transactions of Institute of Engineers and Ship builders,” *Scotland*, vol. 32, pp. 279–295, 1888.
- [166] T. G. Theofanous and T. N. Dinh, “High Heat Flux Boiling and Burnout as Microphysical Phenomena: Mounting Evidence and Opportunities,” *Multiphase Science and Technology*, vol. 18, pp. 251–276, 3 2006.
- [167] S. G. Kandlikar, “History, Advances, and Challenges in Liquid Flow and Flow Boiling Heat Transfer in Microchannels: A Critical Review.,” *ASME. J. Heat Transfer*, vol. 134, p. 034 001, 2012.
- [168] T. Harirchian and S. Garimella, “The critical role of channel cross-sectional area in microchannel flow boiling heat transfer,” *International Journal of Multiphase Flow*, vol. 35, 904-913 2009.
- [169] Y. Change and S. Yao, “Critical Heat Flux of Narrow Vertical Annuli With Closed Bottoms,” *ASME Journal of Heat Transfer*, vol. 105, pp. 192–195, 1993.
- [170] G. B. Wallis, *One-Dimensional Two-Phase Flow*. New York, NY, USA: McGraw Hill, 1969, ch. 11.
- [171] W. A. Ragland and E. N. Ganic, “Flooding in counter-current two-phase flow,” in *Advances in Two-Phase Flow and Heat Transfer*, S. Kakaç and M. Ishii, Eds., Dordrecht: Springer, 1983, ch. 64, pp. 505–538.
- [172] A. Alsaati, D. Warsinger, J. Weibel, and A. Marconnet, “Vapor Stem Bubbles Dominate Heat Transfer Enhancement in Extremely Confined Boiling,” *International Journal of Heat and Mass Transfer*, vol. 177, p. 121 520, 2021.

- [173] J. Bonjour and M. Lallemand, “Flow patterns during boiling in a narrow space between two vertical surfaces,” *International Journal of Multiphase Flow*, vol. 24, pp. 947–960, 6 1998.
- [174] Y. Fujita, H. Ohta, and S. Uchida, “Nucleate boiling heat transfer and critical heat flux in narrow space between rectangular surfaces,” *International Journal of Heat and Mass Transfer*, vol. 31, pp. 229–239, 2 1988.
- [175] M. C. Chyu, “Prediction of Boiling Dryout Flux for Restricted Annular Crevice,” *International Journal of Heat and Mass Transfer*, vol. 31, pp. 1993–1998, 1988.
- [176] Y. ZHAO, T. TSURUTA, and T. MASUOKA, “Critical Heat Flux of Boiling Heat Transfer in a Confined Space,” *JSME International Journal Series B*, vol. 44, pp. 344–351, 2001.
- [177] A. Pham, M. Barisik, and B. Kim, “Pressure Dependence of Kapitza Resistance at Gold/Water and Silicon/Water Interfaces,” *Journal of Chemical Physics*, vol. 139, 24 2013.
- [178] T. Theofanous, T.-N. Dinh, J. Tu, and A. Dinh, “The Boiling Crisis Phenomenon: Part I: Nucleation and Nucleate Boiling Heat Transfer,” *Experimental Thermal and Fluid Science*, vol. 26, pp. 775–792, 2002.
- [179] T. Theofanous, T.-N. Dinh, J. Tu, and A. Dinh, “The Boiling Crisis Phenomenon: Part II: Dryout Dynamics and Burnout,” *Experimental Thermal and Fluid Science*, vol. 26, pp. 793–810, 2002.
- [180] E. M. Cardoso and J. Passos, “Nucleate Boiling of n-Pentane in a Horizontal Confined Space,” *Heat Transfer Engineering*, vol. 34, pp. 470–478, 2012.
- [181] J. Nunes, R. deSouza, A. Rodrigues, M. Safaei, and E. M. Cardoso, “Influence of Coated Surfaces and Gap Size on Boiling Heat Transfer of Deionized Water,” *Journal of the Brazilian Society of Mechanical Sciences and Engineering*, vol. 42, p. 127, 2020.
- [182] K. Geisler and A. Bar-Cohen, “Confinement Effects on Nucleate Boiling and Critical Heat Flux in Buoyancy-driven Microchannels,” *International Journal of Heat and Mass Transfer*, vol. 52, pp. 2427–2436, 2009.
- [183] M. Reeber and R. Frieser, “Heat Transfer of Modified Silicon Surfaces,” *IEEE Trans. Compon. Hybrid Manuf. Technol.*, vol. 3, pp. 387–391, 1980.
- [184] J. Bardeen and W. H. Brattain, “The Transistor, A Semi-Conductor Triode,” *Phys Rev*, vol. 74, pp. 230–231, 2 1948.

- [185] R. Beica, “Enabling Information Age through Advanced Packaging Technologies and Electronic Materials,” in *24th Pan Pacific Microelectronics Symposium*, Hapuna Beach, Hawaii, USA, 2018.
- [186] R. Beica, “The Growth of Heterogeneous Integration and The Importance of Electronic Materials,” in *IMAPS Device Packaging Conference*, Fountain Hills, AZ, USA, 2018.
- [187] R. Beica and J. Hunter, “Heterogeneous Integration Roadmap; WLP TWG,” in *IEEE 68th Electronic Components and Technology Conference (ECTC)*, San Diego, CA, USA, 2018.
- [188] S. Kumar, S. Chitoraga, and F. Shoo, “Status of the advanced packaging industry 2021,” Yole Developpement, 2021.
- [189] G. E. Moore, “Cramming More Components Onto Integrated Circuits,” *IEEE Solid-State Circuits Society Newsletter*, vol. 38, 8 1965.
- [190] P. Ruch, T. Brunschwiler, and W. Escher, “Toward Five-dimensional Scaling: How Density Improves Efficiency in Future Computers,” *IEEE Solid-State Circuits Society Newsletter*, vol. 55, 5 2011.
- [191] M. J. Khurshid and M. Lipasti, “Data Compression for Thermal Mitigation in the Hybrid Memory Cube,” in *IEEE 31st International Conf. on Computer Design (ICCD)*, Asheville, NC, USA, 2013.
- [192] P. Leduc, F. de Crecy, and M. Fayolle, “Challenges for 3D IC Integration: Bonding Quality and Thermal Management,” in *2007 IEEE International Interconnect Technology Conference*, 2007, pp. 210–212.
- [193] J. Cong, J. Wei, and Y. Zhang, “A Thermal-driven Floor Planning Algorithm for 3D ICs,” in *IEEE/ACM International Conference on Computer Aided Design*, 2004, pp. 306–313.
- [194] W. Xiaojin, K. Marston, and K. Sikka, “Thermal Modeling for Warpage Effects in Organic Packages,” in *11th Intersociety Conference on Thermal and Thermomechanical Phenomena in Electronic Systems (ITHERM 2008)*, 2008.
- [195] M. Schultz, M. Gaynes, P. Parida, and T. Chainer, “Experimental Investigation of Direct Attach Microprocessors in a Liquid-cooled Chiller-less Data Center.,” in *IEEE Intersociety Conference on Thermal and Thermomechanical Phenomena in Electronic Systems (ITherm)*, 2014.
- [196] G. S. et al., “Lid-integral Cold Plate Topology Integration, Performance, and Reliability,” in *Proceedings InterPACK (6–9 July 2015)*, 2015.

- [197] Y. Madhour and M. Z. G. Schlottig, "Integration of Intra Chip Stack Fluidic Cooling Using Thin-layer Solder Bonding," in *IEEE International 3D Systems Integration Conference (3DIC) October 2013*, 2013.
- [198] T. Brunswiler, A. Sridhar, C. Ong, and G. Schlottig, "Benchmarking study on the thermal management landscape for 3D ICs: from back-side to volumetric heat removal," in *Proceedings of InterPack (6-9 July 2015)*, 2015.
- [199] T. Brunswiler, "Interlayer Thermal Management of High Performance Microprocessor Chip Stacks," in *Berlin: Cuvillier Verlag Göttingen*, 2012.
- [200] E. Colgan and et al., "A Practical Implementation of Silicon Microchannel Coolers for High Power Chips," *IEEE Transactions on Components and Packaging Technologies*, vol. 30, 2 2007.
- [201] P. D. Franzon, E. J. Marinissen, and M. S. Bakir, *Handbook of 3D Integration: Design, Test, and Thermal Management*, 4th ed. Weinheim, Germany: the Deutsche Nationalbibliothek, 2019, ISBN: 978-3-527-69704-5.
- [202] A. Bar-Cohen, F. L. Robinson, and D. C. Deisenroth, "Challenges and Opportunities in Gen3 Embedded Cooling with High-Quality Microgap Flow," in *2018 International Conference on Electronics Packaging and iMAPS All Asia Conference, ICEP-IAAC 2018*, 2018, pp. 1-12.
- [203] C. L. Ong, S. Paredes, A. Sridhar, B. Michel, and T. Brunswiler, "Radial Hierarchical Microfluidic Evaporative Cooling for 3-D Integrated Microprocessors," in *Proceedings of the 4th European Conference on Microfluidics - Microfluidics 2014 - Limerick*, 2014.

A. HETEROGENEOUS INTEGRATION OF ELECTRONICS AND ASSOCIATED THERMAL CHALLENGES

Digital transformation is expanding into almost all markets motivating technology innovation in electronics packaging. There is an increasing number of applications demanding smarter and smaller devices with increased performance driven by global trends such as artificial intelligence, environmental consciousness, well-being, mobility, connectivity, and enhanced user experience. Computing and packaging trends have come a long way from the first working point-contact transistor at a separation of $250\ \mu\text{m}$ [184] to the 5 nm-technology-node now used in manufacturing with a wide range of single and multiple die packaging. Initially, increasing performance was the primary focus of technological innovation. However, nowadays, miniaturization, cost, and increasing functionality have become critical drivers for technological innovation. Further, expected growth in connectivity, the internet of things (IoT), artificial intelligence, and many more digital applications across diverse markets will continue to increase the demand and complexity of electronics packaging. As a result, more industries are expanding into heterogeneous integration to satisfy the growing requirements.

The ability to integrate two or more active or passive components within one package, *i.e.* heterogeneous integration, has several major benefits. Components within electronic devices can be co-designed and optimized for higher performance, faster time to market, smaller form factor, and lower cost [185]. In fact, heterogeneous integration has already been implemented for logic and memory integration, RF and FEM modules, MEMS and sensing modules, IoT, wireless connectivity packages, and power management [186]. The increase in integration complexity to address the increasing functionality results in an increasing number of inputs and outputs (I/Os). One of the key enablers of complex integration is the success of through-silicon via (TSV) interposer technology, also called “2.5D” packaging platforms, which enables high interconnect density between side-by-side active devices through a redistribution layer and TSVs. Consequently, expanding TSVs into Three-dimensional integration has been identified as the key technology for the future of heterogeneous integration by industrial consortia [187]. In effect, multiple international roadmap initiatives have been established to facilitate technology development of electronics 3D integration such as the In-

ternational Roadmap for Devices and Systems (IRDS) and The Heterogeneous Integration Roadmap (HIR). In fact, in 2019, the market for 3D packaging was already a US\$ 4.76 billion market and is expected to have the highest Compound Annual Growth Rate (CAGR) among Integrated Circuit (IC) packaging technologies [188].

In 1965, Gordon Moore projected a trend where the number of transistors in a dense Integrated Circuits (ICs) doubles every two years [189]. Ever since, his projection, also known as Moore's law, has been the industry guide for setting research and developments goals. These aggressive goals resulted in tremendous improvement in performance and miniaturization over the last decades. Remarkably, the scaling of transistor dimensions only accounts for half of the miniaturization of digital devices [189]. Densification of electronics relies on the densifying the packaging of the electronics, which requires efficient thermal management. Hence, technological advances in packaging and thermal management are crucial for further reduction of the volume of the electronic systems. While substantial work has been done, still there is still room for development: the volume of active transistors in a device accounts for less than 1 ppm of the entire system volume [190].

Vertical integration of active component, also called 3D integration, has the potential to unleash the next era of computing. With advances in Through Silicon Via (TSV) technology, 3D integration has been realized in commercial products. However, 3D integration is limited moderate heat dissipation: 50W for single side heat removal [191]. Cooling has been identified as one on the main limiting factor for 3D stacked dies owing to the increase of the volumetric power density and added thermal interfaces in a dense system integration packaging [192], [193]. The increasing demand for 3D integration motivates the development of novel cooling solutions specifically designed for 3D packages.

The emerging 3D heterogeneous integration technology uncover associated thermal challenges due to the higher thermal resistances within the stack and the higher total power density. In general, an effective thermal solution must address two main challenges. First, multiple thermal interfaces within stacked dies increases the spreading resistance of internal hotspots, while simultaneously stacking dies increases the total power density flux at the topmost layer attached to the heat sink. Second, the 3D heterogeneous integration of diverse components within package lead to differing power generation and temperature

limits which results in undesirable thermal cross talk between high power components and temperature-sensitive low power components.

For low power devices backside heat removal, originally developed for single chip devices, can be exploited. For flip-chip packages, a cold plate absorbs the generated heat from the back side of the active die. Typically, a high thermally conductive lid protects the chip mechanically [194]. Thermal interface materials (TIMs) improve thermal coupling across solid-solid interfaces. The total thermal resistance from the chip to the cold plate is reduced through a direct attachment of the cold plate to the chip in a lidless configuration at the cost of reducing mechanical robustness [195], [196]. Furthermore, to eliminate TIMs in the thermal path, the cold plate can be integrated in the topmost chip of the stack through embedded microfluidic channels within the silicon layer.

Dual-side cooling can reduce the thermal constraints on the 3D chip stacks. Dual-side cooling can be realized by integrating sealed fluid channels into the interposer in between the TSVs [197]. Ultimately, in order to truly realize volumetric heat removal, cooling channels need to be integrated in between active dies within the chip stack [197], [198]. Hence, a co-design approach is required for the integration of TSVs and interlayer cooling channels, which poses a major challenge. High density TSVs at pitch below 100 μm along with chip foot print more than 2 cm^2 result in cooling channels with relatively large length and small hydraulic diameter, which limits the cooling performance significantly. Many hydraulic design options have been proposed to enhance interlayer cooling performance such as fluid networks, 4-port fluid delivery, temporal workload allocation strategies [199].

Advancement of single-phase cooling designs have improved performance compared to conventional microchannels, achieving thermal resistances as low as $10 \text{ mm}^2\text{KW}^{-1}$ [200]. However, single-phase cooling schemes relies on the sensible heating of the fluid to absorb the heat along the heated cavity which induces high inlet-outlet thermal chip gradient. As a result, thermomechanical stresses can be significant. On the other hand, two-phase cooling utilizes the latent heat of vaporization to dissipate heat. The two-phase cooling approach is highly attractive for embedded volumetric cooling scheme. Since it relies on phase change to absorb the heat from the surface, the fluid maintains near saturation temperature across the chip [201]. Furthermore, boiling of a heat transfer fluid within an electronics package

can potentially overcome the thermal challenges that heterogeneous integration introduces. Multiple thermal interfaces within current packages hinder the spreading of internal hot spots. The relatively low phase-change thermal resistance associated with boiling is beneficial to reduce internal hot spot temperatures and avoid other thermomechanical complications [202]. Further, the heterogeneous integration of diverse components within package lead to differing power generation and temperature limits. Confined boiling of a working fluid contained within a package may maintain isothermalization across these components and limit thermal cross talk due to the inherent self-adjusting thermal resistance [203]. However, the high degree of geometrical confinement significantly alters the two-phase heat dissipation characteristics. Hence, it is crucial to have a deeper understanding of the mechanistic effects of confinement on two-phase heat dissipation in order to predict and optimize design of two-phase cooling solution for thermal management.